Gaining Nanophotonic Control through Crystalline Anisotropy

By

Joseph Robert Matson

Dissertation

Submitted to the Faculty of the
Graduate School of Vanderbilt University
in partial fulfillment of the requirements
for the degree of

DOCTOR OF PHILOSOPHY
In
Interdisciplinary Materials Science
May 12th, 2023
Nashville, Tennessee

Approved:

Joshua D. Caldwell, Ph.D.

Greg Walker, Ph.D.

Lauren Buchanan, Ph.D.

Jason Valentine, Ph.D.

Stephanie Law, Ph.D.

To my parents, who inspired me to follow my curiosity,

and to my partner, who supported me.

ACKNOWLEDGMENTS

My time at Vanderbilt has been a rewarding and transformative experience. I am deeply grateful for the opportunities I have had here, and to the numerous people who contributed to it. During my PhD I have gained a new worldview, and lifelong friends; and I will remember these days fondly.

First, I would like to thank my advisor, Prof. Josh Caldwell, for the endless support, encouragement, and direction over the past five years. Thank you for all of the opportunities you have given me. You have always been available to discuss research and life in general, and your patience, understanding, and mentorship have been fundamental in my development as a scientist.

I would like to thank my other committee members, Prof. Greg Walker, Prof. Jason Valentine, Prof. Lauren Buchanan, and Prof. Stephanie Law for their feedback and guidance through my graduate career. I would also like to thank Prof. Sharon Weiss and Prof. Richard Haglund for coursework and discussions which were absolutely vital to my development as a scientist.

It has been a privilege to work with so many incredibly talented scientists at Vanderbilt. In particular, I would like to thank all of my lab-mates in Prof. Caldwell's group: Prof. Thomas Folland, Dr. Ryan Nolen, Mingze He, Guanyu Lu, Scott Criswell, Ryan Kowalski, Katja Diaz-Granados, and Dr. Saurabh Dixit. It has been a true pleasure getting to know all of you, and I look forward to seeing your future successes.

This dissertation is a product of collaborations with a number of world-class scientists, many of whom have inspired and guided me through graduate school. In addition to the ones listed above, I would like to specially thank Prof. Alex Paarmann, Prof. Thomas Beechem, and Prof. Patrick Hopkins for countless discussions and mentorship.

I owe a special thanks to Sarah Ross, Alisha McCord, Jamie Kuntz, Myrtle Daniels, and Sarah Nagy for immense help and support during my PhD. I would also like to thank Dr. Alice Leach, Dr. Bill Martinez, Dr. Christina McGahan, and Kurt Heinrich for supporting and training me in the cleanroom.

Finally, I want to give enormous thanks to my family, my partner Emilie, and her parents. I can't imagine my time at Vanderbilt without your constant support and encouragement.

This dissertation would not have been possible without the generous funding provided by the United States National Science Foundation (DMR-1904793) and the Office of Naval Research (N00014-22-1-2035).

TABLE OF CONTENTS

Page

ACKNOWLEDGMENTS ..... **iv**

LIST OF TABLES ..... **vii**

LIST OF FIGURES ..... **viii**

CHAPTER 1 Introduction **1**

1.1 Nanophotonics – Confining and Manipulating Light 1

1.2 Polaritons for Infrared Nanophotonics 3

1.3 Coupling to polaritons 6

1.4 Anisotropy for Controlling Light 8

1.5 Dissertation Overview 10

CHAPTER 2 Hyperbolic Phonon Polaritons in Hexagonal Boron Nitride **12**

2.1 Hyperbolic Polaritons in Natural Crystals 12

2.2 Reconfigurable Infrared Hyperbolic Metasurfaces using Phase-Change Materials 14

2.3 HPhP Design and Modulation in vdW / Doped Semiconductor Heterostructures 19

2.3.1 Substrate Engineering of HPhPs 20

2.3.2 Concept of tuning HPhPs via substrate permittivity 22

2.3.3 Modal order transition 26

2.3.4 Ultrafast HPhP Modulation 28

2.3.5 Conclusions 31

2.4 Photothermally Probing HPhP Absorption at the Nanoscale 32

2.4.1 Mapping and Spectroscopy of Non-Radiative Hyperbolic Modes 33

2.4.2 High-Q Dark HPhPs in hBN Nanostructures 41

2.4.3 Using PTIR to Confirm Long HPhP Lifetimes in Isotopic $h^{10}BN$ 51

CHAPTER 3 Nanophotonics in Lower Symmetry Crystals **67**

3.1 Impact of Crystal Symmetry on Nanophotonics 67

3.2 Hyperbolic shear polaritons in low-symmetry crystals 70
3.3 Controlling the Asymmetric Propagation of HShPs in bGO 87
CHAPTER 4 Engineered Uniaxial Materials for Nanophotonics 101
4.1 Effective Anisotropy in Layered Materials 101
4.2 Controlling the IR Dielectric Function through Atomic-Scale Heterostructures 102
4.3 Optical Phonon Confinement Modifications to the IR Dielectric Function 116
CHAPTER 5 Conclusions and Future Directions 132
5.1 hBN Devices 132
5.2 Low Symmetry Crystals 132
5.3 Engineered Anisotropy 134
5.4 Closing Perspective 134

LIST OF TABLES

Table Page

Table 4.1 Phonon mode best-fit parameters of ellipsometry data using Eq. (4.3). 108

LIST OF FIGURES

Figure Page

Figure 1.1 Schematic of the different types of polaritons in van der Waals crystals [from ref. [27]]..... 4

Figure 1.2 Phonon dispersion curves in GaSb along high-symmetry axes. The continuous lines were calculated from ab initio electronic structure theory calculations. The horizontal axis markers correspond to the Brillouin zone boundaries. 5

Figure 1.3 Polariton dispersion and methods for coupling. a) The polariton dispersion of a polar semiconductor. b-f) Methods for overcoming the momentum mismatch between free-space light and the polariton. b) and c) illustrate coupling through a high-index prism in Kretschmann (b) and Otto (c) configurations. Alternatively, scattering to provide higher momenta can be achieved through gratings (d), nanostructures (e), or commonly through a metal-coated AFM tip for s-SNOM measurements (f). [a-e from ref. [35]] 6

Figure 1.4 Material anisotropy and the resulting optical and nanophotonic properties. a-c) Diagrams of refraction and birefringence in isotropic, uniaxial, and biaxial systems, with permittivity tensors shown below. d-f) Isofrequency contours and schematic of polariton propagation for the material systems in a-c, when the permittivities meet the criteria given underneath. 9

Figure 2.1 Hyperbolic polaritons and hexagonal Boron Nitride. Isofrequency contours for polaritons in a) isotropic, b) Type I hyperbolic, and c) Type II hyperbolic media. The green arrow tangential to the surface represents the group velocity vector. d) Real parts of the permittivity tensor components of hBN. The Type I lower and II upper Reststrahlen bands are shaded. A schematic of the hBN crystal structure is presented in the inset. e) Polariton dispersion calculated in transfer matrix for a 200nm thick flake of hBN on silicon. Color scale is the imaginary component of the p-polarized reflection coefficient. [a-d from ref. [45]]..... 13

Figure 2.2 Actively reconfigurable hyperbolic metasurface device. a) A device and experimental schematic, in which hBN has been transferred on top of a VO_2 single crystal and polaritons are imaged by the s-SNOM tip. b) An optical microscope image of the heterostructure. c–e) s-SNOM images of the optical near-field at 1450 cm^{-1} (6.9 μm) at various temperatures, showing HPhPs propagating over both metallic and dielectric VO_2 domains. The complex patterns that form are the consequence of multiple interfering waves over the different domains. The different colored arrows indicate the polariton propagating in different media (Purple – launched by hBN edge, Blue – launched from edge of VO_2 crystal, Orange (Green) – launching from VO_2 phase boundary into dielectric (metallic) phase VO_2). f) An electromagnetic-field simulation of the refraction across a VO_2 phase boundary. g) Line profiles from f showing the refraction of the wave. [from ref.[66]] 17

Figure 2.3 Tuned HPhP dispersion of hBN/doped semiconductor heterostructure by controlling semiconductor ωp. (a) Schematic of the platform. For the same hBN, the HPhP wavelength changes as a function of the plasma frequency of semiconductor. In this example, the right side (magenta color) is highly doped, shrinking the polariton wavelength. (b-d) Dispersion plots of hBN over InAs of different

plasma frequencies. The plasma frequencies are noted on the corresponding panels, and the thicknesses of hBN are 51, 51 and 55 nm, respectively. The contour plots and dashed curves are calculated by transfer matrix method (TMM) and Eq. (2.3), respectively, and the triangles are extracted from s-SNOM data. .. 23

Figure 2.4 Full control of kHPhP with doped semiconductors. The normalized kHPhP varies with the |Re(εs)| of the substrate. All curves are calculated by Eq. (2.3), while all symbols are experimental data. Colored shadows indicate the tunable range of kHPhP with that substrate with achievable doping. Solid symbols represent fundamental modes, while open symbols represent high-order modes. Data with dielectric (metallic) InAs are plotted with black (purple) symbols. Data with metallic CdO are plotted with purple rectangles. Note that all noble metals actually lead to nearly identical kHPhP, and the color box on the y-axis is extended for visualization purposes. Due to the accessible carrier concentration and high-frequency permittivity values, the tuning range of |Re(εs)| of InAs and CdO are -10 to 10, and -100 to -2, respectively. 24

Figure 2.5 Modal order transition of HPhPs in hBN/InAs heterostructure. (a) The relationship between normalized kHPhPs and InAs ωp. All curves are calculated by Eq. (1), while all symbols are experimental data. Solid symbols represent fundamental modes, while open symbols represent high-order modes. Data with dielectric (metallic) InAs are plotted with black (purple) symbols. The colored shades indicate whether InAs behaves as dielectrics or metal. (b) The modal order transition observed in the frequency domain. The contour plot is calculated by TMM and triangles are experimental data. (c) kHPhPs ¬at different wavenumber and InAs ωp, with larger kHPhPs ¬plotted with larger color. A clear modal order transition is observed when InAs ωp passes the Reststrahlen band of hBN. 27

Figure 2.6 Ultrafast modulation of HPhPs. (a) The line profile extracted from pump-probe nano-FTIR scans at different time delay. The noisy curves are raw data, and we then applied FFT filters to remove the noise and the filtered data are plotted with thick lines over raw data. (b) The ultrafast nano-FTIR probed at a constant spatial position (~ 0.7 μm from the edge, k≈5×104 cm-1). The data here are processed with FFT filters to remove noise, and the raw data and signal process can be found in SI, section 7. (c) The ultrafast nano-FTIR measurements on InAs substrate. The reflection dip position is related to the plasma frequency of InAs. The InAs static plasma frequency is 1050 cm-1, and the hBN thickness is 55 nm. 31

Figure 2.7 a) Schematic of the PTIR experiment. A pulsed tunable IR laser illuminates the portion of the sample (region highlighted in pink centered around gold-coated AFM probe operating in contact mode). b) AFM topography (scale bars 300 nm) and c) corresponding tilted SEM images (scale bars 1.0 μm) of five representative frustums with different aspect ratio. All the frustums have a thickness of 256 nm ± 4 nm. d) PTIR absorption spectra (p-polarization) obtained by positioning the AFM tip at the center of representative frustums, as indicated in panel b. The schematic of the incident polarization used for the measurements is provided as an inset. e) Color coded position dependent PTIR absorption spectra for the A_r = 4.39 frustum. The spectra in panel d and e are displayed with an offset for clarity. 36

Figure 2.8 a) Analytical calculations of the HPhP dispersion for hBN ellipsoidal particles as a function of the Ar. Four specific 'limbs' are observed with multiple dispersing polaritonic modes. The gray-scale represents the corresponding Purcell factor, while the colored lines are provided as a guide to the eye and identify the l10 (orange traces), l11 (red traces), l01 (green traces) and l02 (blue traces) limbs of the Ar-dependent HPhP dispersion for hBN ellipsoidal particles. b) PTIR (full symbols) and FTIR (open symbols) experimental Ar-dependent dispersion from each of the five frustums measured in Fig. 1b. The modal assignments are in good qualitative agreement with the analytical calculations. The color lines and symbols, along with the (lmn) designations are provided for easier comparison with the calculations. The dispersion of the three observed resonances within the far-field reflection are also provided as the open circles and correspond to the (110), (210) and (310) branches. The error bars represent a single standard

deviation of the resonance peak position uncertainties determined by the least-squares fitting algorithm. Some uncertainties are smaller than the dot size. 39

Figure 2.9 a) Contact-mode and b) tapping-mode PTIR absorption maps for an hBN frustum of A_r = 4.65 ± 0.11. All images (5 nm pixel resolution) were obtained with a scan rate of 0.5 Hz using the same AFM cantilever (probe-A). c) Contact mode PTIR absorption spectra obtained at the color-coded positions marked in the inset. The spectra were smoothed by considering 7 adjacent points and are displayed in common scale and with an offset for clarity. The inset displays the AFM deflection image of the frustum. Scale bars are 250 nm 45

Figure 2.10 a-i) Tapping-mode PTIR absorption maps for an hBN frustum of Ar = 1.16 ± 0.03. All images (3 nm and 7.5 nm pixel resolution in the horizontal and vertical directions respectively) were obtained with a scan rate of 0.6 Hz using probe-B. Scale bars are 100 nm. j) Line cuts of the PTIR images along the direction indicated by the white line in panel-i. k) Tapping-mode PTIR spectra obtained at the color-coded position in panel-a. The spectra are displayed in full scale with an offset for clarity. l) Q-factors of the polariton resonances obtained from the color-coded spectra in panel-k. The error bars represent a single standard deviation in the determination of Q and mainly determined by the uncertainty of determining the peaks FWHM via the least square fitting the resonances with Lorentzian peak shapes. 47

Figure 2.11 a) Comparison of the experimental PTIR spectrum (black) and simulated power loss spectrum (red) obtained by positioning the AFM tip in the center of an isolated frustum of Ar ≈ 1.16. b) Simulated PTIR spectra in the center of an Ar ≈ 1.16 frustum as a function of tip-sample distance. c) FDTD integrated power loss spectra as a function of tip radial location (corresponding to Figure 2.10k). Spectra are shown from the center of the frustum (bottom) to 300 nm away from the center, in 20 nm increments. d) Comparison of line cuts from PTIR scans of an Ar ≈ 1.6 frustum (Figure 2.10j) on the left, to the corresponding line cuts from FDTD simulations on the right, demonstrating agreement in spatial mode profile. Frequencies of line cuts are chosen for the peak center positions in the center experimental and simulated spectra identified in panel a) 49

Figure 2.12 a) Schematic of the sample illumination in photothermal induced resonance (PTIR) experiments. Infrared light (red arrow with wavevector q_{IR}) is incident upon the sample at an angle of α with respect to the plane of the sample, and an angle β with respect to the flake edge. b) Real-space PTIR images of hyperbolic phonon polaritons (HPhPs) in an isotopically enriched ($^{10}B \approx 99$ %) hBN flake (≈ 147 nm thick) obtained by illuminating the sample with different wavelengths. The scale bars represent 5 μm. c) Representative column-wise averaged absorption line profile (measured at 1480 cm^{-1}) as a function of the flake edge (x = 0) distance. d) Discrete Fourier transform (DFT) of the absorption line profile in (c) revealing multiple HPhP excitation modes at distinct spatial frequencies. 54

Figure 2.13 Comparison of the as-measured hyperbolic phonon polariton (HPhP) wavevectors, q (obtained from PTIR imaging analysis), with the calculated dispersion curves based on the dielectric function of the isotopically enriched $^{10}B \approx 99$ % hBN. Results are presented for flakes with thicknesses a) ≈ 147 nm and b) ≈ 337 nm. The experimental data (solid circles) show dispersing branches with progressively increasing momenta and are labelled as Edge-1, Tip-1 and Edge-2. Two low frequency modes are also detected and labelled as 0, 0′. The imaginary component of the computed reflectivity, Im r_p, is represented in the underlying colormap and is used as a proxy for the theoretical HPhP dispersion. 57

Figure 2.14 a) Schematic illustrating sample illumination scheme in photothermal induced resonance (PTIR) experiments. Infrared (IR) light (red arrow with wavevector q_{IR}) is incident upon the sample at an angle of α with respect to the plane of the sample, and an angle β with respect to the flake edge. The magnified schematic outlines the in-plane and normal components of the p-polarization (p-pol) light. b)

Representative comparison of PTIR and s-SNOM column-wise averaged line scans at different incident IR frequencies. c) Discrete Fourier transform (DFT) of s-SNOM line profile revealing the HPhP spatial frequencies. d) Comparison of extracted hyperbolic phonon polariton (HPhP) wavevectors, q, obtained from s-SNOM imaging to the calculated dispersion curves based on the [^{10}B] 99.22 % hBN dielectric function with 147 nm thickness. 61

Figure 2.15 a) Propagation lengths, L_p, for Edge-1 polaritons in a ≈ 147 nm thick ^{10}B ≈ 99 % hBN flake via PTIR (open circles) and s-SNOM (open squares). Propagation lengths are plotted as a function of the genuine in-plane wavevector, q, and compared to previous s-SNOM measurements[27] for a ≈ 120 nm thick ^{10}B 98.7 % hBN flake (solid blue) and natural abundant hBN (solid purple). b) Propagation lengths for Edge-1 (red circles), and Edge-2 (black circles) branches as identified in Fig. 2b for a ≈ 337 nm thick ^{10}B ≈ 99 % hBN flake, as a function of q. The error bars represent the propagated uncertainty in the values of the fitted parameters (95% confidence intervals) used to calculate the propagation length. 62

Figure 2.16 a) Figure of merit, Q, representing the quality of the polaritons and b) lifetimes, τ, for ^{10}B ≈ 99 % isotopically enriched hBN flakes with thickness of ≈ 147 nm estimated via PTIR (open red circles), s-SNOM (open blues squares) and compared to previous s-SNOM measurements for a ≈ 120 nm thick flake of similar composition (^{10}B 98.7 % hBN, solid blue squares). The error bars represent the uncertainty propagation of the fitting parameters (95% confidence intervals) used to calculate the Q and lifetime. 63

Figure 3.1 Crystal structures and resulting permittivity tensors for a) cubic, b) tetragonal, trigonal, hexagonal, c) orthorhombic, d) monoclinic, and e) triclinic crystal systems..... 67

Figure 3.2 MoO3 dielectric function and hyperbolic polaritons. a) Orthorhombic structure of MoO_3. b) Microscope image of MoO3 crystal, with outlined area measured in FTIR microscope for dielectric function. c) Dielectric function of MoO3 extracted from FTIR measurements and from ab initio theory. d-e) Schematic of polaritons launching from a s-SNOM tip and from a simulated dipole. f-g) In-plane hyperbolic phonon polaritons imaged in s-SNOM (f) and in COMSOL simulation using the experimentally extracted dielectric function. h-i) Elliptical phonon polaritons imaged in s-SNOM and COMSOL simulation. [from ref. [182]] 68

Figure 3.3 Hyperbolic shear polaritons in monoclinic β-gallium oxide (bGO) compared to hyperbolic polaritons in uniaxial α-quartz (aQ). (a) Monoclinic crystal structure of bGO (monoclinic angle $\beta = 103.7°$). The sample surface of the investigated bGO crystal is the monoclinic (010) plane (x-y-plane) (b) Rhombic unit cell of aQ with the c-axis oriented along the x-direction, lying in the sample surface plane. The Cartesian coordinate system used in this work is shown. (c,d) Isofrequency surfaces for bGO and aQ, respectively, at two frequencies (red and green) where the material supports hyperbolic polaritons. The contour lines at $kz = 0$ are plotted as solid lines at the bottom, and their mirror axes are shown as dash-dotted lines. (e,f) Real-space electric fields at the bGO and aQ surface, respectively, and (g,h) the respective two-dimensional Fourier transformation. Lines indicate the frequency dependent optical axes for bGO and the crystal axes for aQ. The fields were calculated using COMSOL Multiphysics[314] 73

Figure 3.4 Experimental observation of HPs on aQ and HShPs on bGO. (a) Otto-type prism coupling configuration for the experimental observation of surface waves. The p-polarized free-electron laser (FEL) excitation beam is reflected at the prism back side at an incident angle of $\theta = 28°$. The reflectance detection is unpolarized. The gap size was fixed to $dgap \approx 10.4$ μm for aQ, and $dgap \approx 8.3$ μm for bGO. (b) Experimental azimuth dependence of HPs on aQ, and (c) corresponding simulated reflectance map calculated by means of a transfer matrix method[271]. (d) Experimental azimuth dependence of HShPs on bGO, and (e) corresponding simulated reflectance map. The white lines in (e) correspond to the directions of the frequency-dependent major polarizability axes n and m, see text. (f) Polariton resonance frequency

map for bGO in the 680-720 $\mathrm{cm}-1$ frequency range, extracted from Otto reflectance measurements at various incidence angles θ and azimuth angles Φ at constant gap size $\mathrm{dgap} \approx 4.0$ μm. (g) In-plane hyperbolic dispersion for bGO at selected frequencies interpolated from (f). Dashed lines and symbols mark extrapolated values outside the accessed momentum range. 77

Figure 3.5 Symmetry breaking by shear dissipation for hyperbolic polaritons in monoclinic bGO. (a-c) Real-space electric fields at the bGO surface for three different magnitudes of the off-diagonal permittivity element i f $\mathrm{Im}\varepsilon\mathrm{mn}$ calculated in the frequency-dispersive rotated coordinate system at $718\ \mathrm{cm}-1$, and (d-f) respective Fourier transformation k-space maps in arbitrary units. The thin crosshairs indicate the principal axes in the frequency-dispersive rotated coordinate system, aligned horizontally and vertically because the maps were calculated within the rotated coordinate system [mnz]. (g) Isofrequency surface of bulk eigenmodes in bGO with complex frequency $\omega = \omega/\mathrm{k0} = 1 + \mathrm{i}\ \omega\mathrm{i}/\mathrm{k0}$ calculated in the rotated frame for $\mathrm{f} = 0, 1$ (red and blue, respectively). (h) Imaginary part ωi for $\mathrm{f} = 0, 1$. (i) Contour lines of the isofrequency surface at $\mathrm{kz} = 0$ for $\mathrm{f} = 0, 0.5, 1$. The imaginary part ωi at the corresponding point in k-space is color-coded. 80

Figure 3.6 Propagation losses as function of shear dissipation scaling. (a) Extracted propagation length from COMSOL field patterns for various values of the scaling factor f, see main text. The decay lengths of the surface waves were fitted for all azimuthal directions, and the maximum value was taken for each f. (b) Minimum loss $\min(-\omega\mathrm{ik0})$ at $\mathrm{kz} = 0$ for analytical solutions of the complex frequency calculations as a function of the shear dissipation scaling factor f, compare Fig. 3i. Both calculations predict systematic reduction of propagation losses with increasing f, i.e. going from the artificial biaxial to the natural monoclinic bGO. All calculations were performed at $718\ 1/\mathrm{cm}$. 84

Figure 3.7 Active tuning of the propagation direction of HShPs in bGO. Rotation angle γ (Eq. 2 of the main text) calculated as a function of doping concentration N (in cm^{-3}), assuming a Drude contribution with anisotropic charge carrier mobility, μ_x=296 $\mathrm{cm}^2\mathrm{V}^{-1}\mathrm{s}^{-1}$, μ_y=μ_z=37 $\mathrm{cm}^2\mathrm{V}^{-1}\mathrm{s}^{-1}$. (Literature values of μ in bGO feature a large variance[315]. We here assume strong anisotropy of the charge carrier mobility in order to emphasize the rotation mechanism.) Clearly, between the TO frequencies where the HShPs disperse, the rotation angle γ is strongly dependent on the doping concentration, enabling active tuning of the propagation direction of the supported polariton modes. Note that for an isotropic Drude contribution, on the other hand, Eq. 2 predicts no rotation of the propagation direction as a function of doping concentration. 85

Figure 3.8 Real-space imaging of HShPs launching from infrared antenna on the surface of bGO observed via FEL-coupled s-SNOM. **(a)** Schematic of FEL-coupled near-field imaging experiment. **(b)** Experimental near-field image of HShPs launched by a 2 μm gold disc by the incident FEL beam (oriented along the dashed white line) at a frequency of 712 cm^{-1}. **(c-d)** Finite element modeling of HShP launched by a 2 μm gold disc under similar launching conditions to the experiment shown in (b), in real-space (c) and Fourier space (d). Red dashed curves denote the dispersion of HShPs calculated from theory. 90

Figure 3.9 Dependence on illumination orientation of HShPs in a bulk bGO crystal. (a-e) Experimental near-field images of HShP propagation, launched by a 2 μm gold disc at a frequency of 712 cm^{-1}, with FEL illumination rotated in 45-degree steps, as illustrated by white dashed line. (f-j) Finite element modeling of HShP propagation from gold disc, with illumination conditions similar to (a-e). (k-o) Fourier transforms of (f-j), illustrating the shear asymmetry in the polariton propagation. The red dashed curves in k-o are the dispersion of HshPs calculated from theory. 92

Figure 3.10 Momentum dependence of HShPs computed analytically and probed by illuminating gold resonators of different size. (a-c) Experimental near-field images of HShP propagation, launched by a

(6,4,2) μm gold disc at a frequency of 720 cm^{-1}, with illumination incident from the lower left corner. (d-f) Fourier transform of the experimental images in (a-c), with a zero-filling factor = 5. g-i) Finite element modeling of HShP propagation from gold discs to match experiment (a-c). j-l) Fourier transforms of (g-i). m) Schematic for extracting the HShP figure of merit (FOM) as a function of the launcher radius from the k-space dispersion. n) Analytical FOM dependence on the launcher radius – extracted by integrating the damping rate along the path of HShPs dispersion which is cut off in momentum determined by the launcher radius. o) Dependence of FOM on the launcher radius, extracted from Fourier transforms of the experimental and simulated field profiles (a-c, g-i). 95

Figure 3.11 Frequency dependent rotation of HShP propagation. a) Schematic of the frequency-dependent rotation of the polariton axis, with hyperbola arms in upper left. b) Plot of the permittivity rotation angle γ, with TMM calculation of the polariton peaks for the different gold disc sizes, marking the opening angle of the hyperbolic dispersion across the HShP range. Transparency of TMM calculations is given by the peak intensity of Im(rpp) divided by the maximum peak intensity for a given azimuthal angle. c-e) Rotated polariton axis plotted, as in (a), against c) Near-field images of HShPs launched by a 1 μm diameter gold disc, at varying frequencies (Scale bar = 2 μm). d) Near-field images of HShPs launched by a 2 μm diameter gold disc, at varying frequencies (Scale bar = 5 μm). e) Near-field images of HShPs launched by a 4 μm diameter gold disc, at varying frequencies (Scale bar = 5 μm). Upper left of c,d,e show the arms of the hyperbolic dispersion as extracted from b. 98

Figure 4.1 STEM images and reflectance of AlN/GaN heterostructures and Reststrahlen bands. a) Illustration depicting AlN/GaN heterostructures. b) Calculated reflectance of bulk GaN, AlN, and SiC for normal incidence light in the IR, showing the spectral overlap of the Reststrahlen bands. c) and e) display cross-sectional high-angle annular dark-field STEM images of AlN/GaN heterostructures with AlN (GaN) thicknesses of ~2.2 nm (2.2 nm) for Sample A and ~1.2 nm (1.4 nm) for Sample B, respectively. The AlN layers appear as dark-gray bands, and the GaN layers as light-gray bands. d) and f) show the measured reflectance spectra (blue line) at an incidence angle of 65° and the calculations (orange dashed lines) based on the bulk properties of the AlN/GaN SL from c) and e), respectively. 106

Figure 4.2 Dielectric function of the atomic-scale AlN/GaN SL. a-b) measured, c-d) calculated using DFPT, and e-f) calculated using effective-medium theory real and imaginary parts of the dielectric function of the AlN/GaN SL (Sample B). The in-plane component, ε ⊥, and the out-of-plane component, ε ∥, are shown in blue and orange, respectively. Highlighted areas in a) mark the hyperbolic regions of type I (light gray) and type II (dark grey). g) and h) phonon vibrational patterns associated with the 559-583 cm^{-1} and 615-784 cm^{-1} Reststrahlen bands, respectively, for ε ⊥ shown in c). Blue, orange, and gray spheres denote Ga, Al, and N, respectively, and red arrows denote atomic displacement. 109

Figure 4.3 Theoretical polariton dispersion and strongly confined phonon polaritons of the XH. a-b) Imaginary part of the Fresnel reflection coefficient for p-polarized light Im(r_p) of Sample B for evanescent wave excitation as a function of the relative in-plane momentum k/k_0. The dashed lines represent the modes extracted from calculations with reduced damping. The red dots in a) mark the positions of the reflectance dips in the Otto geometry experiments. Hyperbolic mode progression is observed in b) for all three type-I hyperbolic regions. Additionally, one type II hyperbolic mode and a strongly elliptical mode are observed as indicated. c-f) Spatial electric field profiles for localized excitation of hyperbolic modes of type I (c,e,f) and type II (d). The mode shown in e) exhibits a rigid angle of propagation close to zero, since here the positive epsilon component ε ⊥is nearly zero. 113

Figure 4.4 Superlattice Diagram. A) Crystal structure of GaSb and AlSb unit cells. b) Diagram of 2ML/2ML superlattice. c) Bulk Reflectivity of constituent materials. d) Bulk phonon dispersion plots along the Γ-X Brillouin zone (superlattice direction) of GaSb (red) and AlSb (blue). 120

Figure 4.5 Phonon confinement in 4 ML GaSb /4 ML AlSb superlattice. a) schematic of 4 ML/4ML superlattice, with atomic displacement shown for m=1 mode. Multiple δ values are shown, indicating the meaning of the interface leakage term. b) Raman spectra of 4ML/4ML superlattice, with single LO phonon (LO_1) observed in the AlSb range, and 2 LO phonon peaks observed in the GaSb range (LO_1, LO_2). c-d) Real (c) and imaginary (d) permittivity for the 4ML GaSb and AlSb layers, in the ordinary and extraordinary axes, compared to the bulk dielectric function (black).e) Bulk dispersion curves for GaSb and AlSb, calculated in DFT, with overlaid phonon frequencies from Raman (green squares) and FIR-SE (circles). 121

Figure 4.6 Exploring thickness dependence of phonon confinement. a) FTIR reflectance spectra of superlattices with 20ML AlSb alternating with varying thicknesses of GaSb. b) Ordinary dielectric function of GaSb layer at varying GaSb layer thicknesses, as extracted from FTIR studies. c) Extraordinary dielectric function of GaSb layer at varying thicknesses. d) Raman measurements of confined GaSb phonons for varying GaSb layer thicknesses. e) Confined phonon peaks from Raman (d), plotted against the confined phonon dispersion (dashed lines). Measurements of the 4ML/4ML superlattice from Fig. 2 included as stars. f) Ordinary phonon frequencies from (b), plotted against the confined phonon dispersion (m=1). Phonon frequencies from ellipsometry (Fig. 2) plotted as stars. 126

Figure 4.7 High-resolution momentum resolved inelastic X-ray scattering to probe the superlattice phonon dispersion. a) Schematic of mechanically thinning the substrate supporting the superlattice sample (The sample was not mounted on a cooper post during dicing, it was mounted on a copper post during the measurements) . b) Inelastic X-ray scattering spectrum, with peak-fits showing the elastic (zero loss) peak, the longitudinal acoustic phonon peak, and longitudinal optical phonon peak, at 0.2 reduced momentum in the Γ-X Brillouin Zone. c) LO and LA phonon peaks observed in inelastic X-ray scattering of bulk GaSb (black triangles), the 4ML superlattice from Fig. 2 (red circles), and a 6ML GaSb/ 6ML AlSb superlattice (green squares) Overlaid on LO and LA dispersions of bulk GaSb (blue dashed lines) and bulk AlSb (red dashed lines) . d) DFT phonon dispersion of 4ML GaSb/ 4ML AlSb superlattice, with overlaid IXS LO phonon peaks..... 129

CHAPTER 1

Introduction

Throughout history, improvements in our ability to control light have driven scientific and technological advancement. Notable examples include the use of sundials to make the first measurements of time, early optical microscopes proving the existence of cells and beginning the modern era of biological sciences, and fiber optics connecting the globe at nearly instantaneous speeds. For some applications, modern optical systems allow for remarkable levels of optical control, approaching the physical limits on speed and resolution. However, for many applications there are significant improvements to be made.

The broad underlying motivation for the body of work described in this dissertation is improved control of light in the infrared region, where current technology is limited. Through the approaches to be described, we have demonstrated the ability to control the behavior of infrared light at dramatically reduced length- and timescales, with greater efficiency and fidelity. While we have approached these topics from largely fundamental angles, the outcomes of these efforts offer distinct new paths for future applications in chemical sensing, beam steering for on-chip optics and computing, and next-generation infrared optical components.

1.1 Nanophotonics – Confining and Manipulating Light

The field of nanophotonics pursues a singular goal – to squeeze light down to smaller and smaller length-scales and control its behavior with nanoscale precision. This goal has remarkably broad implications, ranging from single molecule sensing[1–4] to single-chip computers[5,6]; light-speed data transmission[6,7] to near-speed-of-light space travel[8,9]. On a more near-term scale, such improvements in the control of light propagation at the nanoscale are crucial for miniaturizing conventional optical components[10–12], and for achieving new applications such as on-chip

optics[7,13–15], surface enhanced chemical sensing[3,16–19], quantum applications[20–23], and optical computing[6,13,15,24].

While there is significant motivation for using nanophotonic metamaterials in visible applications such as smaller smartphone cameras, displays, or augmented reality glasses – for most applications the infrastructure of visible optical technology is too well developed for nanophotonic alternatives to provide much benefit. However, the ability of nanophotonics to shrink light to smaller scales becomes more appealing at longer optical wavelengths. This benefit is best described by Ernst Abbe's diffraction limit – which approximates the minimum resolvable feature size by an optical microscope (d) as a function of the free-space wavelength (λ) and the numerical aperture (NA), which convolves the refractive index (n) of the medium and the largest angle of light which enters the lens (θ).

$$d = \frac{\lambda}{2NA}, \qquad NA = n\,sin\,(\theta) \tag{1.1}$$

This approximation provides a rule of thumb that the smallest resolvable feature size is approximately the wavelength used for imaging. In the visible, this ranges from 380-700 nanometers – sufficient resolution to image down to the scale of bacteria and large molecules. However, in the infrared (IR) spectral range – which is host for applications including chemical sensing and spectroscopy, communications, and thermal imaging – this lower limit pushes into tens of micrometers, significantly limiting conventional optical approaches.

In addition to the fundamental physical limitations of optical systems in the IR, this range is also plagued by device and material limitations. Narrowband optical sources are limited to expensive, large-footprint, inefficient gas-phase and quantum cascade lasers (QCLs), with limited bandwidth. Transparent optical materials are extremely limited – typically crystalline materials

which are either expensive and difficult to process (Germanium, Diamond, Sapphire), fragile (CaF_2, BaF_2), toxic (BaF_2, ZnSe), or degrade quickly in atmospheric conditions (KBr, BaF_2, CaF_2). Sensors in the IR typically suffer from low efficiency[25] or require cryogenic cooling. Therefore, the promise of nanophotonics for next-generation IR devices is high.

1.2 Polaritons for Infrared Nanophotonics

Among the most promising approaches for achieving the goals of nanophotonics in the IR spectral range is through the coupling of light to matter via so-called "polaritons", a quasi-particle formed when light is strongly coupled to the oscillation of an electromagnetic dipole in a material[26–29]. This coupled mode results from the boundary conditions at the interface of a metal-dielectric interface – and has a momentum given by the polariton dispersion relation:

$$k_p = k_0\sqrt{\frac{\varepsilon_m\varepsilon_d}{\varepsilon_m+\varepsilon_d}} \tag{1.2}$$

where ε_m refers to the permittivity ($\varepsilon = n^2$) of the metallic (polaritonic) material, ε_d refers to the permittivity of the surrounding dielectric material (typically air), and k_0 is the free-space wavevector that defines the light-line, equal to $\frac{2\pi}{\lambda} = \frac{\omega}{c}$. It is important to note that this polariton dispersion relation sets bounds on the polaritonic medium. The polaritons discussed here that are used for confining and manipulating light are supported by optically metallic materials, i.e., ε_m is negative. In order for the polariton dispersion to describe a real mode, $\frac{\varepsilon_m\varepsilon_d}{\varepsilon_m+\varepsilon_d}$ must be positive. Therefore, $\varepsilon_m + \varepsilon_d$ must be negative; so, a polariton is only supported at an interface where $\varepsilon_m \leq -\varepsilon_d$ (e.g., in air, $\varepsilon_m \leq -1$). This also means that $\sqrt{\frac{\varepsilon_m\varepsilon_d}{\varepsilon_m+\varepsilon_d}} \geq 1$, so the polariton wavevector k_p is always larger than the free-space wavevector, therefore the mode has a smaller wavelength

compared to light propagating through free-space. Additionally, this means that as ε_m approaches $-\varepsilon_d$, k_p asymptotically approaches ∞ (the polariton has an arbitrarily small wavelength in a lossless medium), and when $|\varepsilon_m|$ is large, k_p approaches k_0.

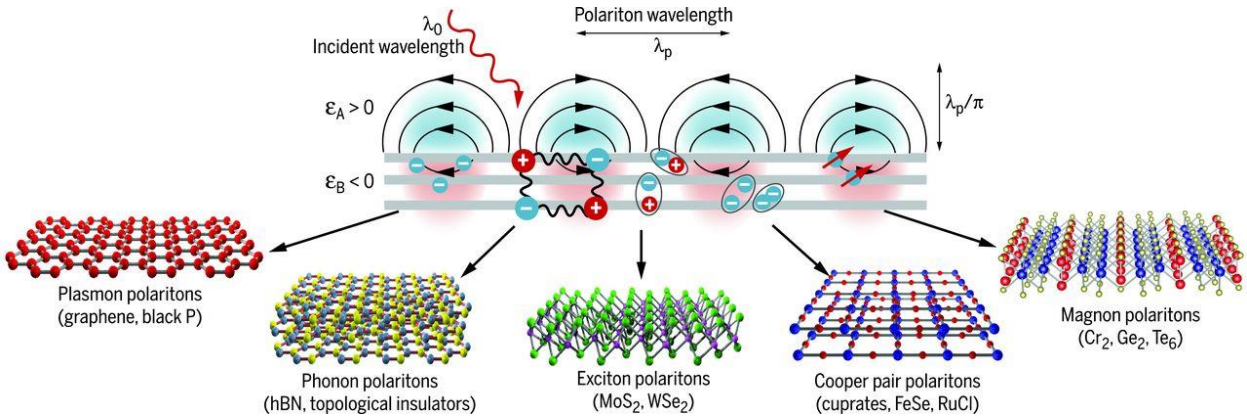

Figure 1.1 *Schematic of the different types of polaritons in van der Waals crystals [from ref. [27]]*

Many different types of electromagnetic dipoles can arise in a material, so there are many types of polaritons that can be supported (Fig. 1.1). The most studied is the surface plasmon polariton (SPP), where light couples with the free carrier plasma oscillations in a metal or doped semiconductor[28,30,31]. Plasmon polaritons benefit from ubiquity, as many materials host SPPs, ranging from the UV to the THz spectral ranges and beyond. There are some downsides to SPPs – the most critical is that they suffer from the high scattering rates of free carriers, resulting in significant losses and broad spectral linewidths for plasmon polaritons, limiting their efficiency in many applications. An alternative to SPPs in the IR are surface phonon polaritons (SPhPs, Fig. 1.1). Instead of light coupling to oscillations in a free carrier plasma, SPhPs involve the strong coupling of light to the optical phonons in a polar crystal[27,32,33].

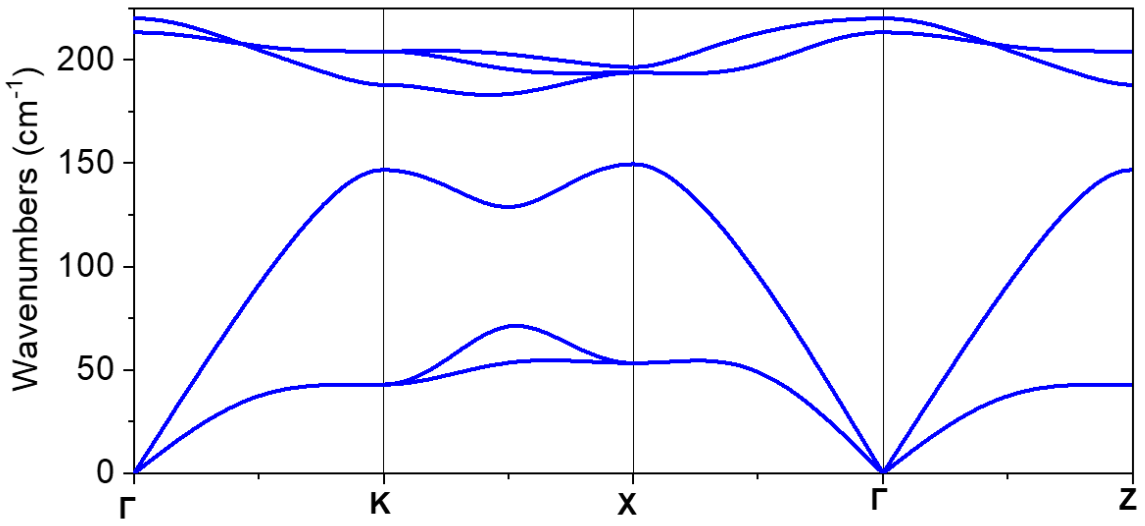

Figure 1.2 *Phonon dispersion curves in GaSb along high-symmetry axes. The continuous lines were calculated from ab initio electronic structure theory calculations. The horizontal axis markers correspond to the Brillouin zone boundaries.*

Phonons are quantized atomic vibrations in a crystal lattice. These vibrations can be separated into optical and acoustic phonons, which can be identified by their dispersion (Fig. 1.2). The phonon dispersion gives the relationship between phonon frequency (vertical axis) and wavevector along different crystal directions (horizontal axis). The acoustic phonon frequency goes to 0 at the Γ-point, where the wavevector is 0. Compared to phonon wavevector, photon wavevectors are essentially 0 – so the Γ-point describes the potential optical interaction of phonons. Hence, *optical* phonons are so named for having non-zero energy at the Γ-point, allowing them to interact with an electromagnetic field. We can further differentiate both acoustic and optical phonons into longitudinal and transverse modes – according to whether their displacements are perpendicular or parallel to the wave vector.

In nonpolar crystals, like silicon or germanium, charge is shared equally across atomic bonds, so the transverse optical (TO) and longitudinal optical (LO) phonons are degenerate at the Γ-point

and there is no electric dipole to couple to light. In polar crystals, like GaAs (Fig. 1.2), the bond is partially ionic – resulting in slightly charged atoms with a net electric dipole in the crystal. This allows the TO phonon to interact with light (a transverse wave) – with a contribution to the material's permittivity given by:

$$\varepsilon(\omega) = \varepsilon_\infty \sqrt{1 + \frac{\omega_{LO}^2 - \omega_{TO}^2}{\omega_{LO}^2 - \omega^2 - i\Gamma\omega}} \tag{1.3}$$

where ε_∞ is the high frequency permittivity, $\omega_{TO,LO}$ are the optical phonon frequencies, and Γ is the phonon damping rate. This dielectric function results in a negative permittivity between the TO and LO phonons called the Reststrahlen band, which allows for the formation of SPhPs[27,32,33]. Although SPhPs are limited to within the Reststrahlen band, they benefit from significantly longer lifetimes (~1-100 picoseconds) compared to SPPs (~10 femtoseconds)[32], owing to the slow scattering rates of phonons.

1.3 Coupling to polaritons

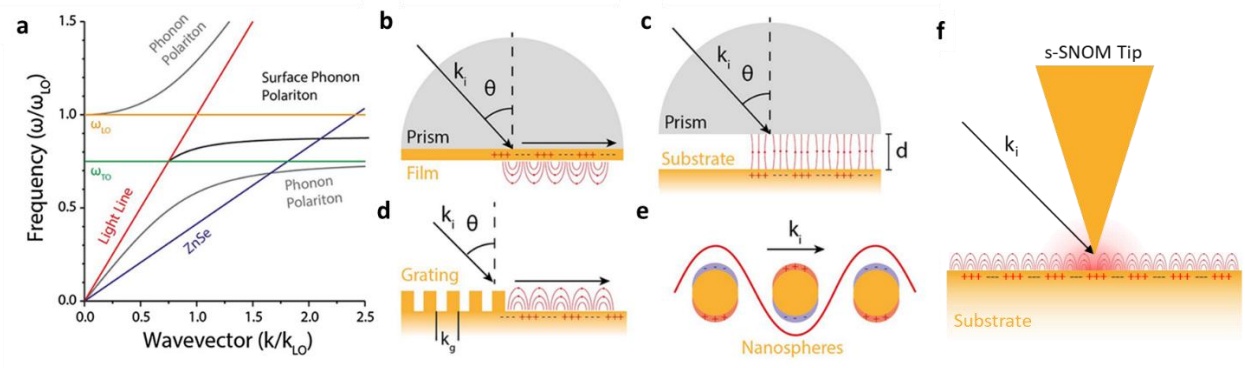

Figure 1.3 *Polariton dispersion and methods for coupling. a) The polariton dispersion of a polar semiconductor. b-f) Methods for overcoming the momentum mismatch between free-space light and the polariton. b) and c) illustrate coupling through a high-index prism in Kretschmann (b) and Otto (c) configurations. Alternatively, scattering to*

provide higher momenta can be achieved through gratings (d), nanostructures (e), or commonly through a metal-coated AFM tip for s-SNOM measurements (f). [a-e from ref. [35]]

The mismatch between k_p and k_0 provides the primary benefit of polaritons (shrinking the wavelength), but also presents a challenge for the stimulation, measurement, and application of these modes. In order to stimulate a polariton, either in a device or for measurement, the first law of thermodynamics requires us to match the energy and momentum of light to that of the polariton. If we look at the dispersion of a SPhP (Fig. 1.3a), it is clear that the free-space light line (red) does not intersect with the SPhP dispersion curve. However, there are a number of techniques we can use to manipulate the momentum of light and overcome the mismatch.

One method for "slowing down" light is to change the index of the propagation medium. The refractive index determines the slope of the light cone – so using a high index prism provides a light line at higher momentum which we can use to couple to polaritons (ZnSe in Fig. 1.3a). This still requires the metal-dielectric interface which supports the polariton to have a lower dielectric index than the prism, coupling with the evanescent field from attenuated total reflectance (ATR) inside the prism[12,29,36]. This method of prism coupling is achieved either with a thin polaritonic film on a low index substrate – with the prism in contact with the film ("Kretschmann configuration", Fig. 1.3b), or with a small gap between the prism and the polaritonic material, with a low index dielectric (like air) in between ("Otto configuration", Fig. 1.3c). By changing the prism index and the incident angle, the in-plane momentum of the evanescent wave can be tuned – allowing coupling to polaritons with momenta $k_{SP} = n_{prism} \sin\theta \, k_0$, where θ is the propagation angle of light within the prism. In the case of Otto configuration, the distance d between the prism and sample surface controls the efficiency of coupling via the degree of overlap of the evanescent fields.

Another route for accessing specific momenta in the polariton dispersion is to pattern a grating on the surface of a polaritonic material (Fig. 1.3d). Such a grating allows free-space light to couple to polaritons with momenta $k_{SP} = k_0 \sin\theta + \frac{2\,m\,\pi}{d}$, where d is the period of the grating, and m is an integer corresponding to the multiple diffractive momenta which allow coupling.

Polaritonic materials can also be patterned into subwavelength resonators, so that the wavelength of light shrinks to the resonator size. This allows coupling into polaritons with less defined momenta than the prism- and grating- coupling methods, but a large degree of tunability by changing the dimensions (Fig. 1.1e). This is one of the most common device types due to the ease of coupling with free-space light and various tuning abilities, through localized surface plasmon resonances in gold nanoparticles for example[23,37,38].

In a similar way, light can also be scattered from subwavelength objects in close proximity to a polaritonic surface to couple to a polariton without confining its propagation. This scattering can be done with metallic resonators, sharp steps or edges on the surface (e.g. van der Waals flake edges), or through a metal coated atomic force microscope (AFM) tip in close proximity to the material (Fig. 1.1 f). Scattering light off of an AFM tip forms the basis for scattering-type scanning near-field optical microscopy[33,39,40] (s-SNOM), a powerful technique which allows mapping of the electric field on the order of the AFM resolution, down to ~20nm, allowing deeply subdiffractional imaging of polariton propagation.

1.4 Anisotropy for Controlling Light

In most materials, we can describe the propagation of light through the material using the material's complex-valued refractive index n, or permittivity ε, as previously mentioned. This

permittivity value changes, or disperses, at different frequencies, but sufficiently describes the refraction (Fig. 1.4a), reflection, and absorption of light in the material. For anisotropic materials, however, the interaction with light depends on the orientation of the material, so we instead use a *permittivity tensor* to describe the interaction with light in different directions. In conventional optics, anisotropic materials – where the crystal structure (and resultant material properties) are different along different directions – are crucial for manipulating light[41]. In uniaxial materials, one axis exhibits a different permittivity from the others (Fig. 1.4b), splitting

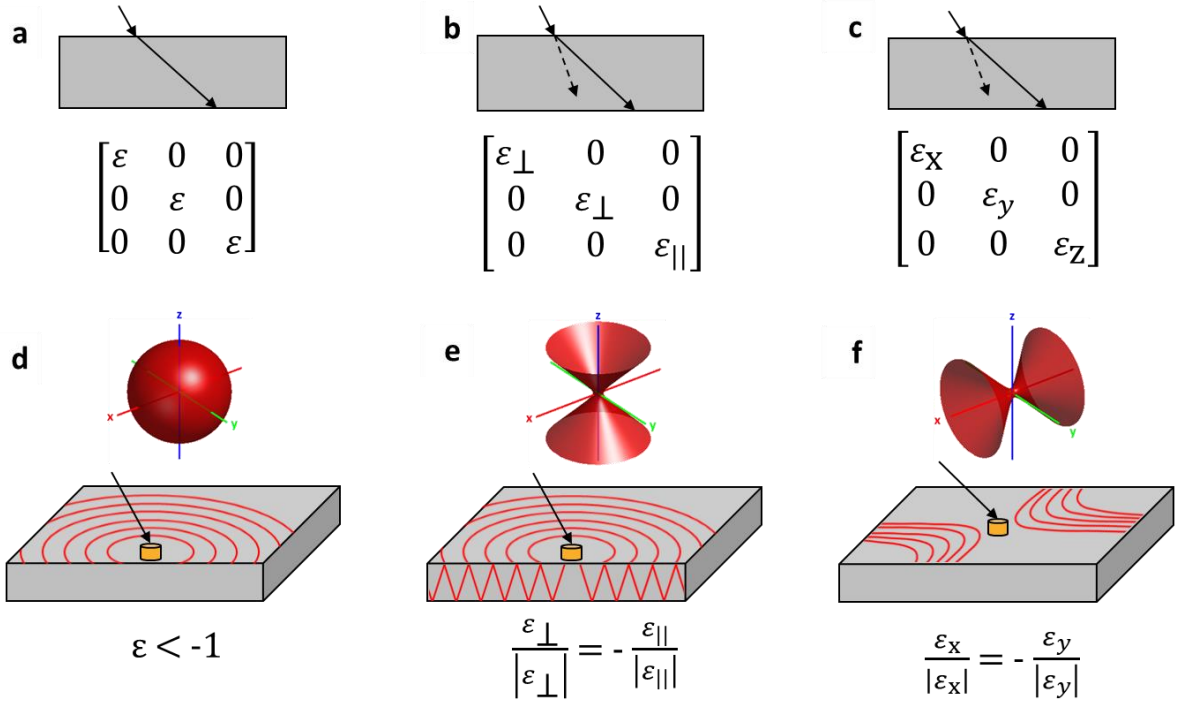

Figure 1.4 *Material anisotropy and the resulting optical and nanophotonic properties. a-c) Diagrams of refraction and birefringence in isotropic, uniaxial, and biaxial systems, with permittivity tensors shown below. d-f) Isofrequency contours and schematic of polariton propagation for the material systems in a-c, when the permittivities meet the criteria given underneath.*

light into an ordinary (solid line) and an extraordinary ray (dashed line), with different velocities, forming the basis for many polarizers, waveplates, and optical filters. In biaxial crystals, which have increased anisotropy (reduced crystal symmetry), the situation is more complicated, as light will still undergo birefringence, but with a varying extraordinary index depending on the crystal

orientation (Fig. 1.4c).

Despite the prevalence and utility of birefringent materials in visible optical applications, the level of birefringence is limited at visible wavelengths. The degree of birefringence, described by $\Delta n = n_e - n_o$, is on the order of ~0.25 for the most anisotropic crystals in the visible. In the infrared, however, the strongly dispersive optical phonon contribution to the dielectric function can result in extreme degrees of birefringence (>10 in hBN, Chapter 2), dramatically altering the SPhP behavior[42–45].

In a typical SPP or SPhP system, the polaritonic material is optically metallic in all directions, resulting in a surface polariton which propagates uniformly across the interface (Fig. 1.4d). In contrast, optical phonon frequencies along the anisotropic axes in uniaxial and biaxial crystals will often occur at different frequencies due to the different bonding, resulting in spectrally distinct Reststrahlen bands along different directions. In uniaxial systems, such as hexagonal boron nitride, this results in hyperbolic phonon polaritons, which propagate into the volume of the material (Fig. 1.4e) – offering new opportunities for tailoring the propagation of light which we will discuss in Chapter 2. Further anisotropic crystals offer greater control over the polariton behavior – such as in-plane hyperbolic polaritons in the orthorhombic crystal MoO_3 (Fig. 1.4f), and recently discovered shear hyperbolic polaritons in monoclinic crystals – discussed in Chapter 4.

1.5 Dissertation Overview

The objective of this dissertation is to gain new levels of nanophotonic control by leveraging the strong tie between crystalline anisotropy and infrared nanophotonics.

In **Chapter 2**, the prototypical hyperbolic phonon polaritons (HPhPs) of the uniaxial van der Waals (vdW) crystal hexagonal Boron Nitride (hBN) are explored with near-field microscopy techniques, developing a further understanding of the low-loss, volume-confined polaritons in flakes, nanostructures, and heterostructures. The inherent volume propagation of HPhPs enables low-loss interaction with the underlying environment, which we employ for sub-diffractional imaging, as a platform for engineering and modulating the polariton properties, and even enabling polaritonic refraction, and 2D refractive optics based on Snell's law.

In **Chapter 3**, I move beyond uniaxial systems to natural crystals with lower symmetry. I discuss biaxial orthorhombic systems, with the example of MoO3, which offer additional control of polariton propagation via in-plane hyperbolic polaritons. Reducing the crystal symmetry even further, I discuss the advantages of the pseudo-biaxial monoclinic crystal system with β-Ga_2O_3(bGO), where the non-diagonalizable permittivity allows a dramatic new degree of control of the propagation direction of the new "shear" polariton, as well as tunable asymmetric propagation.

In **Chapter 4**, I show that thin-film superlattices of polar dielectric materials offer a platform for engineering the effective anisotropy of the material, as well as tuning the phonon characteristics of the crystal, enabling low-loss elliptical and hyperbolic phonon polaritons with extreme dispersions. In addition, I explore the thin-film confinement of optical phonons and elucidate the underlying mechanisms of the phonon confinement phenomenon, as well as the impact on the dielectric function and phonon dispersion of the hybrid material.

Finally, in **Chapter 5**, I draw a brief conclusion for this thesis and a discussion of future directions in anisotropic nanophotonics.

CHAPTER 2

Hyperbolic Phonon Polaritons in Hexagonal Boron Nitride

2.1 Hyperbolic Polaritons in Natural Crystals

One approach while exploring the role of anisotropy on the optical and nanophotonic properties is to utilize and expand upon the existing toolbox of materials. There exists a multitude of materials with varying degrees of anisotropy. One set of materials known for strong anisotropy is the family of van der Waals (vdW) materials[27,46,47], which typically have strong covalent bonds in some axes, paired with weak vdW forces along other axes. Not only do these materials host remarkable anisotropy, but they are also of great interest in many areas of nano-science due to the unique material properties as 2D materials, and for the ability to exfoliate high-quality, clean, stackable materials that can be arbitrarily placed onto many substrates or devices.

In the study of polaritons in vdW materials, hexagonal boron nitride (hBN) was the first material shown to exhibit naturally hyperbolic polaritons[45,46] (HPhPs) – where the huge structural anisotropy results in non-overlapping optic phonons along different axes (Fig. 2.1d), which causes the permittivity to be opposite in sign along different axes. This results in a significant divergence in the polaritonic behavior – resulting in a polaritonic dispersion with multiple higher-order branches (Fig. 2.1e). Previous works had shown hyperbolic polaritons in metal-dielectric stacks[48,49], but these involved significant sample preparation and suffered from the high loss of metal plasmons.

The term “hyperbolic” arises from the isofrequency contour of the material. In isotropic materials, polaritons are limited to the interface of the material and have an elliptical

isofrequency contour (Figure 2.1a) meaning the supported polariton has a fixed wavevector but can propagate at arbitrary angles. For hyperbolic materials, the opposite in sign permittivity in

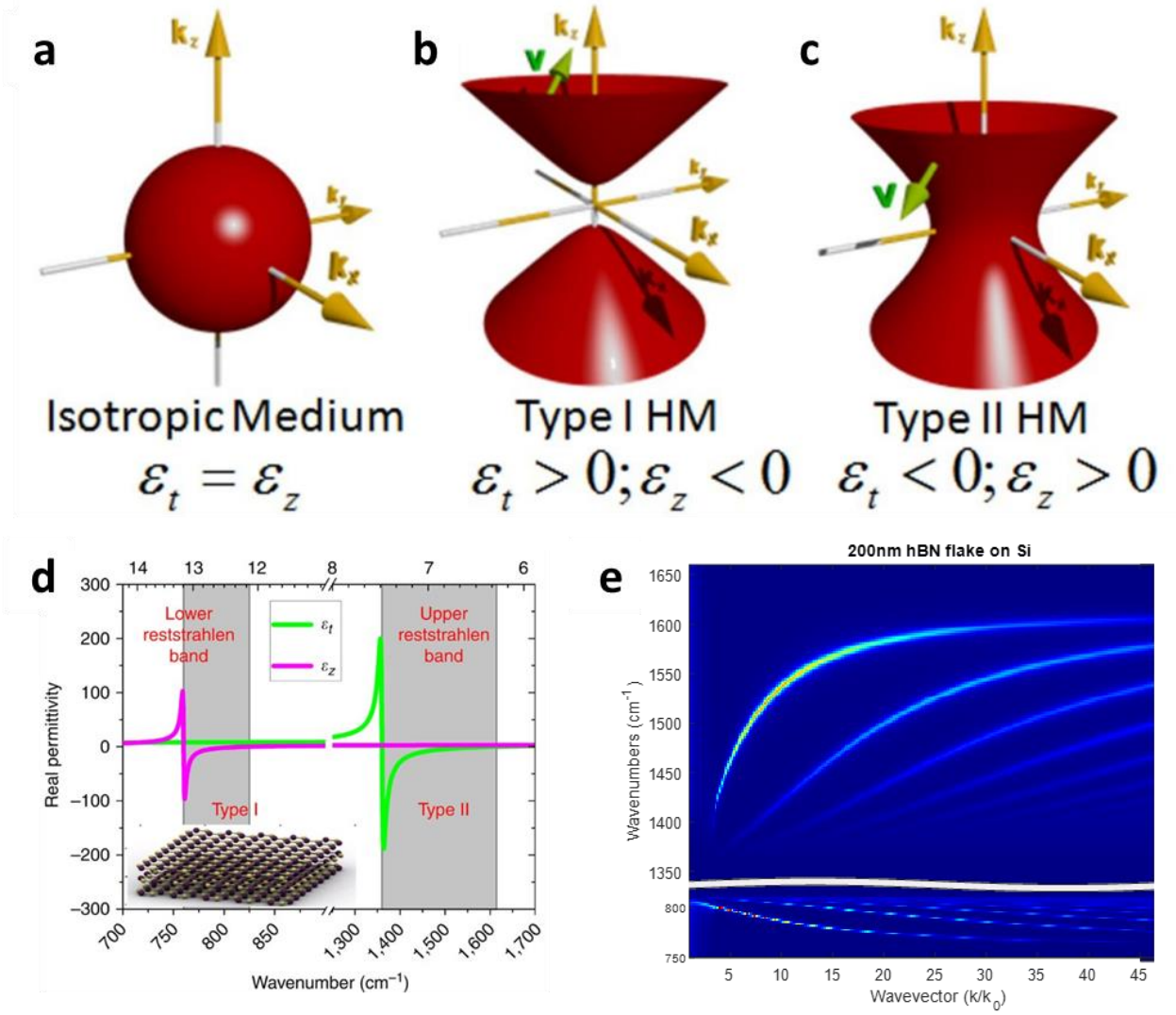

Figure 2.1 *Hyperbolic polaritons and hexagonal Boron Nitride. Isofrequency contours for polaritons in a) isotropic, b) Type I hyperbolic, and c) Type II hyperbolic media. The green arrow tangential to the surface represents the group velocity vector. d) Real parts of the permittivity tensor components of hBN. The Type I lower and II upper Reststrahlen bands are shaded. A schematic of the hBN crystal structure is presented in the inset. e) Polariton dispersion calculated in transfer matrix for a 200nm thick flake of hBN on silicon. Color scale is the imaginary component of the p-polarized reflection coefficient. [a-d from ref.* [45]*]*

different axes causes the isofrequency curve to resemble a hyperboloid[45] (Figure 2.1b,c) so that HPhPs can support arbitrarily large wavevector, but propagate at a fixed angle. In hBN, this

causes the polariton to propagate into the volume of the material at an angle dependent on the permittivity of the material, approximated in Equation 1, where ε_z and ε_t are the out-of-plane and in-plane permittivities, respectively[50].

$$\theta = \frac{\pi}{2} - \arctan\left(\sqrt{\varepsilon_z(\omega)}/i\sqrt{\varepsilon_t(\omega)}\right) \tag{2.1}$$

The stronger confinement, enhanced control over the directional propagation, and volume confinement of hyperbolic polaritons, coupled with the lower losses of phonon polaritons make HPhPs an exciting candidate for infrared nanophotonics. In particular, the high energy, low-loss optic phonons in hBN, and the flexibility of vdW materials have made hBN a prototypical material for nanophotonic devices exploiting hyperbolic phonon polaritons. In this chapter, we detail our contributions to better understanding and exploiting HPhPs in hBN.

2.2 Reconfigurable Infrared Hyperbolic Metasurfaces using Phase-Change Materials

Manipulating optical near- and far- fields can be achieved by scattering light into the resonant modes of nano-structured materials, which collectively form optical metasurfaces[11,51,52]. Historically, metallic polaritonic elements[53] have been used, which are highly absorbing[54], and typically exhibit limited tuning due to the geometric dependence of optical resonances. True reconfigurability (complete changing of the optical response) therefore becomes challenging, as it requires arbitrarily changing the shape of individual elements of the structure, the local dielectric environment, or the optical properties of the polaritonic material itself.

In this regard, phase change materials (PCMs) offer an appealing approach to introducing true reconfigurability as they undergo significant changes in optical properties upon exposure to external stimuli. Examples of PCM's are vanadium dioxide (VO_2), and germanium antimony

telluride (GeSbTe) glasses, which undergo a dielectric to metallic phase transition upon heating or pulsed-laser excitation. For VO_2 this is a volatile (non-latching) phase transition, whereas GeSbTe undergoes a non-volatile (latching) transition. By integrating PCMs and polaritonic materials, changes in optical properties induced by such a phase transition can provide the means to control the polariton dispersion by changing the local dielectric environment in which the evanescent polaritonic near-fields propagate, thus they can be exploited to realize reconfigurable metasurfaces[55–60]. However, one of the phases of PCMs is typically metallic and/or exhibits high optical losses. Consequently, in previous studies of surface-confined polaritons, such as surface plasmon (SPPs) or surface phonon polaritons (SPhPs), the propagation was restricted to spatial regions over the PCM where a low-loss dielectric phase was present[55,56]. This makes concepts such as nanophotonic waveguides, grating couplers and focusing elements extremely difficult to realize in PCM-surface-polariton-based systems, despite the opportunities available.

Here we exploit two key changes in approach that overcome these previous limitations. First, we significantly reduce losses in polariton propagation by using isotopically enriched hexagonal boron nitride[61,62](hBN), a natural hyperbolic[45,63,64] medium that supports low-loss hyperbolic phonon polaritons (HPhPs). Secondly, by implementing hyperbolic polaritons instead of the surface-confined variety[55–60], the polaritons remain sensitive to local changes in the dielectric function of the ambient environment[65], but the electromagnetic near-fields are strongly confined to the volume of the hyperbolic material[45,63,64]. This means that HPhPs interact with spatially localized phase transitions of a PCM, yet do not suffer significant optical losses from this interaction, and thus can be supported over both metallic and dielectric phases.

Vanadium dioxide (VO_2) single crystals were grown by physical vapor transport in a quartz tube furnace at 810°C under 1.7 Torr Ar gas at a flow rate of 25 sccm. Vanadium pentoxide (V_2O_5)

powder (~0.3g, Sigma Aldrich 221899) was placed in a quartz boat (10 x 1 x 1 cm) upstream of the desired substrates and heated for 1 hr. Evaporated V_2O_5 was reduced to VO_2 in this process and deposited on quartz (0001) substrates. Representative crystals from each sample were investigated using Raman spectroscopy to identify the VO_2 phase and optical microscopy to verify the thermal phase transition. Smaller, loose crystals located on the substrate surface were removed by adhesion to a heated (60°C) layer of PMMA firmly brought into contact with the sample and subsequently retracted.

The isotopically enriched hBN crystals were grown from high-purity elemental ^{10}B (99.22 at%) powder by using the metal-flux method. A Ni-Cr-B powder mixture at respective 48 wt%, 48 wt%, and 4 wt% was loaded into an alumina crucible and placed in a single-zone furnace. The furnace was evacuated and then filled with N_2 and forming gas (5% hydrogen in balance argon) to a constant pressure of 850 Torr. During the reaction process, the N_2 and forming gases continuously flowed through the system with rates of 125 sccm and 25 sccm, respectively. All the nitrogen in the hBN crystal originated from the flowing N_2 gas. The forming gas was used to minimize oxygen and carbon impurities in the hBN crystal. After a dwell time of 24 hours at 1550 °C, the hBN crystals were precipitated onto the metal surface by cooling at a rate of 1 °C /h to 1500 °C, and then the system was quickly quenched to room temperature. Bulk crystals were exfoliated from the metal surface using thermal release tape. Crystals were subsequently mechanically exfoliated onto a PMMA/PMGI polymer bilayer on silicon. Flakes were then transferred from the polymer substrate onto VO_2 single crystals using a semi-dry technique, and the polymer membrane was removed using acetone and isopropyl alcohol.

We then perform near-field nano-imaging experiments were carried out in a commercial (www.neaspec.com) s-SNOM based around a tapping-mode AFM. A metal-coated Si-tip of apex

radius $R \approx 20$ nm that oscillates at a frequency of $\Omega \approx 280$ kHz and tapping amplitude of about 100 nm is illuminated by monochromatic quantum cascade laser (QCL) laser beam at different wavelengths and at an angle 45^o to the sample surface. Scattered light launches hBN HPhPs in the device, and the tip then re-scatters light for detection in the far-field (Fig. 2.2a). Background signals are efficiently suppressed by demodulating the detector signal at the second harmonic of the tip oscillation frequency and employing pseudo-heterodyne interferometric detection.

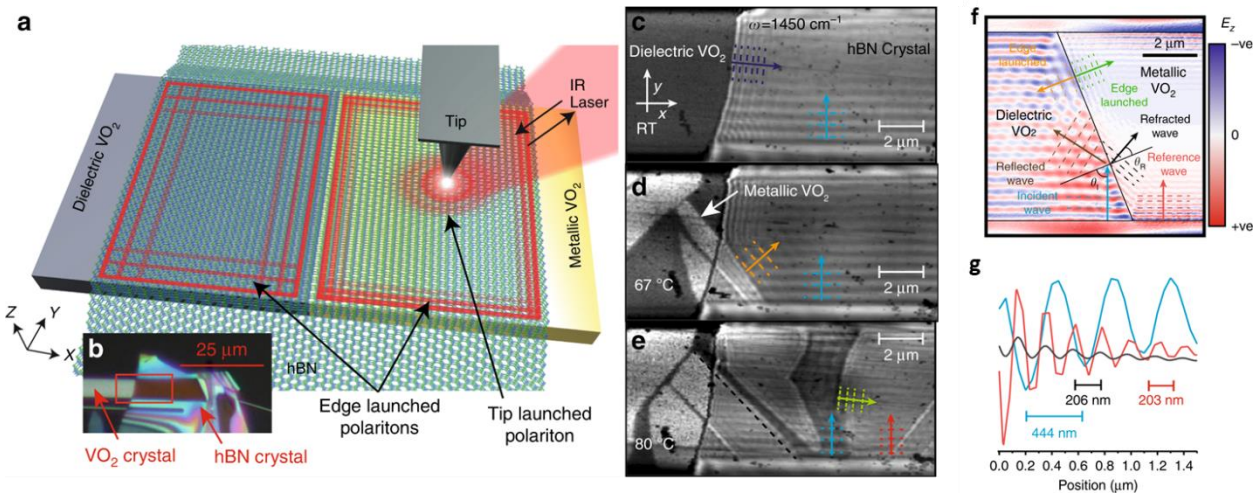

Figure 2.2 *Actively reconfigurable hyperbolic metasurface device. a) A device and experimental schematic, in which hBN has been transferred on top of a VO_2 single crystal and polaritons are imaged by the s-SNOM tip. b) An optical microscope image of the heterostructure. c–e) s-SNOM images of the optical near-field at 1450 cm^{-1} (6.9 μm) at various temperatures, showing HPhPs propagating over both metallic and dielectric VO_2 domains. The complex patterns that form are the consequence of multiple interfering waves over the different domains. The different colored arrows indicate the polariton propagating in different media (Purple – launched by hBN edge, Blue – launched from edge of VO_2 crystal, Orange (Green) – launching from VO_2 phase boundary into dielectric (metallic) phase VO_2). f) An electromagnetic-field simulation of the refraction across a VO_2 phase boundary. g) Line profiles from f showing the refraction of the wave. [from ref.*[66]*]*

The difference in the local dielectric environment between the metallic and dielectric domains results in a large change in the HPhP wavelength in the hBN over each domain (Fig. 2.2c-e), which in turn results in the refraction of the mode when transmitting across the PCM phase

domain boundaries. If a hyperbolic polariton traverses the boundary between different VO_2 domains, the angle of propagation changes to conserve momentum in accordance with Snell's law[67]:

$$\frac{\sin(\theta_I)}{\sin(\theta_R)} = \frac{n_2}{n_1} \tag{2.2}$$

where n_1 and n_2 are the wave-effective indices in the first and second media, and θ_I and θ_R are the corresponding angles of incidence and refraction. To demonstrate that the experimentally measured images are due to refraction, we compare the results in Fig. 2.2d to a simplified electromagnetic simulation (Fig. 2.2f). In the simulation we excite the structure with plane waves (45° incidence), and at the edges of the VO_2 crystal polaritonic waves are launched that propagate across the surface (mimicking edge-launched polaritons). Note that we do not consider the tip-sample interaction in these simulations. Here HPhPs excited at the edge of the VO_2 crystal (blue) propagate in the *y*-direction within the dielectric phase. When these HPhPs approach the angled dielectric-metallic domain boundary (black line), some of the wave will be reflected (brown) and some will be transmitted across the boundary (black) and refracted due to the mismatch in wavevectors for the HPhPs supported over the two PCM domains. The simulation also shows waves launched directly from the domain boundary (orange and green) in Figs. 2.2c and d.

Here, we are verifying the refraction by extracting the polariton wavelengths from linecuts of the polariton fringes from the s-SNOM experiments and the simulations (Fig. 2.2g), which agree well with Eq. 2.2, confirming the polariton refraction across VO_2 boundaries. This means that the combination of hyperbolic media and PCMs employed here can be used to create refractive optical elements and waveguides[68], as well as components benefitting from full optical

functionalities that to this point have been limited to far-field optics.

This combination of PCMs with hyperbolic media opens a whole new toolset for near-field optical design and structuring. Significantly, for reversible PCM transitions, any of these designs can be fully reconfigured using either thermal or laser-writing based approaches. Finally, by exploiting the increasingly wide range of different PCMs and hyperbolic materials and metamaterials (such as transition metal oxides[69]), these effects can be realized over an extended range of frequencies and patterning methods.

2.3 HPhP Design and Modulation in vdW / Doped Semiconductor Heterostructures

Hyperbolic phonon polaritons (HPhPs) can be supported in highly anisotropic materials, where the real parts of their permittivities along different directions are opposite in sign as a result of spectrally offset optical phonons. Compared to surface polaritons, HPhPs offer further confinement of long-wavelength light to deeply subdiffractional scales, and volume propagation that enables control of the polariton wavevector by changing the underlying medium. This allows for greater control of polaritonic resonators and near-field polariton propagation. Yet, to realize the full potential of HPhPs for infrared nanophotonics, it is necessary to demonstrate engineered HPhPs on broadly tunable, low surface roughness substrates. We here demonstrate that doped semiconductors, e.g., InAs and CdO, can meet these needs and thus to be used to engineer HPhPs with almost arbitrary and continuous tuning of the HPhP wavevectors. We elucidate HPhP characteristics as a function of the plasma frequency of an InAs substrate, which features a significant wavevector discontinuity and modal order transition when the substrate permittivity crosses zero in the Reststrahlen band. Around the transitional point, the HPhP system is sensitive to perturbations, e.g., the working frequency and InAs plasma frequency, thus it is suitable for

sensing and modulation applications. We also illustrate that the hBN/InAs platform allows for active modulation at sub-picosecond time scales by photo-injecting carriers into the InAs substrate, demonstrating a wavevector change of ~1.6x. Overall, the demonstrated hBN/doped semiconductor platform offers significant improvements towards manipulating HPhPs, and enormous potential for engineered and modulated polaritonic systems for applications in on-chip photonics and planar metasurface optics.

2.3.1 Substrate Engineering of HPhPs

Due to the long free-space wavelength of mid- to far-infrared (IR) light, the realization of deeply subdiffractional photon confinement via the stimulation of polaritons[26] is critical for flat IR nanophotonic applications, such as miniaturized optical components[70–72], on-chip photonics[73], polariton waveguides[66] and nanolasers[74]. More specifically, hyperbolic polaritons supported by extremely anisotropic media, i.e., those featuring permittivity tensor components with oppositely signs along different optical axes, can offer significant promise for many nanophotonic applications[75] where stronger confinement, and improved control over propagation is beneficial. Applications of these properties include hyperlensing[50,76–78], metasurface-based optical components,[79,80] quantum optics[81] and probes of nanoscale defects[82,83]. While hyperbolicity was first demonstrated with artificial dielectric/metal stacks[76], it was later discovered that a list of natural materials[26,84], including hBN[45,64], MoO_3[43,69], V_2O_5[85] support hyperbolic phonon polaritons (HPhPs). These opportunities are further expanded within low symmetry systems as demonstrated by the report of so-called ‘Ghost-polaritons’ in off-cuts of calcite[44] and hyperbolic shear polaritons in monoclinic such as β-Ga_2O_3[29]. Such HPhPs in nature crystals feature exceptionally low optical loss[32,46,86], because polaritons are derived from optic phonons[32,87] instead of scattering from free carriers[12,32,88].

Unlike surface-confined polaritons[56], volume-confined HPhPs can interact with the local environment with minimal optical loss[66]. Based on this principle, it has been demonstrated that HPhP wavevectors can be tuned and engineered by changing the substrate permittivity in a list of studies[66,89–93], with this effect having been generalized by Fali et al[89]. Additionally, HPhPs propagating across domains with varying permittivities will be refracted, with the behavior described by Snell's law[89] and the continuity of tangential components of the wavevectors. With those fundamentals, patterned substrates can be used to manipulate polaritons supported by pristine hyperbolic media, such as polaritonic refraction[80,89,94] (e.g., prism and lensing), structured HPhPs[66,80,95] (e.g., waveguiding), photonic crystals[96] and accelerated HPhPs[97]. Like dielectric optics, those effects rely on wavevector differences for the HPhPs over different substrate regions, and some results can be enhanced with more significant contrast[97]. Additionally, the platform is ideally flat, as placing thin vdW materials over uneven surfaces (e.g., silicon pillars) will modify the morphology and/or induce strain[98,99] and scattering[100]. However, all existing demonstrations have either used 3D structures to induce a large contrast in the wavevectors, e.g., silicon versus air (etched silicon[95]), or provided fundamentally limited polaritonic wavevector change (~1.6 times for phase change materials[66,80]). Therefore, it is ideal to find a platform that provides a planar surface and sufficient wavevector contrast that can be actively controlled.

To this end, we demonstrate a hyperbolic material/doped semiconductor platform to control HPhPs at an unprecedented level with ultralow surface roughness (sub-nanometer). In a lossless case, such platforms would enable arbitrary manipulation of HPhP wavevectors. Moreover, we illustrate a sharp modal order transition when the plasma frequency of the doped semiconductor passes through the transitional frequency, manifesting a wavevector discontinuity suitable for

modulation and sensing applications. Around the transitional point, we experimentally demonstrate a wavevector difference of ~9.6 times for hBN over different InAs substrates. Finally, we show that the hBN/doped semiconductor system can be modulated at sub-picosecond time scales by photo-injection, with an experimentally demonstrated polaritonic wavelength change of ~1.6 times. Although we focus primarily on uniformly doped semiconductors, we stress that semiconductors with in-plane varying plasma frequency can also be realized, offering significant freedom to manipulate HPhPs along a planar surface. Importantly, the application of the platform is not limited to hBN, as plasma frequencies of doped semiconductors can be tuned over an extended range of frequencies for other hyperbolic materials (e.g., MoO_3), providing a significant toolbox for manipulating HPhPs.

2.3.2 Concept of tuning HPhPs via substrate permittivity

Although HPhPs are volume-confined modes, they remain sensitive to the local environment[66,89–93,101], e.g., the dielectric function of the substrate. The dependence of HPhP wavevectors (k_{HPhP}) over substrate permittivity can be described by an analytical solution19:

$$k(\omega) = k' + ik'' = -\frac{\psi}{d}\left[\operatorname{atan}\left(\frac{\varepsilon_o}{\varepsilon_t \psi}\right) + \operatorname{atan}\left(\frac{\varepsilon_s}{\varepsilon_t \psi}\right) + \pi l\right], \quad \psi = -i\sqrt{\frac{\varepsilon_z}{\varepsilon_t}} \qquad (2.3)$$

where d represents the hBN thickness, ε_o and ε_s the complex dielectric functions of air and the substrate, respectively, ε_t and ε_z are dielectric functions of hBN along in and out of plane axis, while l represents the HPhP mode order (0,1,2…).For a hBN/doped semiconductor heterostructure, the HPhPs supported can be indirectly engineered by changing the carrier concentration (therefore the plasma frequency, ω_p, and dielectric function) of the doped semiconductors, even with uniform hBN thickness. Therefore, HPhPs propagating in different domains possess different wavevectors, as shown in the schematic Fig. 2.3a. This difference can

be used to engineer HPhPs for far-field resonators[89] or the near-field polariton propagation[66,80,94–97]while minimizing fabrication-induced optical loss.

We first exemplify the substrate-induced polariton tuning with a hBN/InAs heterostructure. To this end, we grew InAs samples with different ω_p by controlling the as-grown dopant

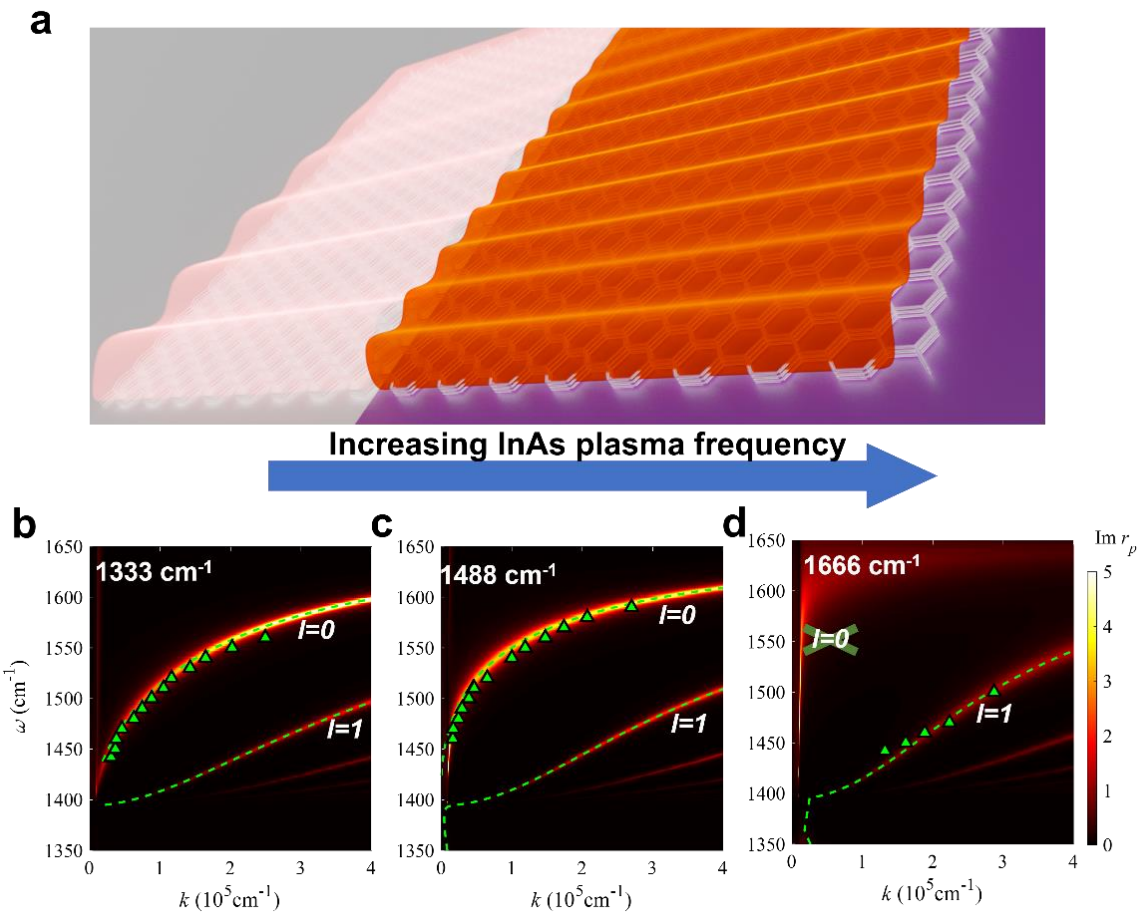

Figure 2.3 *Tuned HPhP dispersion of hBN/doped semiconductor heterostructure by controlling semiconductor ωp. (a) Schematic of the platform. For the same hBN, the HPhP wavelength changes as a function of the plasma frequency of semiconductor. In this example, the right side (magenta color) is highly doped, shrinking the polariton wavelength. (b-d) Dispersion plots of hBN over InAs of different plasma frequencies. The plasma frequencies are noted on the corresponding panels, and the thicknesses of hBN are 51, 51 and 55 nm, respectively. The contour plots and dashed curves are calculated by transfer matrix method (TMM) and Eq. (2.3), respectively, and the triangles are extracted from s-SNOM data.*

concentration and transferred hBN slabs onto these InAs substrates. We then utilized scattering-type scanning near field microscopy (s-SNOM) to measure the HPhP dispersions through Fourier analysis of linescans from the flake edge. To minimize the role that the hBN thickness plays in dictating HPhPs wavevectors, similar hBN thicknesses (~51-55 nm) are used in this set of comparisons. The calculated dispersion plots along with the experimentally extracted data points validate that HPhP dispersions can be manipulated by varying the InAs ω_p (Fig. 2.3b-d).

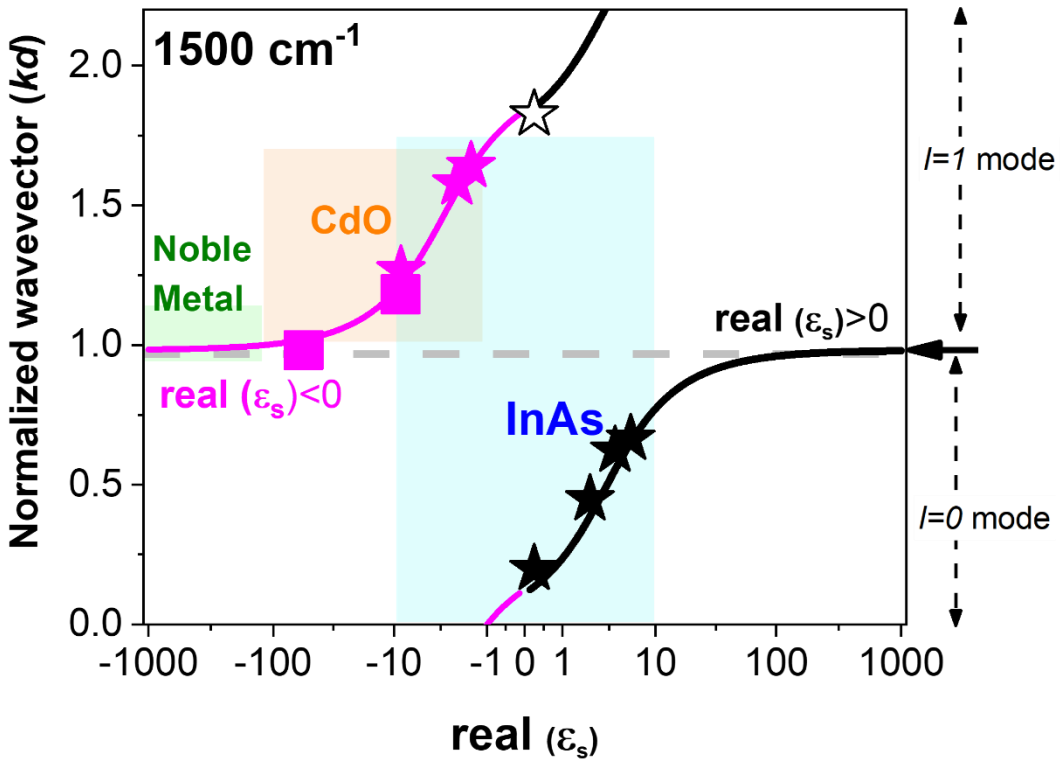

Figure 2.4 *Full control of kHPhP with doped semiconductors. The normalized kHPhP varies with the |Re(εs)| of the substrate. All curves are calculated by Eq. (2.3), while all symbols are experimental data. Colored shadows indicate the tunable range of kHPhP with that substrate with achievable doping. Solid symbols represent fundamental modes, while open symbols represent high-order modes. Data with dielectric (metallic) InAs are plotted with black (purple) symbols. Data with metallic CdO are plotted with purple rectangles. Note that all noble metals actually lead to nearly identical kHPhP, and the color box on the y-axis is extended for visualization purposes. Due to the accessible carrier concentration and high-frequency permittivity values, the tuning range of |Re(εs)| of InAs and CdO are -10 to 10, and -100 to -2, respectively.*

Notably, the HPhP modal numbers in those systems are different: *l=0* branch is only supported when InAs is dielectric (Fig. 2.3b-c versus Fig. 2.3d), due to the mirror symmetry. We focus on the most dominant HPhP mode in both near- and far-field, i.e., the HPhP mode with lowest wavevector, and we refer them to as fundamental mode following other references[61,64,65].

While HPhPs can be tuned by the substrate ω_p, quantitative analyses of the dependence of the k_{HPhP} over upon the substrate property permittivity are required to use this concept for engineered devices. By nature, the HPhP dispersion varies proportionally with the sample thickness - but most applications (such as polariton refraction) are robust to sample thickness. In order to compare multiple samples of varying thickness, we normalize the polariton dispersion by multiplying the wavevector by the hBN thickness, i.e., $k(\omega)d$. The normalized wavevector at a given frequency is then only related to substrate permittivity (ε_s) and mode order (l), and it is found to be highly sensitive to substrate permittivity, as shown in Fig. 2.4. Most notably, *l=0* branch is only supported for dielectric substrate, and it is forbidden with metallic substrate due to mirror symmetry[90]. Therefore, when we focus on the fundamental mode, the modal orders are different: *l=0* (low confinement) and *l=1* branch (high confinement) for dielectric and metallic substrates, respectively. Furthermore, the wavevectors can also be manipulated by the substrate permittivity even within the same modal branch: increasing $\mathrm{Re}(\varepsilon_s)$ leads to reduced k_{HPhP}. It is important to note that the majority of k_{HPhP} values are realized within a small range of $\mathrm{Re}(\varepsilon_s)$ (between -10 and 10), including the highest and lowest k_{HPhP} values, which could induce largest polaritonic refraction effects.

While the tunability of HPhPs via substrate is promising, traditionally used metallic substrates

(noble metals) do not provide access to the high wavevector range, since they exhibit $|\mathrm{Re}(\varepsilon_s)|$ over 100 in the mid-infrared. To address this challenge and maximize the ability to manipulate HPhP wavevectors, we here use doped semiconductors with designable plasma frequency to access those ranges. Specifically, InAs and cadmium oxide (CdO) are two promising candidate materials, with achievable plasma frequencies from 500-2500 cm^{-1} and 1500-15000 cm^{-1}, respectively. Experimentally, we grew InAs and CdO substrates with varying ω_p, and $h^{10}BN$ flakes were transferred onto them, with k_{HPhP} measured and extracted by Fourier analysis. The experimental data plotted as symbols in Fig. 2.4, showing excellent agreement. Notably, we experimentally obtained both the highest and lowest k_{HPhP} at 1500 cm^{-1} with InAs substrates, which could be used to exploit polaritonic in-plane refractive behavior.

With doped CdO and InAs, we almost entirely unlock the potential of controlling the k_{HPhP} with this tuning of the substrate permittivity, and only a tiny range of k_{HPhP} are not accessible (~10%), where high refractive index dielectrics would be required. Unlike noble metals that typically feature high surface roughness[102] without specialized growth[102] and/or fabrication[100,103–105], these doped semiconductors possess as-grown low surface roughness (below 1 nm), which is another crucial criterion for HPhP platforms[100,102]. Therefore, those doped semiconductors can serve as ultrasmooth platforms to enable the tuning of HPhPs over an extensive range of k_{HPhP}.

2.3.3 Modal order transition

While the changed order of the fundamental mode in hBN on dielectric vs metallic substrates contributes provides a means for strong tuning when the substrate permittivity is near zero – by tuning ω_p of the substrate through the reststrahlen band we can take advantage of the modal order transition for a discontinuous transition in the polariton wavevector. To realize this in the doped semiconductor platform - we must develop an understanding of the dependence of the

wavevector on the substrate ω_p. In particular, the hBN/InAs heterostructure offers an ideal tuning range for engineering the HPhPs. To that end, we calculate how k_{HPhP} changes with InAs ω_p, at a working frequency of 1500 cm^{-1}, as shown in Fig. 2.5a. When InAs ω_p passes the working frequency, InAs characteristic changes from dielectric to metallic (grey and magenta shaded in Fig. 2.5a, respectively). This dielectric-metallic evolution of substrate further induces HPhP

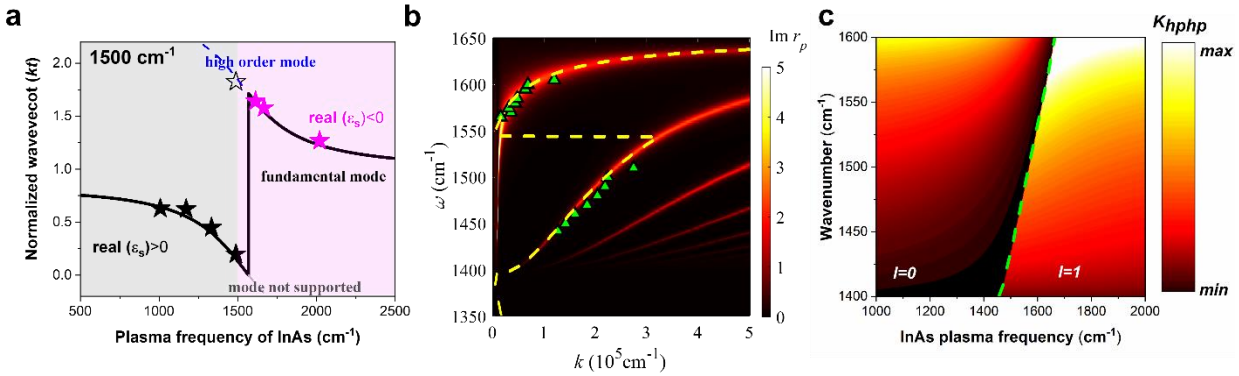

Figure 2.5 *Modal order transition of HPhPs in hBN/InAs heterostructure. (a) The relationship between normalized kHPhPs and InAs ωp. All curves are calculated by Eq. (1), while all symbols are experimental data. Solid symbols represent fundamental modes, while open symbols represent high-order modes. Data with dielectric (metallic) InAs are plotted with black (purple) symbols. The colored shades indicate whether InAs behaves as dielectrics or metal. (b) The modal order transition observed in the frequency domain. The contour plot is calculated by TMM and triangles are experimental data. (c) kHPhPs ¬at different wavenumber and InAs ωp, with larger kHPhPs ¬plotted with larger color. A clear modal order transition is observed when InAs ωp passes the Reststrahlen band of hBN.*

modal order transition from *l=0* to *l=1* branch, leading to the wavevector discontinuity. Additionally, in both dielectric and metallic regimes (grey and magenta shaded in Fig. 2.5a, respectively), increasing InAs ω_p leads to declining $Re(\varepsilon_{InAs})$, which in turn makes k_{HPhP} monotonically decrease. Importantly, both minimum and maximum k_{HPhP} can be found around the transitional point, and we experimentally demonstrate a change in the normalized wavevector of 9.6 times at 1500 cm^{-1}.

The permittivity of InAs is dispersive, so the modal transition can also happen in the frequency domain. When InAs $Re(\varepsilon_s)$ passes through -1 within the Reststrahlen band of hBN, a modal order

transition happens, splitting the fundamental HPhPs into two supported modal orders, as shown in Fig. 2.5b. As such, the dispersion plot features highly confined HPhPs below the transitional frequency (*l=1* mode), while showing low confined HPhPs above it (*l=0* mode) (Fig. 2.5b). Using an InAs sample with a ω_p at a frequency within the Reststrahlen band, we experimentally demonstrated the transition discontinuity (Fig. 2.5b, green triangles), with good agreement with calculations. The dispersion is analogous to two stacked hyperbolic dispersions, and we observed intriguing behaviors in both frequency (coexisting absorption and reflection modes) and real space (guiding in different regions at different frequencies) in numerical simulations.

The modal order transition criteria can be generalized for both the InAs ω_p (substrate-tuning) and working frequency (frequency-tuning) domains, as shown in Fig. 2.5c. A clear transition line distinguishes the two modal orders, separating k_{HPhP} into two regimes: one where highly confined HPhPs are observed (right side) and one where less confined modes are supported (left). At any transition point, the modal order transition could happen if InAs ω_p is changed or the working frequency is changed, i.e., along the InAs ω_p axis or wavenumber axis in Fig. 2.5c, respectively. As a consequence of the modal order transition and wavevector discontinuity, around the transitional line, k_{HPhP} experience large variation with any perturbations of working conditions, e.g., InAs plasma frequency, working frequency, and local environment. Therefore, a HPhP system working around the transitional point, such as resonators, can be modulated effectively and/or used for refractive index sensing. It is important to note that for any working frequency inside the Reststrahlen band of hBN, there is a corresponding InAs ω_p to enable this transition, while such tunability of InAs[106] and CdO[107] lend this concept to be expanded to other hyperbolic materials, e.g., MoO_3.

2.3.4 Ultrafast HPhP Modulation

Besides manipulating HPhPs in static structures, the hBN/doped semiconductor platform also enables the dynamic modulation of HPhPs. Both permittivity tensors of InAs[108] and CdO[109] can be modulated at the surface by photo-carrier injection and/or electrical biasing. Here we demonstrate ultrafast modulation of HPhPs with photo-injection into InAs. When a 130-fs, 80-MHz repetition rate pulsed laser source at 0.78 eV (1590 nm free-space wavelength) irradiates the hBN/InAs heterostructure, the photons will only be absorbed by InAs since it is above InAs bandgap (0.35 eV) yet well below that of hBN (~6 eV)[110]. This process will generate a surplus of free-charge carriers at the InAs surface, locally increasing ω_p with a rise time below 1 ps, and those free carriers will then recombine with a lifetime of ~8 ps, as shown in Fig. 2.6c. As a consequence of this locally modulated InAs ω_p, k_{HPhP} supported by hBN/InAs heterostructure can be modulated at such picosecond time scales.

To experimentally demonstrate such modulations, we conducted a near-field pump-probe measurement on one of the hBN/InAs heterostructures. Before the pump signal arrives (*pre-pump*), we observe a polariton wavelength of ~ 1.1 μm at 1450 cm^{-1} for the HPhPs supported. When the pump arrives (*at-pump*), the InAs ω_p at the surface is shifted to a higher frequency, leading to a decreased k_{HPhP} as mentioned, and we experimentally observe a stretched polariton wavelength (~1.7 μm). Since the time constant of modulated InAs ω_p is ~8 ps, the induced HPhP wavevector is expected to recover within a similar temporal scale. Experimentally, we find the polaritonic behavior quickly changes to a state between *pre-pump* and *at-pump* even after only 1 ps of the pump signal, and the change is insignificant after ~ 7 ps (green curve in Fig. 2.6a).

In addition to the modification of the polariton wavelength, we can also monitor how resonant frequency of a given HPhP system change when the InAs is pumped. For a proof-of-concept demonstration, we measured the nano-FTIR spectra at a spatial position ~0.7 μm from the hBN

edge, which corresponds to a constant wavevector of HPhP system ($k \approx 5\times10^4$ cm^{-1}), and the frequency amplitude peaks indicate the modal frequency. When InAs ω_p is increased, the wavevector at a fixed frequency is reduced; therefore, when we look at a constant wavevector, the corresponding frequency blueshifts. Experimentally, the modal frequency indeed experienced a blue shift when InAs was pumped. This implies that we can modulate HPhP resonators at ultrafast time scales[111] with un-pumped phonon materials for potentially lower loss, and the ultrafast switch of HPhPs has important implications for device applications in modulated optical sources[112], beacons and other areas. Importantly, we do not pump the polaritonic material (unlike reference where polar materials are directly pumped[111]), our approach offers a great degree of flexibility in terms of different doped substrates, as well as other hyperbolic materials, and could provide a foundation for more complex heterostructures.

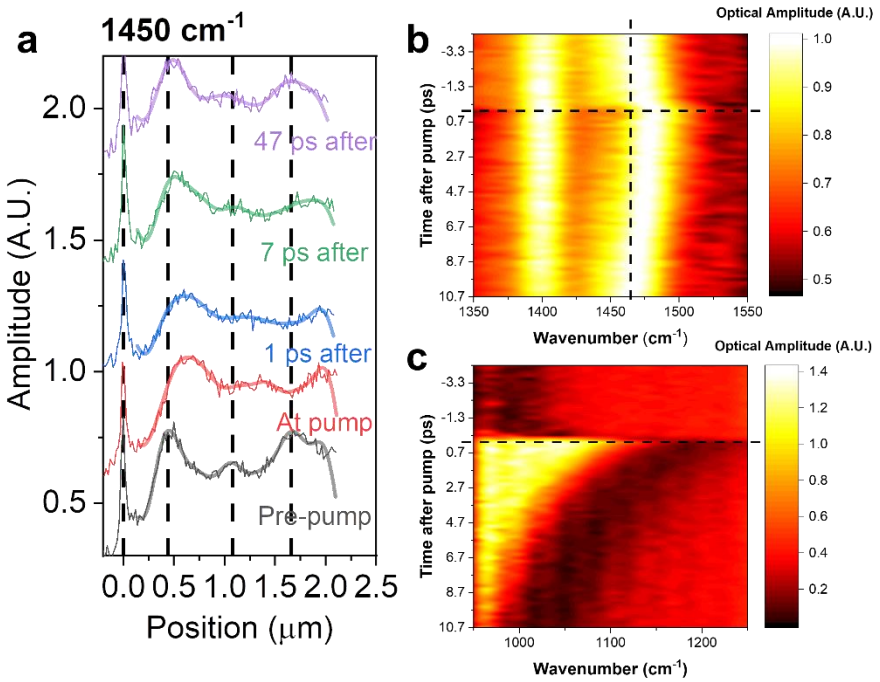

Figure 2.6 *Ultrafast modulation of HPhPs. (a) The line profile extracted from pump-probe nano-FTIR scans at different time delay. The noisy curves are raw data, and we then applied FFT filters to remove the noise and the filtered data are plotted with thick lines over raw data. (b) The ultrafast nano-FTIR probed at a constant spatial position (~ 0.7 μm from the edge, k≈5×104 cm-1). The data here are processed with FFT filters to remove noise, and the raw data and signal process can be found in SI, section 7. (c) The ultrafast nano-FTIR measurements on InAs substrate. The reflection dip position is related to the plasma frequency of InAs. The InAs static plasma frequency is 1050 cm-1, and the hBN thickness is 55 nm.*

2.3.5 Conclusions

In summary, we proposed and demonstrated a hyperbolic material/doped semiconductor platform to manipulate HPhPs at an unprecedented level. Almost arbitrary (~90%) possible HPhP wavevectors can be realized in such a heterostructure, facilitating the manipulation of HPhPs via wavevector contrast. Moreover, when the plasma frequency of the doped semiconductor passes through the polariton frequency, a sharp modal order transition of HPhP will occur, and the HPhP system is highly sensitive to the local environment around the transitional point, which could be used for sensing and modulation purposes. Finally, we demonstrate an ultrafast modulation of HPhPs at picosecond time scales by photoinjecting free

carriers into semiconductors, with a polaritonic wavelength change of ~1.6 times. With the advancements in semiconductor manufacturing, such as further reduced ohmic loss and in-plane varying doping, we expect the doped semiconductor to be an increasingly important platform to manipulate HPhPs, both in the near- and far-field. Importantly, the concept is not limited to hBN, and these effects can be realized over an extended range of frequencies and hyperbolic materials (e.g., MoO_3), opening a whole new toolbox to manipulate in-plane HPhPs.

2.4 Photothermally Probing HPhP Absorption at the Nanoscale

For imaging polaritonic behavior, AFM-based s-SNOM measurements are standard practice. Compared to far-field and nonlinear spectroscopies, the deeply subdiffractional resolution and lax sample restrictions of s-SNOM measurements provide enormous advantages for fundamental understanding of nanophotonic devices. However, it has been suggested that the fundamental mechanism of s-SNOM, which relies on the interference between the electric field scattered by the tip and the field on the surface of the sample is subject to certain optical selection rules that can limit the information provided by s-SNOM.

Instead, a number of AFM-based optical techniques have arisen, which provide the excellent spatial resolution of s-SNOM but rely on alternative mechanisms to probe the polariton behavior. One such technique, the photothermal induced resonance technique (PTIR) is similar to s-SNOM, but rather than measuring the optical field interfering with the tip, PTIR uses the AFM deflection to measure the local thermal expansion due from pulsed laser absorption[113,114]. This technique is limited to materials where the excitation generates significant thermal expansion, and has previously been employed for mapping of electronic bandgap[115] and chemical composition[116] at the nanoscale, with applications in biology[117,118], photovoltaics[119],

polymer science[120,121], pharmaceutics[122], and plasmonics[123–125], as reviewed elsewhere[114,126]. Here, we use this technique to gain new understanding of the volume-confined HPhPs in resonators and flakes of hBN.

2.4.1 Mapping and Spectroscopy of Non-Radiative Hyperbolic Modes

Surface phonon polaritons[32,127,128], are a low-loss alternative to surface plasmons that enable exciting applications at infrared and terahertz frequencies[32], including narrow-band thermal emission[127,129,130] and yield high quality factors (>300) nanoscale antennas[45,131–134] and unprecedented modal confinements[32,131,132]. These characteristics result in very large Purcell factors that are necessary to achieve strongly enhanced optical processes at the nanoscale, e.g. second harmonic generation in SiC nanopillar arrays[135]. Hexagonal boron nitride (hBN) has recently attracted much interest because of its intrinsic hyperbolicity[45,64] and the potential for integration with graphene and other van der Waals materials[136–138] to realize novel hybrid architectures[139,140]. Hyperbolicity is an extreme form of optical anisotropy, in which the values of the real part of the dielectric function along orthogonal crystalline axes are not only different, but in fact opposite in sign. This property enables polaritonic modes with very large wavevectors (i.e., confinement to very small dimensions)[63] and restricts the polariton propagation along directions dictated by the material dielectric function[78,141–143] Hexagonal boron nitride is considered the archetype of an ever-broadening library of naturally hyperbolic materials[84,144,145] and provides an ideal platform for studying hyperbolic phonon-polaritons (HPhPs) [45,61,64,137,141,146,147] - deeply sub-diffraction, volume-confined collective optical modes - that enable unique applications in mid-infrared nanophotonics[78,143].

In contrast to conventional metals and polar insulators, where polaritons are confined to the material surface, hyperbolic phonon polaritons can freely propagate in a nanostructure volume

and must be characterized by three distinct quantum numbers (instead of two for surface polaritons). The choice and physical meaning of these numbers (or modal indices) is geometry-specific. For example, thin hBN slabs are characterized by the in-plane momentum vector $\vec{q} = (q_x, q_y)$, which is a continuous variable, and one branch of index $l = 0, 1, ...$, a discrete number[45,64,148]. For nanostructures that confine polaritons in three dimensions[45,141,148], all their modal indices must be discrete. For example, the modes of ideal spheroidal nanoparticles are characterized by the azimuthal angular momentum m, the orbital angular momentum l, and a radial index n. Far-field spectroscopic experiments on three-dimensionally confined truncated nanocones, the so-called 'frustum' shaped nanostructures[45,141] have detected a few low-order HPhP resonances ($l \leq 7, m = 1, n = 0; l \leq 3, m = 0, n = 0$) in two distinct spectral bands. These resonances are qualitatively described by the calculations for ideal spheroidal particles when parametrized with respect to the frustum aspect ratio

$$A_r = d/t\,, \tag{2.4}$$

where d is the average diameter at half-height and t is the film thickness.

The higher-l modes have many desirable properties. They are characterized by a shorter polariton wavelength $\lambda_p = 2\pi/q$ and hence, by a stronger field confinement that can be exploited for sub-diffraction imaging and focusing. Although many other higher-order HPhP modes (with $m > 1$ and $n > 0$) have been theoretically predicted[148], they remained elusive because coupling to far-field radiation is either very weak or forbidden by selection rules. These high-order HPhP modes offer more precise tailoring of the evanescent near-field spatial distributions and better matching of the polariton orbital angular momenta to those of nanoscale absorbers or emitters, potentially modifying the selection rules to make weak or forbidden transitions dominant[149,150].

Scattering-type scanning-near-field optical microscopy (s-SNOM) utilizes a sharp, metallized tip as a scanning optical antenna that can aid the excitation of such modes in the near-field and has enabled imaging high-l modes in hBN slabs in real space. Here, we show that another near-field technique, photothermal induced resonance (PTIR) enables direct observation of multiple 'limbs' ($m = 0,\ \ n > 0, l = 1,2,3, ...$) of the hBN hyperbolic dispersion relation in hBN frustum nanostructures. These measurements give the first unequivocal evidence for the existence of the 'dark' higher order modes[148]. In previous far-field and s-SNOM measurements only the ($l = 1,2,3, ...$) 'branches' of the $m = 1$, $n = 0$ limb were detected. PTIR makes the observation of the higher order modes possible because it detects light absorption by mechanically transducing the sample photothermal expansion, thus bypassing the challenge imposed by weak far-field emission that limits established methods. Consequently, these results highlight the PTIR capability to characterize nanophotonic dark-modes of both artificial meta[48,63,75,150–152] and natural[45,64,84,144] hyperbolic media.

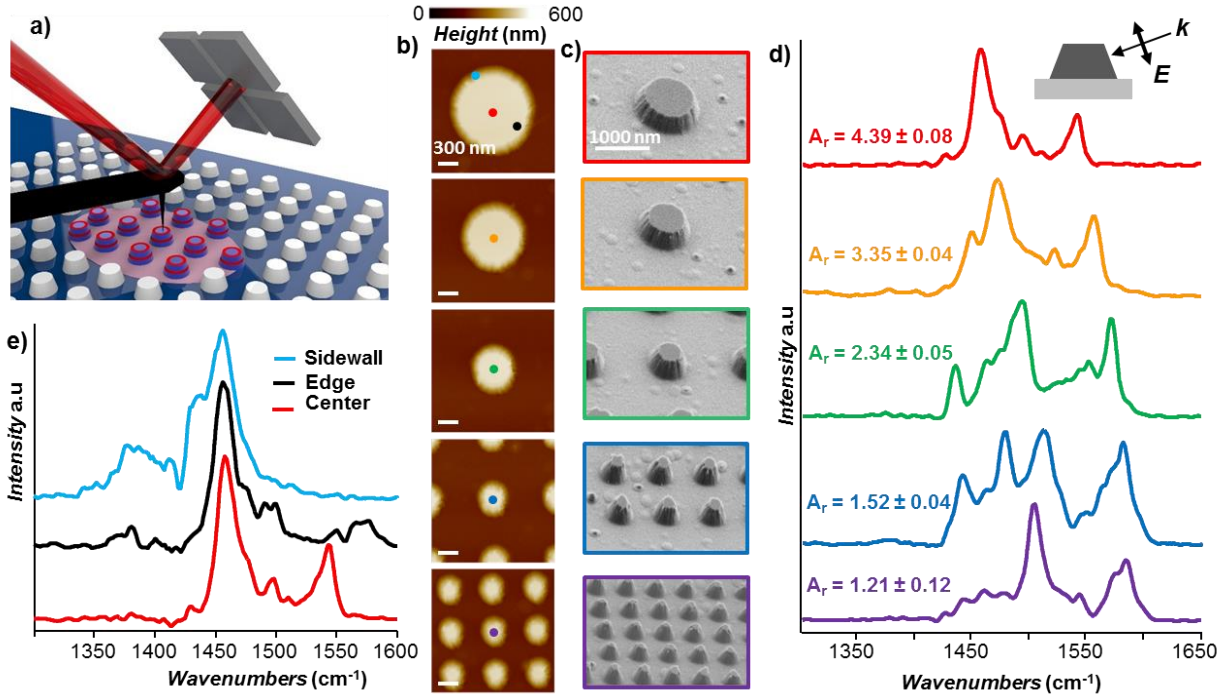

Figure 2.7 *a) Schematic of the PTIR experiment. A pulsed tunable IR laser illuminates the portion of the sample (region highlighted in pink centered around gold-coated AFM probe operating in contact mode). b) AFM topography (scale bars 300 nm) and c) corresponding tilted SEM images (scale bars 1.0 µm) of five representative frustums with different aspect ratio. All the frustums have a thickness of 256 nm ± 4 nm. d) PTIR absorption spectra (p-polarization) obtained by positioning the AFM tip at the center of representative frustums, as indicated in panel b. The schematic of the incident polarization used for the measurements is provided as an inset. e) Color coded position dependent PTIR absorption spectra for the A_r = 4.39 frustum. The spectra in panel d and e are displayed with an offset for clarity.*

The PTIR combines the spatial resolution of atomic force microscopy (AFM) with the specificity of absorption spectroscopy. Because PTIR often utilizes infrared (IR) excitation, it is also known as AFM-IR. Similar to s-SNOM, in PTIR a metallized AFM tip is used to overcome the momentum mismatch and/or enhance coupling between the far-field radiation and the deeply sub-diffraction polaritonic modes. In contrast to s-SNOM, where the tip is operated in tapping mode and the scattered light is detected, in the PTIR experiments presented here, the AFM probe is in contact with the sample (contact mode) and acts as a near-field mechanical detector. A detailed comparison between the working principles of PTIR and s-SNOM and corresponding applications is available elsewhere[114]. The PTIR signal transduction typically follows the

sequence: optical energy into vibrational energy (absorption), absorbed energy into heat, heat into mechanical thermal expansion, thermal expansion into cantilever motion, and cantilever motion into AFM photodetector signal[115]. Although novel nanoscale probes with integrated cavity opto-mechanics [153], can track the fast sample thermal expansion dynamics, the conventional cantilevers used here are too slow to capture that process and are kicked into oscillation by the sample expansion similar to a struck tuning fork. Because the amplitude of the PTIR signal (cantilever oscillation) is proportional to the energy absorbed by the sample[123,154], PTIR spectra enable mapping of electronic bandgap[115] and chemical composition[116] at the nanoscale, with applications in biology[117,118], photovoltaics[119], polymer science[120,121], pharmaceutics[122], and plasmonics[123–125], as reviewed elsewhere[114,126]. For example, PTIR recently enabled the observation of 'dark' modes in plasmonic antennas[123,155] and the imaging of HPhPs modes in micrometer-sized hBN flakes[90].

The PTIR set up used in this work consists of a wavelength-tunable, pulsed laser that illuminates a portion of the sample (≈ 50 μm diameter centered around the AFM probe) with an angle of ≈ 20° with respect to the sample surface (Fig. 2.7a). The gold-coated Si AFM probe provides the momentum-matching necessary for efficiently coupling the incident light into the highly confined, large-wavevector polaritonic modes. Five periodic arrays of hBN frustum-shaped nanostructures with d ranging from 312 nm ± 26 nm to 1120 nm ± 22 nm (as measured by AFM; Fig. 2.7b), similar to those previously measured by far-field reflectance/transmittance[45] and s-SNOM[141], are studied here. The uncertainties in the nanostructure dimensions represent one standard deviation in the measurements of seven nominally identical structures. The nanostructures have a thickness of t = 256 nm ± 4 nm and are characterized by A_r ranging from 1.21 ± 0.12 to 4.39 ± 0.08, where the A_r uncertainty is determined by the uncertainty in the

measurement of the frustum diameters. The corresponding scanning electron microscope (SEM) images are provided in Fig. 2.7c, with details on the sample fabrication available elsewhere[45,141]. The hBN HPhP modes were observed within the hBN upper Reststrahlen band[45,64] (1360-1610 cm^{-1}). Local PTIR absorption spectra (Fig. 2.7d,e) were obtained for each cone by placing the AFM tip in specific locations on the frustums and plotting the amplitude of the cantilever-induced oscillations as a function of laser frequency. In addition, PTIR absorption maps were obtained by scanning the AFM tip while illuminating the sample at a given incident frequency and measuring the amplitude of the cantilever-induced oscillation as a function of tip location. PTIR experiments can be obtained with either *s*- (in plane) or *p*-polarized light. Because of the incident light angle, illumination with *p*-polarization provides both an in-plane and an out-of-plane electric field component, the latter being amplified by the larger vertical polarizability of the gold-coated probe. All PTIR data provided in the main text were obtained using p-polarized light (inset of Fig. 2.7d) since this illumination condition provides the most interesting results.

The PTIR spectra from the center of representative frustums (Fig. 2.7d) highlight a broad range of optical modes and a systematic mode dispersion as a function of A_r. Although some of these resonances appear to directly correlate to those previously observed in both far-field[45] and s-SNOM[141] measurements, several additional, strong modes are observed. Particularly, many of the strongest resonances are observed at frequencies above $\approx$ 1550 cm^{-1} (i.e. above the $m = 1, n = 0, l = 1$ resonance for the smallest $A_r$frustums) and were not reported for any of the arrays in prior works. Because each of the modes observed in the PTIR spectra show a systematic dispersion with the A_r, we deduce that these resonances are indeed HPhP resonance modes. Furthermore, in contrast with previous s-SNOM observations[141], PTIR spectra obtained at different locations on a given frustum (see Fig. 2.7e) display clear spectral variations. This is

most likely related to the how well the AFM tip can launch HPhPs while in contact with the frustum, rather than to the launching of the HPhPs by the sharp frustum corners.

The extension of the analytical calculations beyond the $(l10)$ case to include those with $m = 0$ and $n > 0$ in the upper Reststrahlen band, offers a rich and complex dispersion relationship (see Fig. 2.8a). Here, the hyperbolic dispersion is represented as a function of A_r with the gray-scale corresponding ro the calculated Purcell factor for the mode. To limit the complexity of the plots, only HPhPs with m = 0 or m = 1 and $n = [(l - m)/2] \leq 2$ are given. In this dispersion plot of Fig 2.8a, we observe a series of limbs each corresponding to different m and/or n. Each limb is

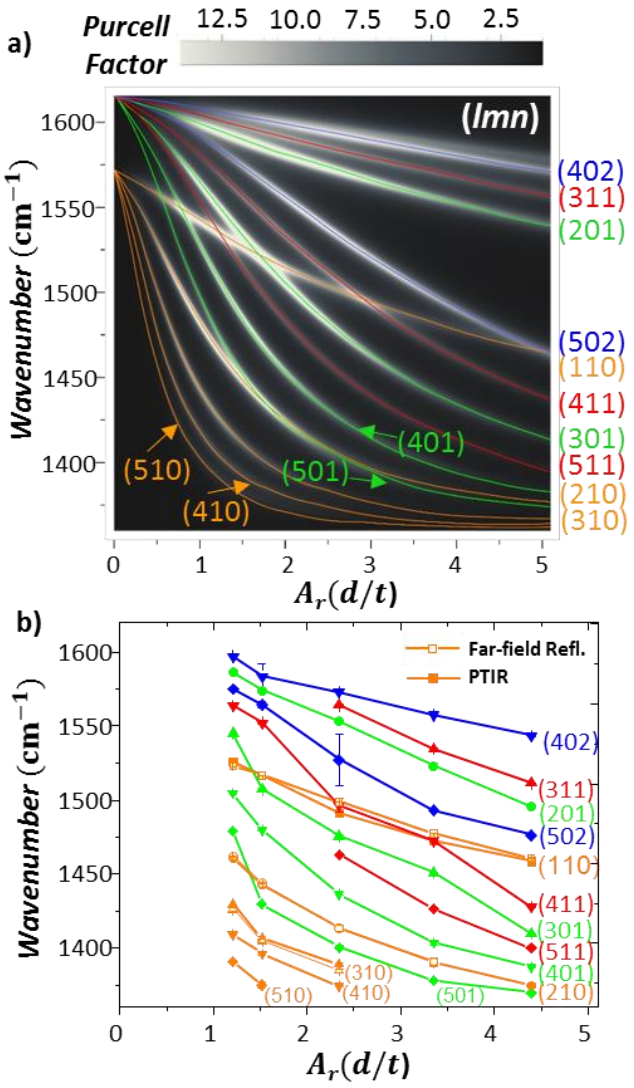

Figure 2.8 *a) Analytical calculations of the HPhP dispersion for hBN ellipsoidal particles as a function of the Ar. Four specific 'limbs' are observed with multiple dispersing polaritonic modes. The gray-scale represents the corresponding Purcell factor, while the colored lines are provided as a guide to the eye and identify the* $(l10)$ *(orange traces),* $(l11)$ *(red traces),* $(l01)$ *(green traces) and* $(l02)$ *(blue traces) limbs of the* A_r*-dependent HPhP dispersion for hBN ellipsoidal particles. b) PTIR (full symbols) and FTIR (open symbols) experimental* A_r*-dependent dispersion from each of the five frustums measured in Fig. 1b. The modal assignments are in good qualitative agreement with the analytical calculations. The color lines and symbols, along with the (lmn) designations are provided for easier comparison with the calculations. The dispersion of the three observed resonances within the far-field reflection are also provided as the open circles and correspond to the (110), (210) and (310) branches. The error bars represent a single standard deviation of the resonance peak position uncertainties determined by the least-squares*

composed of several branches of varying l, with each limb designated by solid lines of the same color in Fig 2.8a, which are provided as a guide to the eye. The previously reported $(l10)$ limb is highlighted in orange. The previously unreported limbs [$(l02)$; blue], [$(l11)$; red], and [$(l01)$; green] are also included. We now compare these theoretical curves with the observations. Close examination of the PTIR spectra for each A_r demonstrates several series of dispersing resonant modes. Using the dispersion plot in Fig. 2.8a as a guide, we can employ least-squares fitting of the resonances observed in the PTIR absorption spectra, to assign and group the experimentally observed modes into corresponding limbs and branches (Fig 2.8b) that qualitatively match the analytical calculations (Fig 2.8a). While the sheer number of resonant modes observed in the PTIR experiment makes the unambiguous identification of each resonance challenging, the good qualitative agreement supports our assignments. Furthermore, because least-square fitting of the far-field reflectance data enabled the identification of the $(l10)$ (open orange symbols in Fig. 2.8b) we could compare the HPhP spectral positions of these modes with those observed in the PTIR spectra directly. The good match between the FTIR and PTIR spectral positions (Fig 2.8b) adds additional confidence to the spectral assignments. Regardless of the specific assignments, our analysis clearly demonstrates that the additional resonances observed here are consistent with those previously anticipated by theory, 30 including the modes occurring at frequencies higher than the frequency of the (110) mode. As noted above, with the exception of the $(l10)$ limb, the hBN resonances have not been experimentally observed previously owing to the limitations imposed by the far-field selection rules, highlighting the power of the PTIR technique for nanophotonic modal observation and analysis.

For the analytical calculations (Fig. 2.8a), the hBN nanoparticle was modeled as a spheroid. Its polaritonic eigenmodes were found solving numerically the transcendental equation given in

previous work. (Note the small difference in notations: the mode indices l, m, n here correspond to l, m, r in Refs. [45] and [148]). We represent the AFM tip by a point dipole emitter placed above the north pole of the spheroid. The dipole axis is specified by a unit vector **d**, which we chose to be 45 degrees with respect to the equatorial plane of the spheroid plane of the spheroid. We assume that the PTIR signal is proportional to the Purcell factor of the emitter, $f = 1 + (3/2)(\lambda_0/2\pi)^3 \mathrm{Im}(\mathbf{d} \cdot \mathbf{E})$, where λ_0 is the vacuum wavelength of light and **E** is the reflected electric field at the dipole's location. The calculation of the Purcell factor is performed by expanding **E** in spheroidal harmonics according to the formulas given in the Supplementary Material of Ref. [148].

In summary, the PTIR technique was used here to provide the first observation of non-radiative HPhP modes in hBN, enabling the detection of up to five branches of four different limbs of the A_r-dependent hyperbolic dispersion relationship. Such non-radiative modes were predicted theoretically[148], however, their far-field selection rules have precluded their direct observation in previous experiments. The PTIR near-field detection, mediated by the sample thermal expansion, enables the detection of these dark HPhP modes. The comparison of the rich PTIR spectra with the calculations of the A_r-dependent dispersion for ellipsoidal nanoparticles, for which an analytical solution is available, provided the basis for the assignment of the quantum numbers defining each limb and branch to the experimentally observed modes. The PTIR absorption maps also enabled the visualization of the frequency-dependent evolution of the local resonant absorption. More broadly, these results also highlight the capabilities of the PTIR method in characterizing nanophotonic materials and nanostructures that are complementary to the more traditional techniques such as far-field reflection/transmission spectroscopy and s-SNOM.

2.4.2 High-Q Dark HPhPs in hBN Nanostructures

In the previous section, the PTIR technique was able to measure a suite of additional resonances[156] that were originally predicted in hBN nanostructures[148], but were not accessible in far-field and s-SNOM measurements. The origin for this difference is a topic of debate, however, a clear methodological difference stands in the signal detection scheme. In s-SNOM, the AFM cantilever oscillates periodically above the sample (tapping-mode) and the tip-scattered light is measured optically in the far-field. In contrast, PTIR typically operates with the AFM cantilever in contact with the sample (i.e. contact-mode) and directly transduces mechanically the sample photothermal expansion to measure light absorption[114]. It was suggested[156] that the different PTIR and s-SNOM sensitivities for detecting these additional higher-order dark and weakly scattering modes may originate from the different probe operation schemes or from the intrinsically different detection mechanisms, which for PTIR does not require scattering towards the (s-SNOM) far-field detector. In support of the latter argument, PTIR has, for example, enabled efficient detection of dark, i.e., weakly-scattering, plasmonic modes as well[116,123].

Here, we leverage the conventional contact-[157] and the newly-introduced tapping-mode[158,159] PTIR measurement modalities to test the prior hypothesis and pinpoint the origin of the peculiar sensitivity of the PTIR technique to these dark HPhP modes. The demonstration of nominally identical results in the hBN frusta we studied, regardless of the probe operation (tapping vs. contact modes), rules out the AFM probe operation as the reason for the discrepancies between s-SNOM[61] and PTIR measurements[156]. Theoretical modelling of the PTIR near-field response as a function of the distance between the tip and the frustum surface also shows distance-independent excitation of dark HPhPs, well correlated with our experimental observations. Furthermore, PTIR measurements show that high-Q (up to ≈ 280) HPhP resonances that are preserved to first approximation even in high density hBN frustum arrays. Such observations contrast with the

typical behavior of plasmonic and surface phonon polariton (SPhP) resonances, where the *Q*-factor and the optical cross-section are typically degraded by the proximity of other nanostructures[124,132]. We attribute such key differences to the progressively stronger confinement of the higher momenta HPhPs within the volume of the frusta, which reduces the influence of environmental permittivity and inter-particle coupling on the *Q*[66]. Since dark and weakly scattering resonances typically have higher *Q*s than bright modes resulting from the reduced radiative contribution to the scattering lifetime, our measurements suggest that PTIR direct near-field detection is the likely enabling reason that, for the frusta studied here, permits a more complete characterization of polaritons than with s-SNOM. We believe that the combination of high-*Q* and the high densities of nanostructures demonstrated in this work, holds great promise for applications in sensing and quantum emission, while also demonstrating the emerging potential of PTIR as a novel tool for characterizing nanophotonic media in the IR.

In PTIR, a pulsed laser (*p*-polarized) illuminates an area of ≈ 40 μm diameter centered around the AFM tip, much larger than the frusta studied here. Sample-1 is characterized by h_1 = 262 nm ± 1 nm and d_1 = 1219 nm ± 27 nm, i.e. Ar_1 = 4.65 ± 0.11 (see Fig 2.9) while sample-2 features h_2 = 317 nm ± 6 nm, d_2 = 367 nm ± 8 nm, and thus an Ar_2 = 1.16 ± 0.03, (Fig. 2.10), with the latter representing the same hBN frusta array measured previously by s-SNOM[61]. The uncertainties in the nanostructure dimensions represent one standard deviation in the AFM topography measurements of the same nanostructure along different directions. The nanostructure dimensions were obtained from separate linear fits of the baseline, plateau, and side walls of tapping-mode topography line cuts, which provide a more accurate A_r estimate with respect to our previous work[156]. Our previous measurements of the hBN frusta were obtained with the same illumination geometry using the conventional, non-resonant PTIR excitation

scheme in contact-mode, i.e., with a 1 kHz laser repetition rate, which is well below the cantilever contact resonance frequencies (typically 100 kHz to 350 kHz)[156]. To increase the PTIR sensitivity, here we leverage three distinct recently introduced resonance-enhanced detection schemes for operation in contact-[157,160] or tapping mode[158,159,161,162]. Two distinct AFM probes were used: the softer probe-A (1 N/m to 7 N/m nominal stiffness) was used both in contact-mode (PTIR spectra and images) and tapping-mode (PTIR images only) to measure sample-1, while the stiffer (≈ 40 N/m) probe-B was used for tapping-mode only (PTIR images and spectra) to measure sample-2 and 3. The "hybrid" mechanical characteristics of probe A are a compromise, i.e. a bit too stiff for contact-and too soft for tapping-mode. On the samples analyzed here, in general probe-A offers better performance in contact- than tapping-mode since some speckle or streak artefacts can be seen in the tapping-mode maps (Fig. 2.9b) and leads to unusable, high-noise tapping-mode PTIR spectra. Nevertheless, by enabling both contact and tapping image modalities, probe-A permits a direct comparison that unambiguously establishes the independence of the probe detection scheme from the ability to observe dark-modes with PTIR.

For this we analyze sample-1 (Ar =4.65) in both contact-mode (Fig. 2.9a) and tapping-mode (Fig. 2.9b) using probe-A. The PTIR contact-mode images (Fig. 2.9a) reproduce our previous measurements on similar frusta well[156], and enable 8.3-fold faster imaging thanks to the higher throughput of the resonant detection scheme[157,163] adopted here. The PTIR images in Fig 2.9a show polariton near-field patterns evolving as a function of the incident frequency, as expected for a hyperbolic medium where the polariton propagation angle is dictated by the frequency-dependent dielectric function[86]. In contrast with previous s-SNOM images[141] that showed strong intensities only on the sidewall of the frusta, the PTIR images in Fig. 2.9 depict strong near-field intensities towards the center of the frustum, in agreement with our previous measurements[156].

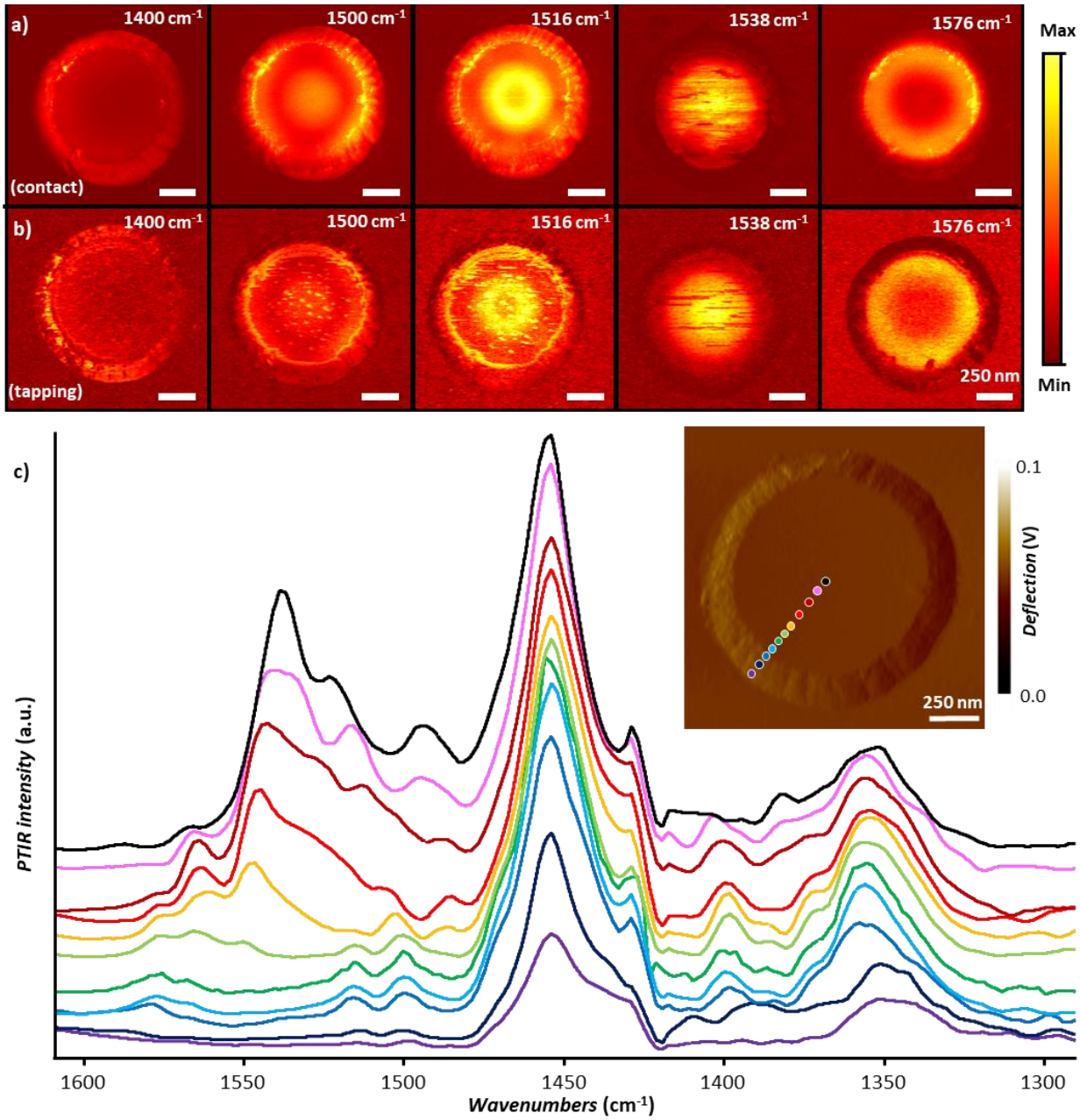

Figure 2.9 *a) Contact-mode and b) tapping-mode PTIR absorption maps for an hBN frustum of A_r = 4.65 ± 0.11. All images (5 nm pixel resolution) were obtained with a scan rate of 0.5 Hz using the same AFM cantilever (probe-A). c) Contact mode PTIR absorption spectra obtained at the color-coded positions marked in the inset. The spectra were smoothed by considering 7 adjacent points and are displayed in common scale and with an offset for clarity. The inset displays the AFM deflection image of the frustum. Scale bars are 250 nm*

Beside few speckle or streak artefacts, particularly visible in the tapping-mode maps, the PTIR tapping-mode (Fig. 2.9b) and contact-mode (Fig. 2.9a) images on sample-1 are nearly identical,

suggesting that the probe operation (contact or tapping) cannot explain the differences between prior PTIR16 and s-SNOM measurements[141].

HPhPs exist only in the narrow, fixed spectral window delimited by the optic phonon pairs (Reststrahlen band) of the hyperbolic material. PTIR contact-mode spectra on the same frustum (Fig. 2.9c) reveal several polaritonic resonances within hBN upper Reststrahlen band (i.e., between approximately 1610 cm^{-1} and 1360 cm^{-1})[64,164]. Consistent with Fig. 2.9a, b, the PTIR spectra show strong intensity at the center of the frustum and relative peak intensities that are a function of the tip position, confirming our previous results[156], but in contrast with prior nano-FTIR spectra that were essentially invariant with the tip position[141]. Interestingly, some spectral features occur at the same frequency independent of the spatial location of the tip (i.e., peak at roughly 1455 cm^{-1}), while others shift in frequency as a function of tip position (peaks occurring at frequencies larger than 1550 cm^{-1}). Through comparison with prior far-field results[141,164], it is determined that the former correspond to modes that couple to the far-field. In contrast, the spectral features that shift in frequency with probe position correspond to HPhPs with centrosymmetric near-field distributions (see Fig. 2.9) that were not detected by s-SNOM or by far-field FTIR and thus were previously assigned as dark and/or weakly scattering higher-order HPhPs[156]. Thus, we deduce that the AFM tip is crucial for launching at least the polaritons at frequencies above 1550 cm^{-1} in PTIR experiments. This differs from s-SNOM, where the detected modes were assigned to polaritons launched by the resonant frustum cavity itself.

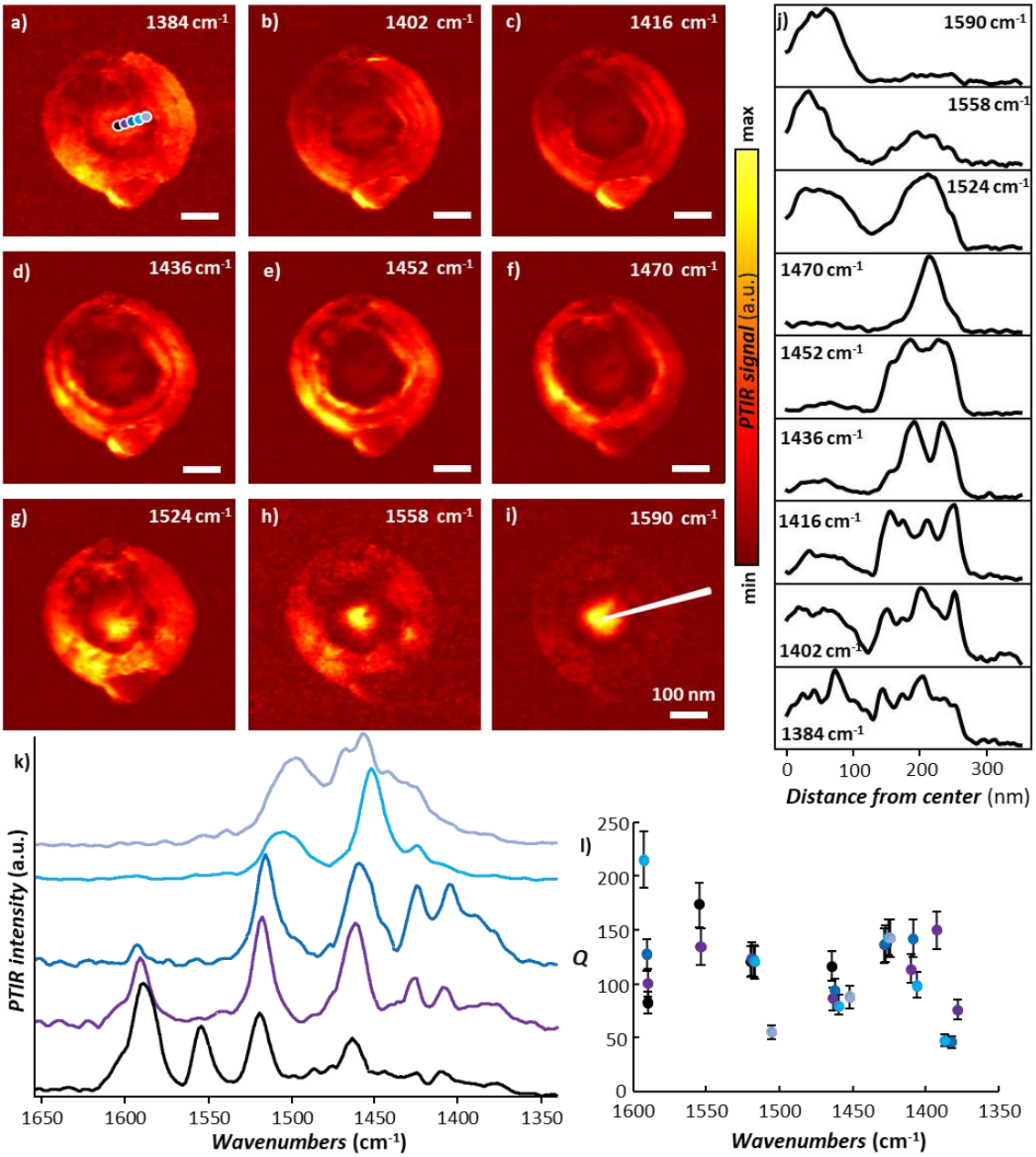

Figure 2.10 *a-i) Tapping-mode PTIR absorption maps for an hBN frustum of Ar = 1.16 ± 0.03. All images (3 nm and 7.5 nm pixel resolution in the horizontal and vertical directions respectively) were obtained with a scan rate of 0.6 Hz using probe-B. Scale bars are 100 nm. j) Line cuts of the PTIR images along the direction indicated by the white line in panel-i. k) Tapping-mode PTIR spectra obtained at the color-coded position in panel-a. The spectra are displayed in full scale with an offset for clarity. l) Q-factors of the polariton resonances obtained from the color-coded spectra in panel-k. The error bars represent a single standard deviation in the determination of Q and mainly determined by the uncertainty of determining the peaks FWHM via the least square fitting the resonances with Lorentzian peak shapes.*

The tapping-mode PTIR absorption images at 1402 cm^{-1}, 1416 cm^{-1} and 1436 cm^{-1} (Fig. 2.10 b-

d) show several concentric rings on the frustum sidewall, similar to previous s-SNOM measurements[141]. However, in contrast to those efforts, the PTIR images in Fig. 2.10 b-d again exhibit significant near-field intensity at the center of the frustum, thus providing a more complete characterization of the polaritonic modes. The intensity at the frustum center becomes the strongest feature for images obtained at frequencies greater than 1524 cm^{-1} (Fig. 2.10 g-i). For comparison, Fig. 2.10j displays line cuts along the marked direction in the PTIR images (in Fig. 2.9a-i). Previous s-SNOM images were interpreted as the result of polaritons15 launched at the intersection of the sidewall with the frustum base and reflecting on the frustum sidewall. In PTIR, however, one would expect that for polaritons launched efficiently in the far-field, for example by the frustum base, would result in a spatially homogeneous signal, because the high hBN thermal conductivity and short HPhPs lifetime (< 10 ps) would conduce to homogeneous frustum heating during the much longer (80 ns) laser pulses. Consequently, the polaritons in Fig. 2.10 must be tip-launched. Therefore, the PTIR intensity reflects the local coupling efficiency between the wavelengths in free space and the tip-launched HPhPs, leading to a strong signal when and where the HPhP near-fields are strongest. This hypothesis is corroborated by the tapping-mode PTIR spectra (Fig. 2.10k) that reveal a series of very sharp polaritonic resonances whose relative intensities depend strongly on the AFM tip position. The *Q*-factors of many of these resonances are high (typically between 50 and 200) with the sharpest peak reaching *Q* values of ≈ 215, approaching those reported from far-field spectra[164] and later via s-SNOM in isotopically enriched hBN frusta[165]. Such large values of Q are presumably the result of the weak radiative coupling of these dark and weakly scattering HPhPs to free-space and may underline the different PTIR and s-SNOM sensitivities.

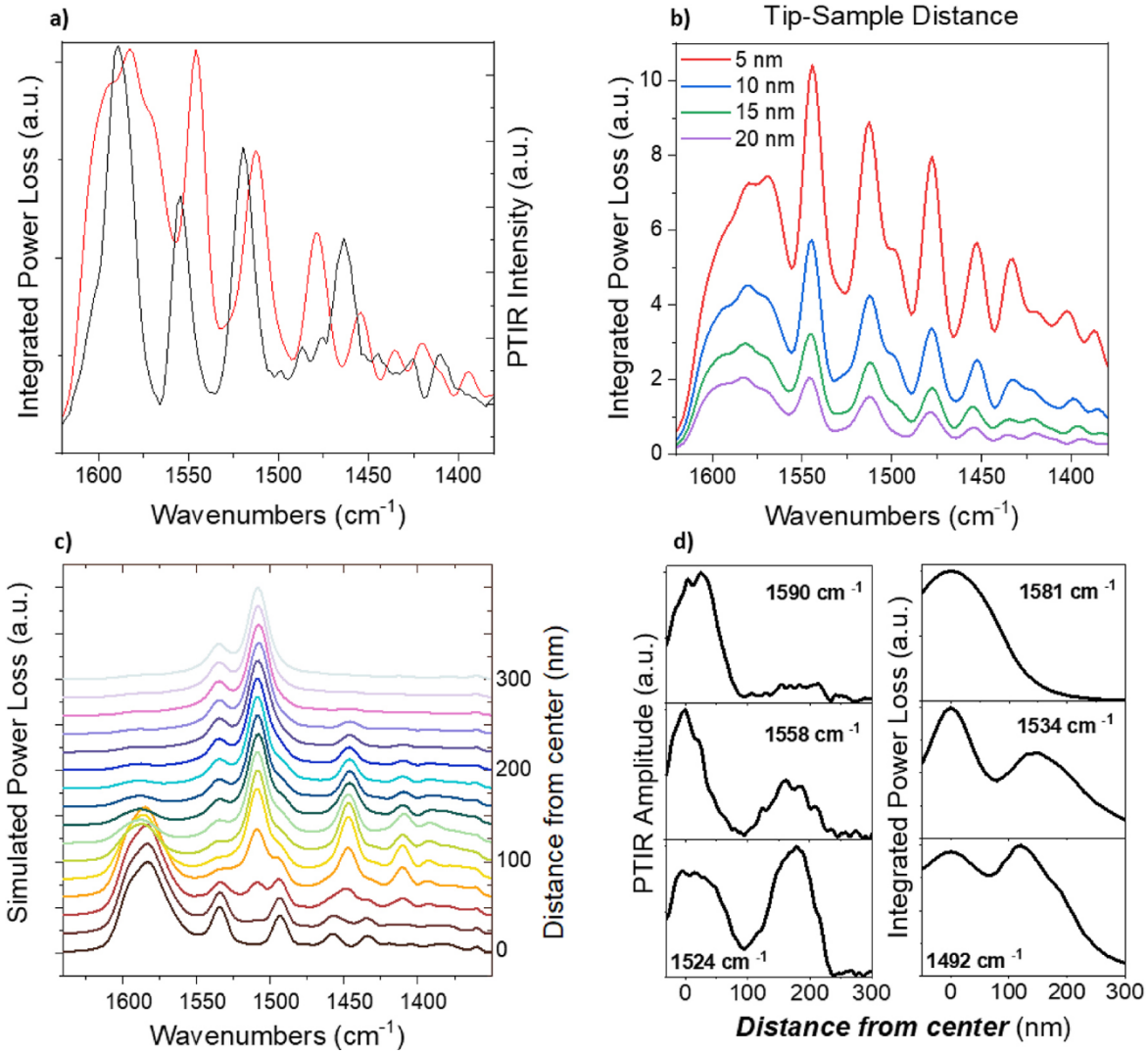

Figure 2.11 *a) Comparison of the experimental PTIR spectrum (black) and simulated power loss spectrum (red) obtained by positioning the AFM tip in the center of an isolated frustum of Ar ≈ 1.16. b) Simulated PTIR spectra in the center of an Ar ≈ 1.16 frustum as a function of tip-sample distance. c) FDTD integrated power loss spectra as a function of tip radial location (corresponding to Figure 2.10k). Spectra are shown from the center of the frustum (bottom) to 300 nm away from the center, in 20 nm increments. d) Comparison of line cuts from PTIR scans of an Ar ≈ 1.6 frustum (Figure 2.10j) on the left, to the corresponding line cuts from FDTD simulations on the right, demonstrating agreement in spatial mode profile. Frequencies of line cuts are chosen for the peak center positions in the center experimental and simulated spectra identified in panel a)*

We simulated the PTIR experiments on sample-2 (Ar = 1.16) using a finite difference time domain (FDTD) solver. The AFM tip was modeled by a discrete port mode positioned within a thin silicon shell in order to mitigate non-radiative coupling to the sample. This tip was positioned at various positions above the simulated frustum in order to determine the height and

radial position dependence of the PTIR signal. The frustum is located in the center of a 3 μm thick substrate, with open boundary conditions in all directions. The PTIR spectra were calculated by integrating the power loss density in the frustum at each frequency, with 0.05 cm^{-1} spectral resolution.

By exciting the frustum with a near-field dipole source and integrating the power loss into the hBN, a similar response to the experimental observation is obtained (Fig. 2.11a). To gauge the impact of probe operation, we varied the distance between the dipole source and the frustum surface (Fig. 2.11b) and observed a spectral response that remains qualitatively unchanged, although with considerable change in intensity. Next, to assess the spatial distribution of the modes we radially translated the dipole source outwards from the frustum center (Fig. 2.11c, d). Comparison with the line cuts and spectra in Figure 2.10j, k, shows strong qualitative agreement to the experiments. Since the simulated spectra are obtained integrating light absorption through the full structure, this result further demonstrates that the spatial variation is due to the spatially varying tip-coupling efficiency of the incoming light rather than differences in the local thermal expansion. Overall, these results support the conclusion that the mode of probe operation cannot explain the different PTIR and s-SNOM sensitivities to dark and weakly scattering HPhPs.

In summary, we conclusively and unambiguously identified that the mode of operation (contact or tapping) of the AFM probe is not the discriminating factor enabling the observation of dark and weakly scattering higher ($n > 0$) order HPhP modes within nanostructured hyperbolic materials. This conclusion is manifested in the PTIR spectra and maps on hBN frusta that are unchanged in character when measured in contact- or tapping-mode. Further, by employing the recently developed and gentler PTIR tapping-mode operation, we successfully measured near-field spectra and maps of the same delicate frusta originally probed by s-SNOM and nano-FTIR

(also operated in tapping-mode), again clearly observing the higher order modes not detected in those samples in prior s-SNOM investigations. In general, the novel PTIR tapping mode paradigm is well suited to measure rough, delicate or sticky samples, which are notoriously difficult to measure in contact mode, with the added benefits of a bit higher (≈10 nm) spatial resolution[157,159] than in contact-mode (≥20 nm)[123,166]. PTIR spectra reveal polaritonic resonances with high-Qs (up to 280). Taken overall, our measurements suggest that the ability of the AFM probe to directly transduce the near-field absorption in PTIR experiments is likely the determining factor that enables the observation of such high-Q polaritonic dark resonances. We understand this as follows. Although the role of the gold-coated AFM tip in launching the polaritonic resonances in the nanostructures is the same in s-SNOM and PTIR; the detection of the near-field tip-scattered light in s-SNOM provides near-surface sensitivity to light absorption in the hBN frusta. In contrast, the thermal-expansion-based PTIR transduction provides sensitivity to light absorption within the whole nanostructure. Since for dark (n > 0) modes the field distribution is weak on the nanostructure surface and strong within the nanostructure volume, the PTIR technique is well suited to study these typically elusive modes. We believe that this work will stimulate research leveraging naturally hyperbolic materials for sensing and quantum emission applications, while improving our understanding of the comparative merits of these two distinct nanoprobe techniques.

2.4.3 Using PTIR to Confirm Long HPhP Lifetimes in Isotopic $h^{10}BN$

After leveraging the PTIR technique to gain new insights over s-SNOM measurements in hyperbolic resonators – we compare the techniques in the more general case of an hBN flake, which is intrinsically advantageous for realizing waveguides and hyperlenses[76,78,143,167] among other devices. In particular, we push the limits of the polariton propagation using isotopic

enrichment - a useful strategy to increase phonon lifetimes in materials composed of atoms with multiple naturally occurring isotopes (such as hBN) since, in addition to point defects (i.e., impurities), the scattering of optic phonons depends strongly on isotopic disorder[168,169]. For example, intrinsic HPhPs lifetimes (τ), propagation lengths (L_p), and figures of merit (i.e., the polaritons Q in Fourier space) were predicted to improve for hBN[61,168,169] containing pure (100 % ^{10}B, to range between $\tau \approx 3.3$ ps[168] and 7.5 ps[61]) compared to naturally abundant boron (80 % ^{11}B, 20 % ^{10}B, $\tau \approx 1.5$ ps)[168] at room temperature. Increased lifetimes and propagation lengths have been experimentally confirmed in near-monoisotopic (≈ 98.7 % ^{10}B, ≈ 99.22 % ^{10}B [170], and ≈ 99.2 % ^{11}B[171]) samples using scattering-type near-field optical microscopy (s-SNOM). However, the measured values at room temperature ($\tau < 1.2$ ps, $L_p < 4$ μm, $Q \approx 40$ for 98.7 % ^{10}B[61], $L_p < 8$ μm, $Q \approx 50$ for 99.22 % ^{10}B[170], and $L_p < 5$ μm, $Q \approx 30$ for 99.2 % ^{11}B)[171] were significantly lower than theory predictions[168]. Giles *et al.*[61] proposed that for a flake ≈ 10 μm in width, HPhPs launched from opposite edges can interfere in the middle leading to discrepancies with predicted values. In addition to that, here we will show that the limited scan size (comparable to L_p) afforded by smaller flakes provides an insufficient accuracy for evaluating L_p and τ[61].

In this work, we leverage photothermal induced resonance (PTIR)[114,126] measurements using a tapping-mode heterodyne detection scheme[159] to measure, with nanoscale resolution, HPhPs propagating in isotopically enriched (≈ 99 % ^{10}B) hBN flakes with lateral dimensions up to 120 μm × 250 μm. Fourier analyses of real-space PTIR images yields the HPhP dispersion relation with lifetimes up to ≈ 4.2 ps, propagation lengths up to ≈ 25 μm, and record-breaking Q (up to $Q \approx 90$), approaching the values previously predicted by theory[61,168,169]. This confirms the predicted dominant role of isotopic disorder, over anharmonic and impurity background decay

channels, in determining the lifetimes of optic phonons in hBN[169] Not only are those values the highest reported at room temperature for isotopically enriched hBN, the propagation lengths and Q reported here exceed previously reported values ($L_p \approx 8$ μm, $Q \approx 60$) for ≈ 99 % ^{10}B at cryogenic temperatures (45 K)[170]. We show that s-SNOM data validate the PTIR measurements and that for comparing properly these two nanoscale IR techniques it is critical to account for the light incident angles with respect to the sample plane and crystal edges that are typically different in the two setups. In addition to HPhPs, we also observe weakly confined modes both within and below the hBN Reststrahlen band that we attribute to light guiding within hBN flakes.

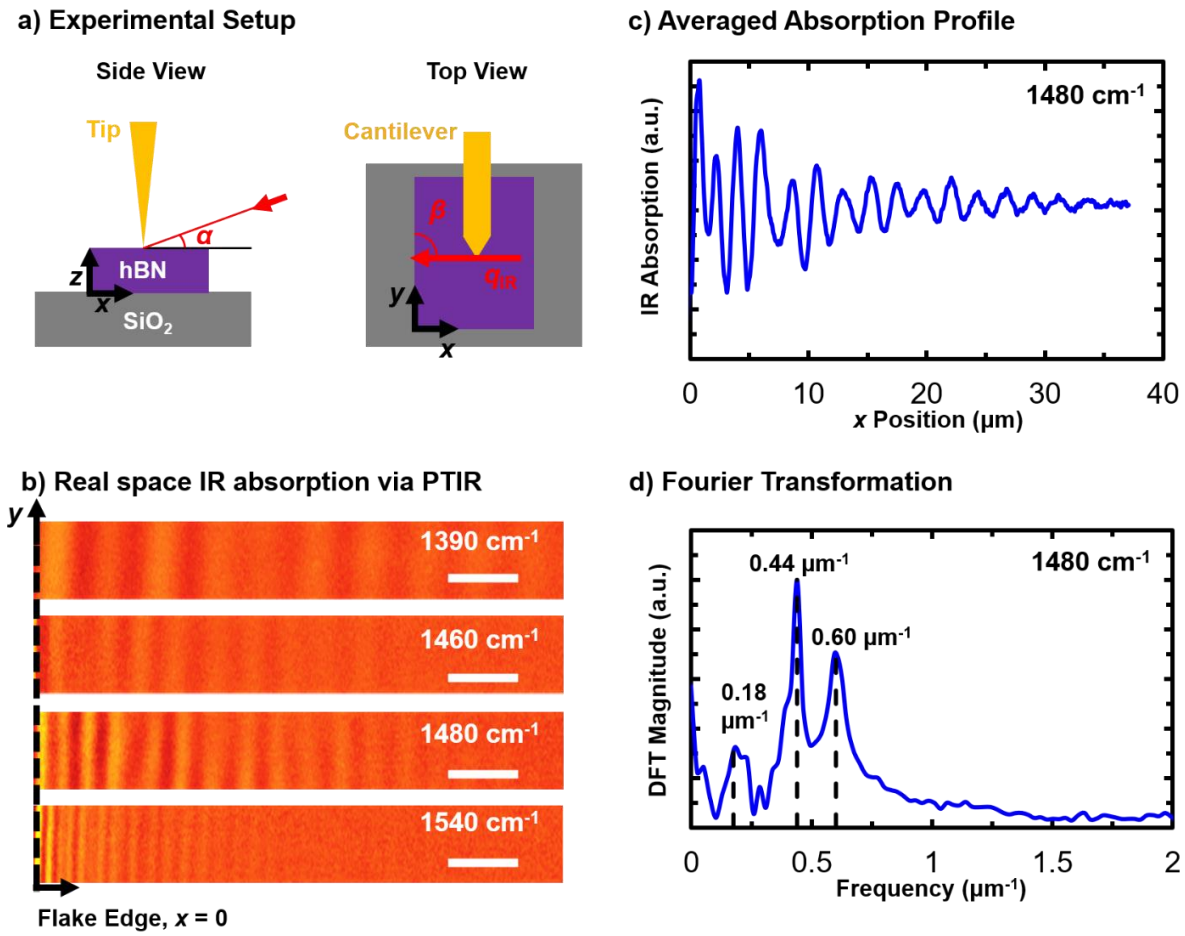

Figure 2.12 *a) Schematic of the sample illumination in photothermal induced resonance (PTIR) experiments. Infrared light (red arrow with wavevector q_{IR}) is incident upon the sample at an angle of α with respect to the plane of the sample, and an angle β with respect to the flake edge. b) Real-space PTIR images of hyperbolic phonon polaritons (HPhPs) in an isotopically enriched ($^{10}B \approx 99$ %) hBN flake (≈ 147 nm thick) obtained by illuminating the sample with different wavelengths. The scale bars represent 5 μm. c) Representative column-wise averaged absorption line profile (measured at 1480 cm^{-1}) as a function of the flake edge (x = 0) distance. d) Discrete Fourier transform (DFT) of the absorption line profile in (c) revealing multiple HPhP excitation modes at distinct spatial frequencies.*

When a hyperbolic material is nanostructured or confined in one or more directions (i.e., in a thin flake), HPhP propagation is permitted only for specific (quantized) momenta that are dictated by the permittivity tensor of the material and its finite size[148,172]. Typically, light-scattering sites such as flake edges or the probe tip are necessary to launch the polaritons

(hereafter referred to as edge- or tip-launched, depending on their origin) as these material discontinuities bridge the momentum gap between photons in free space and the strongly-confined, high-momentum polaritons[173]. While flake edges and the tip scatter light with a continuum of momenta, HPhPs can propagate in the hBN with only a subset of discrete momenta determined by the permittivity tensor. For example, the PTIR images in Fig. 2.12b show the HPhPs propagating for few tens of micrometers within the hBN flake, which are evident as a series of fringes. Edge-launched polaritons propagate and decay in amplitude towards the flake interior, while tip-launched polaritons originate at the probe tip and are detected upon reflection from a flake edge back to the tip. Edge-launched and tip-launched polaritons are a manifestation of the same physical phenomenon, however, tip-launched polaritons (of frequency ω) are detected only after reflecting back to the tip from a material discontinuity (e.g., a flake edge) forming a standing wave interference pattern of frequency 2ω. Therefore, tip-launched polaritons are characterized by fringe periods approximately half that of the corresponding edge scattered polaritons in PTIR and s-SNOM maps[90]. This apparent discrepancy is instrumental in nature due to the tip-scanning measurement. Fourier analysis of real-space PTIR maps (see Fig. 2.12c) more clearly reveal how many HPhP excitation modes contribute to the real-space image as peaks evident in reciprocal space power spectra.

In the PTIR experiments, schematically illustrated in Fig. 2.12a, the sample was illuminated at an angle, α, with respect to the sample plane ($\alpha = 20° \pm 2$) with light incident from the right side ($\approx 90°$ with respect to the longitudinal axis of the cantilever). The uncertainty in the incident angle is an estimate of the angle assessment precision. The samples were mounted on a manual rotation stage that enables controlling the angle between the flake edge and the in-plane propagation direction of the incident light, defined as β (see Fig. 2.12a). The angles α and β are

important to consider when comparing measurements obtained under different conditions or different modalities (i.e., PTIR and s-SNOM) as α affects the near-field tip-enhancement strength[174] and both angles can affect the period of the polariton fringes[171,175,176].

A multi-mode damped harmonic oscillator model was fit to the reduced one-dimensional (1D) PTIR absorption profiles to extract the frequencies associated with each HPhP mode:

$$\sum_{i}^{n} A_i e^{-\gamma_i x} \cos(k_i x + \varphi_i) \tag{2.5}$$

Where *i* indexes each of the *n* independent peaks evident in the Fourier power spectra (Fig. 1d), A_i is a scaling coefficient, γ_i is the damping coefficient, k_i is the spatial peak center frequency (μm^{-1}), and φ_i is a phase shift that accounts for offsets in the relative position of the origin (determined topographically by the flake edge). The angular HPhP wavevector is defined as $q = 2\pi/\Lambda$, where Λ represents the polariton wavelength and is extracted from either the spacing between edge-launched polaritons in the 1D profile or twice the spacing between the tip-launched polariton fringes. Evident by the roughly micron- and submicron-scale fringe spacings in real-space maps, the polaritons enable a strong confinement of light (up to ≈ 7-fold at 1560 cm^{-1}) with respect to the free-space wavelength (λ_{IR}). Subsequent Fourier analyses of the reduced line profiles yield the corresponding polariton wavevectors that, as a function of IR wavenumber, provide the material dispersion relation. In Fig. 2.13, we compare the experimental results with the analytically calculated reflectivity of ≈ 99.2 % isotopically enriched hBN[61]. The analytical dielectric function for ^{10}B ≈ 99 % was calculated by fitting a harmonic oscillator to reflectance spectra[61]. Compared to naturally abundant hBN, both Raman measurements and the fitted reflectance spectra show a significant spectral shift in the TO/LO phonon frequencies (as

well as the damping factors) for the isotopically enriched samples.[27] The comparison reveals multiple, thickness-dependent excitation branches, where a given free-space wavelength is compressed to shorter polariton wavelengths in each successive (higher-order) branch[177]. The first branch, referred to as the fundamental mode (labelled as "Edge-1"), agrees well with the theoretical predictions for both flakes. For the thicker 337 nm flake, we also observe the second-order polariton mode (Fig. 2.13b; labeled "Edge-2"), consistent with previous observations[61]. In addition to HPhPs, fringes with very small wavenumbers (labelled 0 and 0′ in Fig. 2.13) were observed in both flakes, which we attribute to waveguide modes.

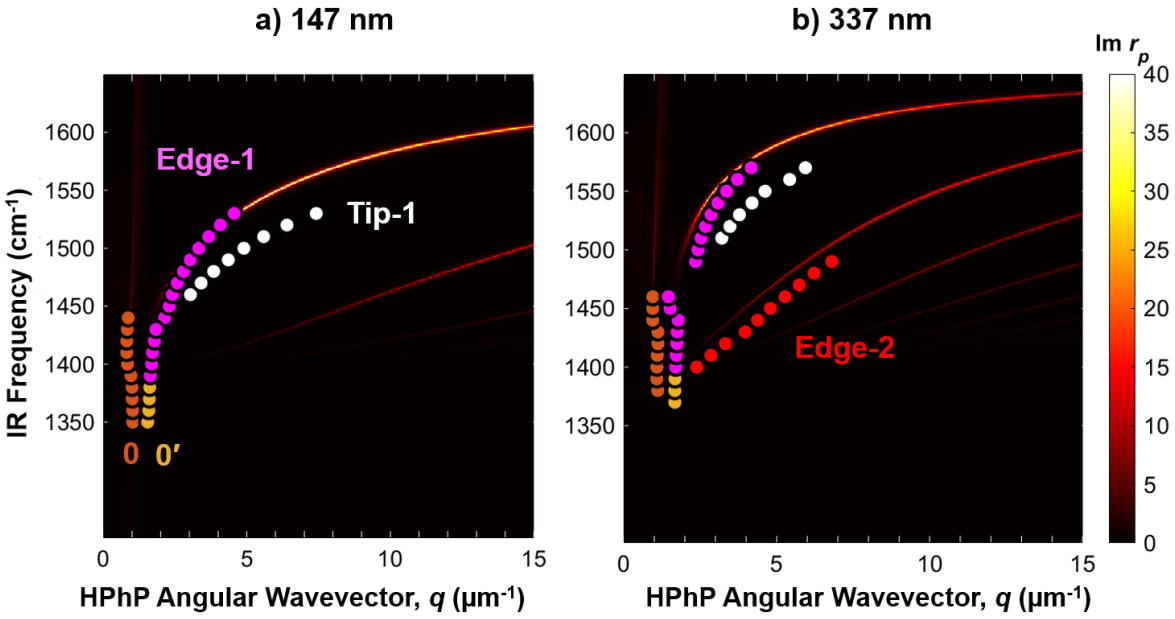

Figure 2.13 *Comparison of the as-measured hyperbolic phonon polariton (HPhP) wavevectors, q (obtained from PTIR imaging analysis), with the calculated dispersion curves based on the dielectric function of the isotopically enriched $^{10}B \approx 99$ % hBN. Results are presented for flakes with thicknesses a) ≈ 147 nm and b) ≈ 337 nm. The experimental data (solid circles) show dispersing branches with progressively increasing momenta and are labelled as Edge-1, Tip-1 and Edge-2. Two low frequency modes are also detected and labelled as 0, 0′. The imaginary component of the computed reflectivity, Im r_p, is represented in the underlying colormap and is used as a proxy for the theoretical HPhP dispersion.*

Notably, for both flakes, an "extra branch" (denoted as "Tip-1") is detected with momenta between the Edge-1 and Edge-2 branches. As mentioned previously, s-SNOM data on 2D hyperbolic flakes have revealed the coexistence of both tip- and edge-launched HPhPs, with the tip-launched modes having approximately double the measured frequency of the edge-launched variety[61]. However, the ratio between Tip-1 and Edge-1 momenta ranges from about 1.26 (at 1460 cm^{-1}) to around 1.70 (at 1550 cm^{-1}) for the 147 nm thick flake and between 1.27 (at 1510 cm^{-1}) to 1.42 (at 1570 cm^{-1}) for the 337 nm thick flake. These results suggest that the ratio is not constant (≈ 2) as expected. The effect of the light incident angles (α, β) on the s-SNOM measured fringe spacing has been reported for surface phonon polaritons in SiC[33,178] and waveguide modes in MoS_2[175] and $PtSe_2$[176] but, it has not been typically considered for HPhPs in hBN since it was previously estimated to be insignificant[179]. Additionally, the effect of the flake edge orientation has been recently shown to affect the relative tip and edge HPhP launching efficiency in isotopically enriched (≈ 99.2 % ^{11}B) hBN[171], but its effect on the fringe spacing has not been detailed. Here, the genuine (g) in-plane wavevectors of the edge launched polaritons were calculated by accounting for the orientation angles[175]:

$$q_{\mathrm{edge,g}} = q_{\mathrm{edge}} - q_{\mathrm{IR}}[\cos(\alpha) \times \sin(\beta)] \tag{2.6}$$

where q_{edge} is the wavevector extracted from the fringe spacing near the edge, q_{IR} is the free-space wavevector of light, α (20°, Fig. 1a) is the illumination angle with respect to the sample plane, and β (90° for the PTIR measurements) is the angle between the direction of HPhP propagation and the sample edge (see Fig. 2.12a). It is noteworthy that the tip-launched HPhPs have been reported to be independent of the orientation of the illuminating field[180]. After calculating the genuine edge-launched wavevectors with Eq. 2.6 we retrieve the expected ≈ 2:1

ratio for edge- and tip-launched polaritons. We believe that Eq. 2.6 has not been typically considered in the previous hBN HPhP literature, because of the typically shorter scan windows employed (8–10 μm) that are comparable with the in-plane component free-space wavelength. Here we show that Eq. 2.6 is required to analyze the wide scan (40 μm) data in our work and that such wide scan lengths are advantageous for accurately measure phonon-polaritons characteristics such as propagation length and lifetimes. Wide scan lengths have a higher resolution for Fourier space analysis (0.05 μm^{-1} for a 40 μm scan vs 0.25 μm^{-1} for an 8 μm scan) and can disentangle the effect of the incident free space wavelength on the measured interference pattern. Consequently, large scans allow: a) to resolve polaritons peak in Fourier space that are narrow, closely spaced or low at frequency; more accurate estimate of the peaks position and linewidth which are directly related to propagation length and lifetimes. Due to the strong relative intensity of the edge-launched HPhPs in the samples measured here, Eq. 2.6 shall be used for comparing PTIR and s-SNOM data and to account for the different illumination conditions in each experimental setup. We also note that such differences may be more apparent in this work due to the very long scans and HPhP propagation reported.

To further corroborate the PTIR analysis, we measured the 147 nm thick hBN flake in a similar location to the PTIR measurements using s-SNOM, the prevalent method for polaritons imaging[181]. In the s-SNOM setup, the sample was illuminated by p-polarized light incident at 30° with respect to the sample plane (α = 30°) and at 225° with respect to the long axis of the AFM cantilever (see Fig. 2.14a). The s-SNOM data were acquired by tapping a gold-coated AFM tip at 271–307 kHz with an amplitude of 65–91 nm and demodulating the 2nd harmonic amplitude signal. The same data processing and Fourier analysis steps used for PTIR were conducted on the reduced s-SNOM line scans (e.g., Fig. 2.14b) to obtain the polariton

wavevectors (Fig. 2.14c). The theoretical dispersion relation determined from the computed material reflectivity method is then compared with the experimental data points in Fig. 2.14d with good quantitative agreement.

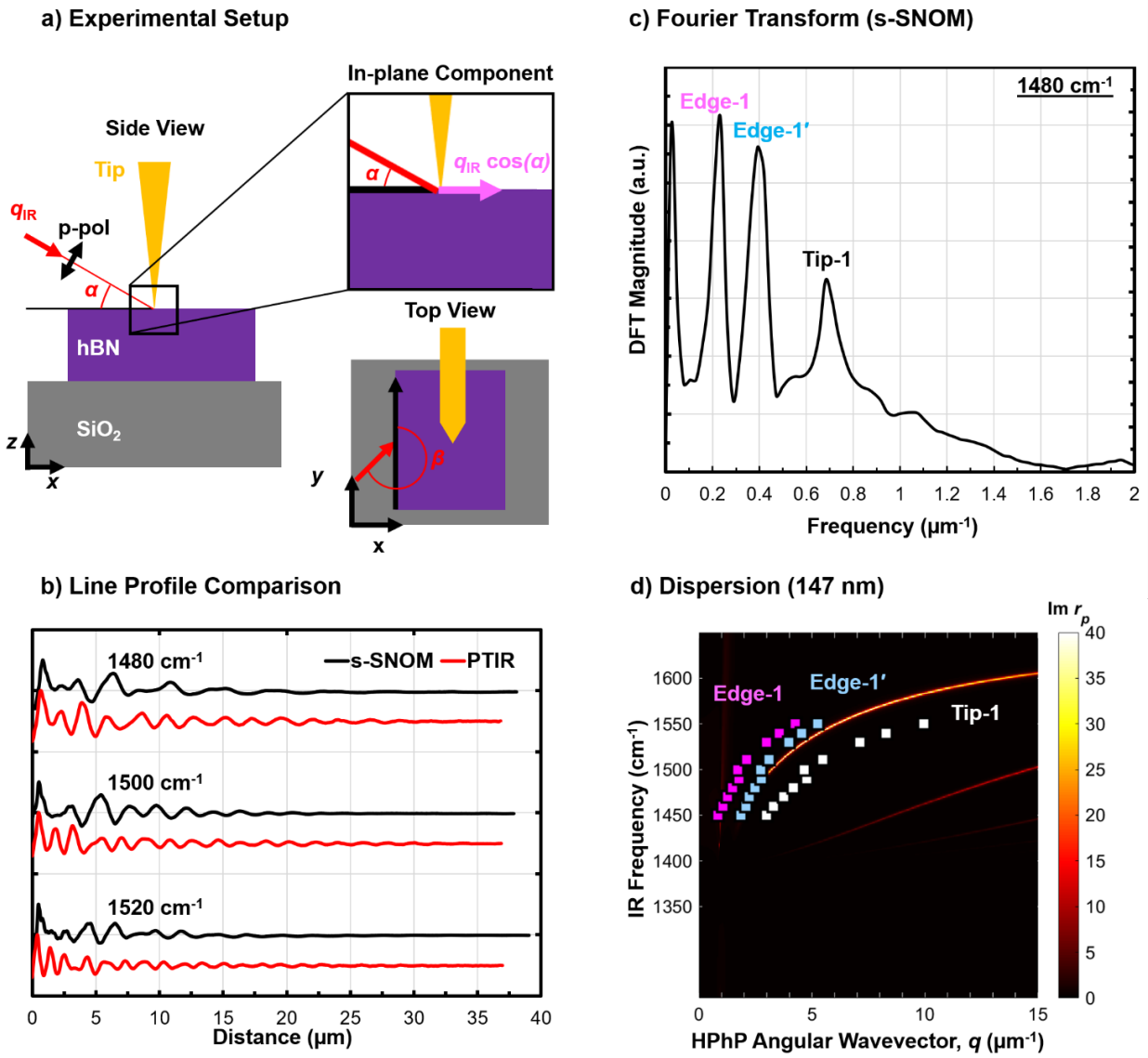

Figure 2.14 *a) Schematic illustrating sample illumination scheme in photothermal induced resonance (PTIR) experiments. Infrared (IR) light (red arrow with wavevector q_{IR}) is incident upon the sample at an angle of α with respect to the plane of the sample, and an angle β with respect to the flake edge. The magnified schematic outlines the in-plane and normal components of the p-polarization (p-pol) light. b) Representative comparison of PTIR and s-SNOM column-wise averaged line scans at different incident IR frequencies. c) Discrete Fourier transform (DFT) of s-SNOM line profile revealing the HPhP spatial frequencies. d) Comparison of extracted hyperbolic phonon polariton (HPhP) wavevectors, q, obtained from s-SNOM imaging to the calculated dispersion curves based on the [^{10}B] 99.22 % hBN dielectric function with 147 nm thickness.*

One peculiar difference between the s-SNOM and PTIR datasets is the unexpected detection of

an additional branch near the first edge-launched branch (denoted as "Edge-1′" in Fig. 2.14d) in the s-SNOM data. This feature is detected only when considering the whole 40 μm wide scan, and it is not detected when truncating the data to a 10 μm scan; due to the insufficient resolution in Fourier space. Notably, calculating the $dq_{\text{Tip-1}}/dq_{\text{Edge}}$ gradient for each branch reveals gradients of ≈ 2.0 for both Edge-1 and Edge-1′ modes suggesting that both branches should be of the edge-type and of the same order. We note that the Edge-1 mode matches the genuine Edge-1 dispersion according to:

$$q_{\text{edge,g}} = q_{\text{edge1}'} + \frac{q_{\text{IR}}}{2}[\cos(\alpha) \times \sin(\beta)] \tag{2.7}$$

Applying Eq. 2.7 to the Edge-1′ branch, the resulting genuine edge polaritons align extremely

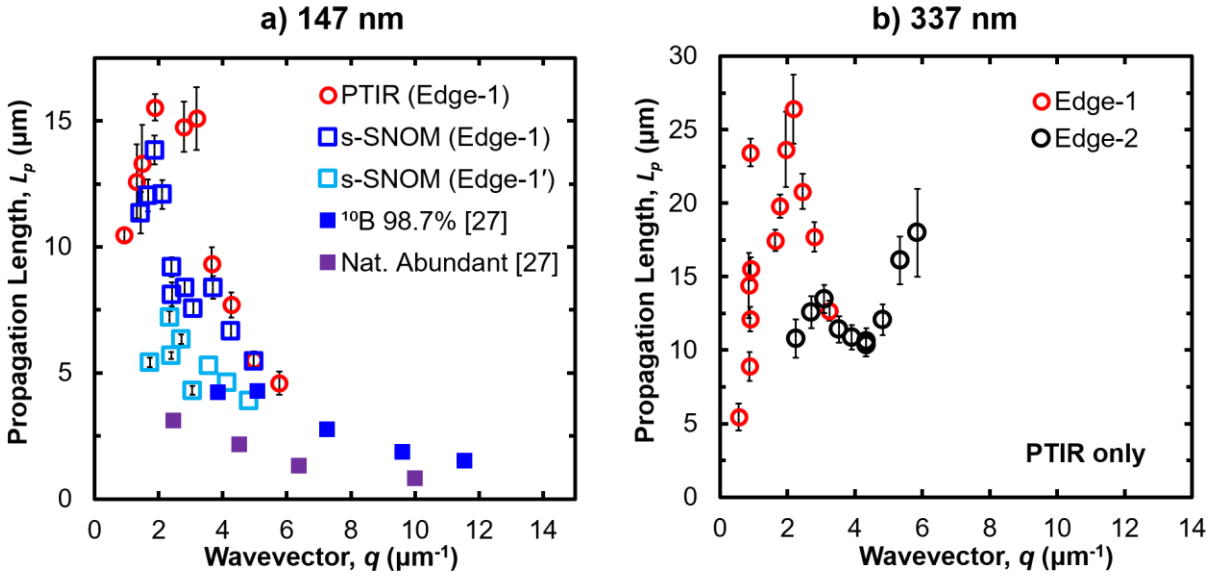

Figure 2.15 *a) Propagation lengths, L_p, for Edge-1 polaritons in a ≈ 147 nm thick ^{10}B ≈ 99 % hBN flake via PTIR (open circles) and s-SNOM (open squares). Propagation lengths are plotted as a function of the genuine in-plane wavevector, q, and compared to previous s-SNOM measurements[27] for a ≈ 120 nm thick ^{10}B 98.7 % hBN flake (solid blue) and natural abundant hBN (solid purple). b) Propagation lengths for Edge-1 (red circles), and Edge-2 (black circles) branches as identified in Fig. 2b for a ≈ 337 nm thick ^{10}B ≈ 99 % hBN flake, as a function of q. The error bars represent the propagated uncertainty in the values of the fitted parameters (95% confidence intervals) used to calculate the propagation length.*

well with the Edge-1,g data for both s-SNOM and PTIR. However, we have not identified which physical mechanism underlies such modified interference pattern.

Next, we extract useful parameters from the data to evaluate and benchmark the characteristics of the measured HPhPs. For each mode, we calculate the propagation length ($L_p = 1/\gamma_n$), where γ_n is the harmonic damping coefficient, and compare the obtained values with prior results on naturally abundant and isotopically enriched hBN (see Fig. 2.15). While previous s-SNOM measurements[61] revealed $L_p < 4$ μm, for a 120 nm thick, h^{10}BN (98.7 %) flake, here we obtain propagation lengths up to ≈ 14 μm (s-SNOM) and up to ≈ 15 μm (PTIR) for a ≈ 147 nm thick flake of the similar nominal isotopic composition (see Fig. 2.14b for a direct comparisons of PTIR and s-SNOM absorption profiles). Such long propagation lengths can be intuitively confirmed by visually inspecting the polaritonic fringe patterns in Fig. 2.12, which demonstrates

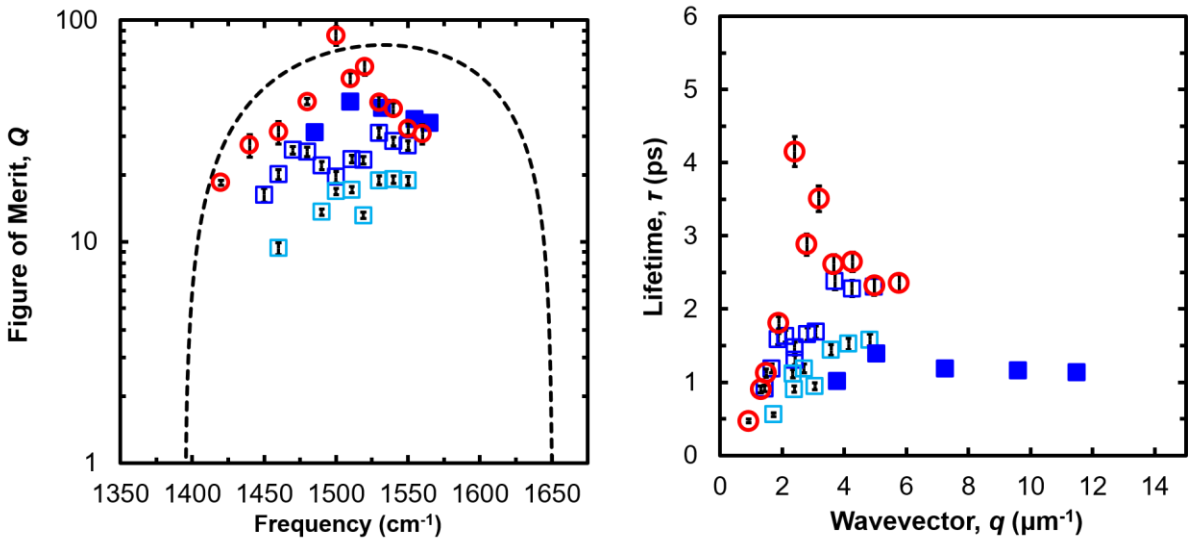

Figure 2.16 *a) Figure of merit, Q, representing the quality of the polaritons and b) lifetimes, τ, for $^{10}B \approx 99$ % isotopically enriched hBN flakes with thickness of ≈ 147 nm estimated via PTIR (open red circles), s-SNOM (open blues squares) and compared to previous s-SNOM measurements for a ≈ 120 nm thick flake of similar composition (^{10}B 98.7 % hBN, solid blue squares). The error bars represent the uncertainty propagation of the fitting parameters (95% confidence intervals) used to calculate the Q and lifetime.*

the benefit of isotopic enrichment in hBN of ≈ 5 × with respect to measurements on naturally abundant materials. Record propagation lengths exceeding ≈ 25 μm (at room temperature) were evident in PTIR measurements on a ≈ 377 nm thick flake (Fig. 2.15b). In agreement with previous results[43], the greater optical confinement (larger q) of the second order mode detected in the thicker (≈ 337 nm) flake, generally results in shorter, but still remarkably long propagation lengths of about 10 μm < L_{P2} < 17 μm (Fig. 2.15b).

To benchmark HPhP performance for nanophotonic applications more quantitatively, next we focus on the fundamental polariton branch and compute the polariton group velocity $v_g = \partial\omega/\partial q$ from the slope of the dispersion curve in Fig. 2.13 and its lifetime (τ) defined as:

$$\tau = \frac{L_p}{v_g}. \tag{2.8}$$

Another useful benchmark that enables comparing polaritons from different materials is the propagating figure of merit (the Q of the polariton in Fourier space) defined as:

$$Q = \frac{\mathrm{Re}(q)}{\mathrm{Im}(q)} \tag{2.9}$$

where Re(q) is the in-plane wavevector and Im(q) is proportional to the fitted half-width at half-maximum of the spectral linewidth extracted from the power spectra in Fourier space.

The resulting Q's and HPhP lifetimes are plotted in Fig. 2.16 and compared with previously reported values measured using s-SNOM on flakes of similar composition and thicknesses[61]. The Q and the polariton lifetimes (up to ≈ 4 ps) obtained for these large, isotopically enriched flakes approach the values predicted by theory[168] for ^{10}B hBN and exceed the theoretical limits for naturally abundant hBN ($\tau \approx 1.5$ ps[168]). The long lifetimes measured here support the hypothesis that the previously reported values for these samples[61] were constrained by the lateral hBN flake size, which we overcome here using flakes with lateral dimensions that significantly exceed the

HPhP propagation lengths and using 40 μm wide scan lengths.

In addition to HPhPs, the PTIR images reveal another set of branches in the hBN dispersion (labelled as "0" and "0′" in Fig. 2.13) that we believe have not been reported previously. These branches are associated with small wavevectors ($\approx 1\ \mu m^{-1}$) that do not disperse strongly as a function of the incident IR frequency and match well the expected light line calculated by the reflectivity model (Fig. 2.13). We attribute these features to waveguide-like modes (sometimes referred as air modes)[175] in hBN that display low optical compression and remarkably long propagation lengths. Interestingly, these waveguide-like modes are also detected below the TO phonon frequency ($\approx 1390\ cm^{-1}$), and thus outside the Reststrahlen band, down to around $1350\ cm^{-1}$ (see Fig. 2.13). Note that while two modes can be distinguished clearly outside the Reststrahlen band, the higher momentum mode of the two closely overlaps in momentum space with the Edge-1 mode within the Reststrahlen band, making their distinction challenging. However, we note that L_p and Q as a function of frequency for the edge-1 and 0' modes show a sharp discontinuity in correspondence of hBN phonon mode at $1390\ cm^{-1}$, which we leveraged to classify those 2 modes.

The analysis of hyperbolic polaritons in large, isotopically enriched hBN flakes (up to 250 μm), free of macroscopic defects, with wide scan (40 μm) PTIR and s-SNOM maps enables precise ($0.05\ \mu m^{-1}$ resolution) quantification of the key characteristics, including: dispersion relation, propagation length, group velocity, lifetime, and figure of merit. Our results on ≈ 99 % ^{10}B hBN shows an eight-fold improvement of polariton propagation lengths (up to ≈ 25 μm) and a four-fold improvement in lifetimes (up to ≈ 4.2 ps) with respect to naturally abundant samples and record-breaking propagating figure of merit ($Q \approx 90$) matching earlier theoretical predictions. These results confirm the hypothesis that previous s-SNOM measurements of the polariton

lifetimes and propagation lengths on these samples were, in part, artificially restricted by the flake width – a critical issue for vdW polaritons with long propagation. With lifetimes close to theoretically predicted values, our analysis confirms the dominant role of isotopic disorder over other decay channels (anharmonic decay and background impurities), in determining the lifetimes of optic phonons in hBN. Therefore, further improvements shall be expected only for isotopically purest samples with even lower background impurities. The analysis and methods presented here can be generally applied to other vdW crystals and their heterostructures to benchmark polariton performance for a variety of nanophotonic applications. Particularly, we show that the period of the measured polariton fringes in near-field maps is affected by the light incident angles with respect to the sample plane (α) and with respect to the flake edges (β). These angles shall be accounted for when comparing measurements obtained with different measurement schemes or on flakes with edges illuminated from different angles. Even more importantly, we show that to extract accurate lifetimes and propagation lengths, large scan lengths ($\gg$ propagation length and in plane incident wavelength) on large flakes that are free of other defects or asperities (which also can launch the polaritons) are necessary. Overall, the extremely long propagation lengths of the polaritons studied here and the material growth-based strategy will enable progress in the development of nanophotonic materials and devices towards for use in hyperlensing and ultra-thin optics applications.

CHAPTER 3

Nanophotonics in Lower Symmetry Crystals

3.1 Impact of Crystal Symmetry on Nanophotonics

The initial works exploring HPhPs in hBN made it clear that natural crystal anisotropy offers a valuable tool for advancing nanophotonic control. Beyond the initial discovery in hBN, almost any uniaxial crystal will have an offset, though perhaps smaller, between the optic phonons along the opposing axes which will enable a region of HPhPs. This includes a significant number of vdW crystals, as well as bulk crystals like Quartz and Calcite, which also offer control over the crystal cut to manipulate the orientation of the optic axis with respect to the surface, enabling added control over the polaritonic behavior.

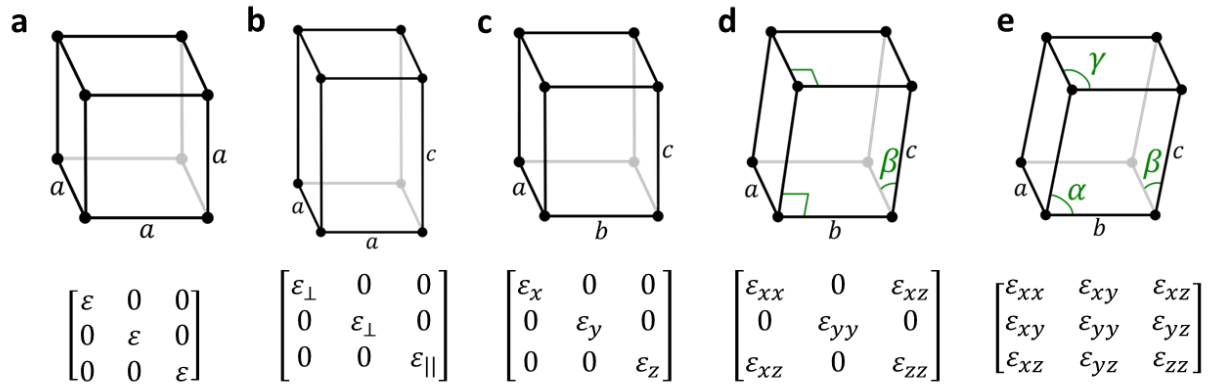

Figure 3.1 *Crystal structures and resulting permittivity tensors for a) cubic, b) tetragonal, trigonal, hexagonal, c) orthorhombic, d) monoclinic, and e) triclinic crystal systems.*

We can also explore natural crystals with further reduced symmetry and gain even greater control over the nanophotonic behavior. By comparing the symmetries of different crystal systems, and the resultant permittivity tensors, a path becomes clear which we have already

begun to walk down. Isotropic polaritonic media, which are by far the most common for nanophotonic applications since they include noble metals and plasmonic materials, as well as phonon polaritons in cubic crystals (Fig. 3.1a) like SiC. Uniaxial crystals, including tetragonal, trigonal, and hexagonal crystal structures (Fig. 3.1b), meet the fundamental requirements for hyperbolic polaritons due to the unique permittivity (and optic phonon frequencies) in one axis. The next step in decreasing symmetry would be biaxial, orthorhombic systems (Fig. 3.1c), where

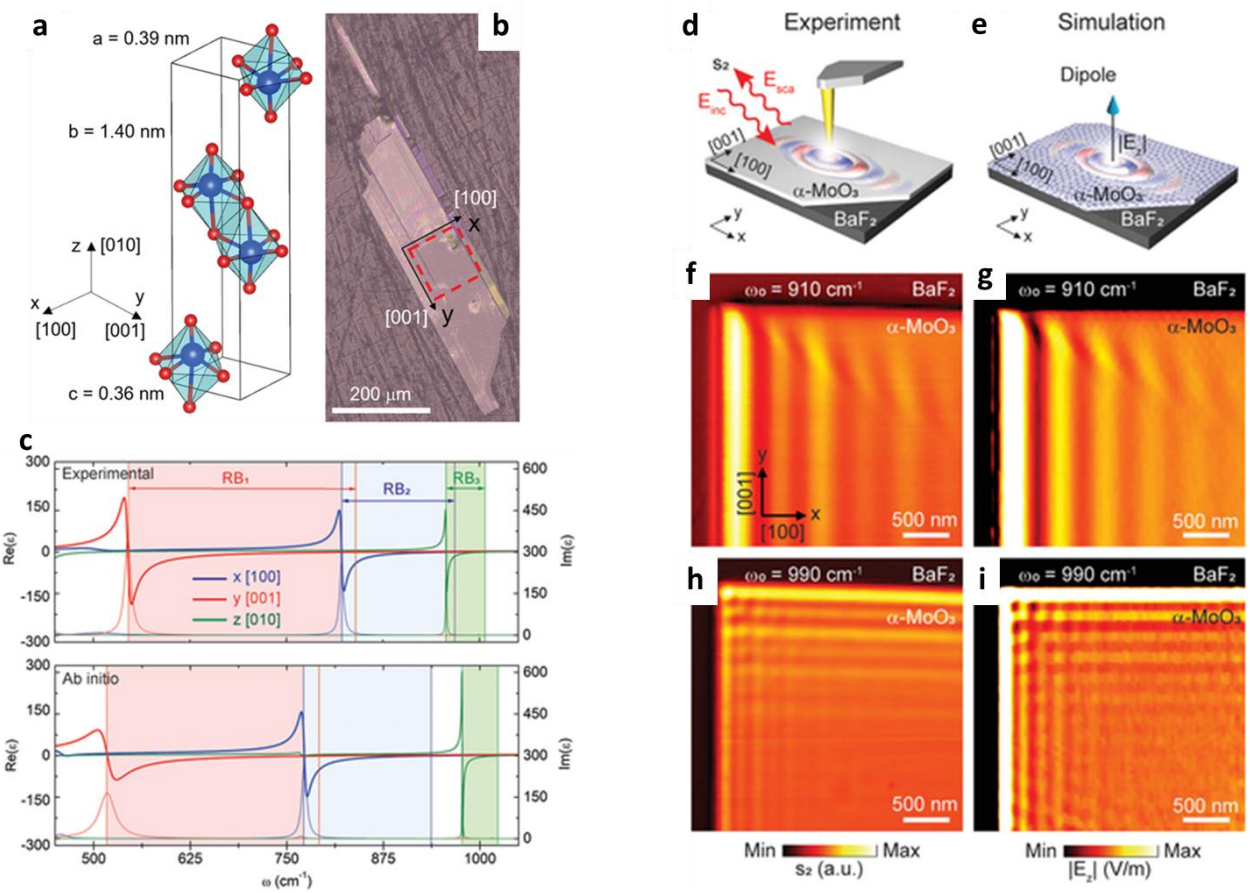

Figure 3.2 *MoO3 dielectric function and hyperbolic polaritons. a) Orthorhombic structure of MoO_3. b) Microscope image of MoO3 crystal, with outlined area measured in FTIR microscope for dielectric function. c) Dielectric function of MoO3 extracted from FTIR measurements and from ab initio theory. d-e) Schematic of polaritons launching from a s-SNOM tip and from a simulated dipole. f-g) In-plane hyperbolic phonon polaritons imaged in s-SNOM (f) and in COMSOL simulation using the experimentally extracted dielectric function. h-i) Elliptical phonon polaritons imaged in s-SNOM and COMSOL simulation. [from ref.* [182]*]*

all three principal axes offer unique lattice constant and thus permittivity. One exemplary material which has been recently demonstrated is MoO_3.

Similar to hBN, MoO_3 hosts hyperbolic polaritons – however, rather than being hyperbolic out-of-plane and propagating radially in-plane, MoO_3 also hosts polaritons which are hyperbolic in-plane[43,183]. This isolates the propagation to a single crystal axis in-plane, enabling a new level of control over the propagation. We used FTIR microscopy to experimentally extract the dielectric function of MoO3 crystals (Fig. 3.2c), which was unknown in the IR due to inherent difficulties with vdW crystal size scales. This dielectric function provided excellent agreement for simulating the in-plane hyperbolic and elliptical phonon polaritons (Fig. 3.2d-i), and established the groundwork for numerous recent works exploiting the in-plane hyperbolicity for exotic nanophotonic applications, including numerous works have shown that by overlapping 2 slabs of MoO_3 with varying offset angles, the propagation can be further controlled, and the optical axis (propagation direction) can be manipulated[184,185].

Moving past orthorhombic systems to monoclinic and triclinic systems reduces the symmetry even further. However, rather than increasing anisotropy in the diagonal permittivities as the previous crystal systems have done, these systems break the orthogonality of lattice vectors, resulting in non-zero off-diagonal permittivities. Given the trends in phonon polaritons which have offered increased nanophotonic control with decreasing crystal symmetry, we are confident that monoclinic and triclinic crystals should offer new and interesting control over the phonon polaritons, however there had not been any substantial studies of polaritons in these systems. In this chapter, we delve into the nanophotonic properties of monoclinic crystals, and particularly

β-Ga_2O_3 (bGO).

3.2 Hyperbolic shear polaritons in low-symmetry crystals

The lattice symmetry of a crystal is one of the most important factors in determining its physical properties. Particularly, low-symmetry crystals offer powerful opportunities to control light propagation, polarization and phase[43,185–187]. Materials featuring extreme optical anisotropy can support a hyperbolic response, enabling coupled light-matter interactions, also known as polaritons, with highly directional propagation and compression of light to deeply sub-wavelength scales[27,145]. Here we show that monoclinic crystals can support hyperbolic shear polaritons, a new polariton class arising in the mid- to far-infrared due to shear dissipation in the dielectric response. This feature emerges in materials where the dielectric tensor cannot be diagonalized, that is, in low-symmetry monoclinic and triclinic crystals where multiple oscillators with non-orthogonal relative orientations contribute to the optical response[188,189]. Hyperbolic shear polaritons complement previous observations of hyperbolic phonon polaritons in orthorhombic[43,186,187] and hexagonal[45,64,75] crystal systems, unveiling new features, such as the continuous evolution of their propagation direction with frequency, tilted wavefronts and asymmetric responses. The interplay between diagonal loss and off-diagonal shear dissipation in the dielectric response of these materials has implications for new forms of non-Hermitian and topological photonic states. We anticipate that our results will motivate new directions for polariton physics in low-symmetry materials, which include geological minerals[190], many common oxides[191,192] and organic crystals[193], significantly expanding the material base and extending design opportunities for compact photonic devices.

Crystal symmetry plays a critical role in dictating the optical, electronic, mechanical, and

thermal properties of a material. Reduced symmetry is at the heart of numerous emergent phenomena, including structural phase transitions[191], charge density waves[194,195] and topological physics[196]. The interaction of light with low-symmetry materials is particularly important, as it allows fine control over the phase, propagation direction and polarization[43,185–187]**.** This control can be especially pronounced for sub-diffractional surface waves, for instance surface phonon polaritons (SPhPs)[32,88] and surface plasmon polaritons (SPPs), supported at the surface of polar crystals and conductors, respectively. Both SPhPs and SPPs are quasi-particles comprised of photons and coherently oscillating charges, i.e., polar lattice vibrations or free-carrier plasmas, respectively, and they are strongly influenced by crystal symmetry. As a relevant example, low-symmetry polaritonic materials can support hyperbolic light propagation[63], constituting an exotic class of light waves that are highly directional with very large momenta. Hyperbolic polaritons arise in materials where the real part of the permittivity along at least one crystal direction is negative, while positive along at least one other, stemming from the extreme anisotropy of their response that is typically associated with specific polarized lattice resonances. In turn, hyperbolic polaritons enable deeply subwavelength light confinement over broad bandwidths[45,64,75]. In polar crystals with symmetries that support a single optical axis (uniaxial), such as hexagonal boron nitride (hBN), hyperbolic polaritons (HPs) of type I or II can arise[45,64,75,145], for which the hyperbolic isofrequency surfaces do or do not intersect the optical axis, respectively. Materials or metamaterials exhibiting lower symmetry, where all three major polarizability axes are different (biaxial) but orthogonal, such as alpha-phase molybdenum trioxide (α-MoO_3)[186,197], Li-intercalated V_2O_5[187], or nanostructured metasurfaces[79], exhibit several distinct spectral regimes of hyperbolic modes propagating along different crystal axes. Notably, in-plane hyperbolicity within α-MoO_3 films has been shown to be low-loss[186,197], with

reconfigurable features[198] and capable of supporting topological transitions[185]. Even more exotic polaritonic responses may be expected in crystals with further reduced symmetry, such as monoclinic and triclinic lattices.

Monoclinic crystals make up the largest crystal system, with approximately one third of Earth's minerals belonging to one of its three classes[199]. These low-symmetry Bravais lattices exhibit non-orthogonal principal crystal axes (Fig. 3.3a), in contrast to orthorhombic (e.g. biaxial α-MoO_3[43]), tetragonal, hexagonal, trigonal (e.g. uniaxial α-Quartz, aQ, Fig. 3.3b), or cubic crystal systems. As a consequence, their dielectric permittivity tensor has major polarizability directions that strongly depend on the frequency, with off-diagonal terms that cannot be completely removed through coordinate rotation[188,189]. These features arise due to the non-trivial relative orientation (neither parallel nor orthogonal) of multiple optical transitions that, at a given frequency, contribute to a net polarization that cannot be aligned with the crystal axes. In turn, this property results in exotic light propagation not supported by higher-symmetry crystals[188,189,200–202]. Here we show exemplary consequences of these material features for nanophotonics, in particular the emergence of a new form of waves - hyperbolic shear polaritons (HShPs) - which have not been previously observed.

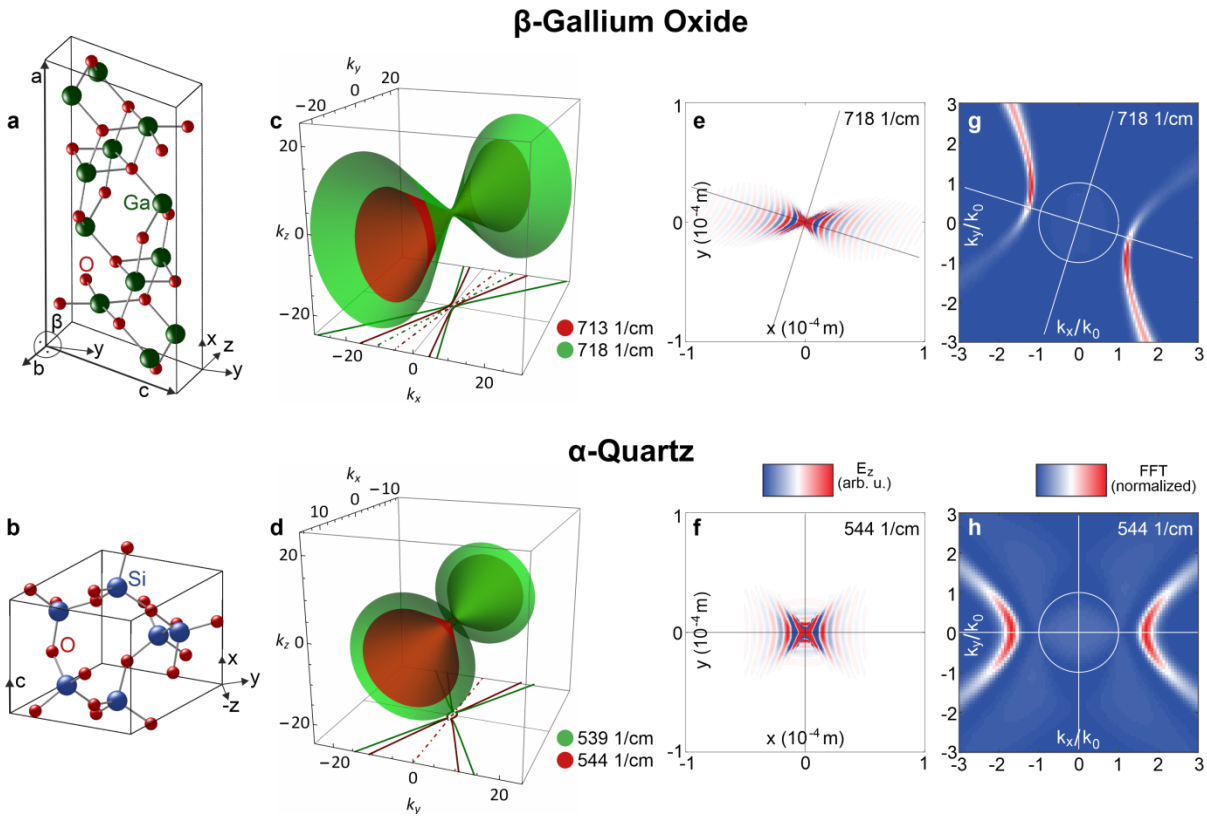

Figure 3.3 *Hyperbolic shear polaritons in monoclinic β-gallium oxide (bGO) compared to hyperbolic polaritons in uniaxial α-quartz (aQ). (a) Monoclinic crystal structure of bGO (monoclinic angle $\beta = 103.7°$). The sample surface of the investigated bGO crystal is the monoclinic (010) plane (x-y-plane) (b) Rhombic unit cell of aQ with the c-axis oriented along the x-direction, lying in the sample surface plane. The Cartesian coordinate system used in this work is shown. (c,d) Isofrequency surfaces for bGO and aQ, respectively, at two frequencies (red and green) where the material supports hyperbolic polaritons. The contour lines at $k_z = 0$ are plotted as solid lines at the bottom, and their mirror axes are shown as dash-dotted lines. (e,f) Real-space electric fields at the bGO and aQ surface, respectively, and (g,h) the respective two-dimensional Fourier transformation. Lines indicate the frequency dependent optical axes for bGO and the crystal axes for aQ. The fields were calculated using COMSOL Multiphysics*[314] .

In this work, we theoretically and experimentally demonstrate the emergence of HShPs in monoclinic crystals. HShPs arise in low-symmetry materials because of the presence of multiple phonon oscillators with non-orthogonal relative orientations. The resulting non-diagonalizable dielectric tensor exhibits shear dissipation terms analogous to viscous flow[203], which, when strongly coupled to light, enables the emergence of HShPs - a new form of HPs. As an exemplary material to demonstrate this phenomenon, we study beta-phase Ga_2O_3 (bGO), which

has gained significant research and industrial attention for its high breakdown field[204,205] and applications in photovoltaics[206], optical displays[207] and gas sensors[208]. In the low energy range, bGO features several strong IR-active, non-orthogonal phonon resonances[188], making the permittivity tensor of bGO naturally non-diagonalizable. Its low-symmetry has two consequences on the polariton propagation when compared to more conventional hyperbolic materials with a diagonal permittivity tensor such as hBN, aQ, and α-MoO_3. First, both the bGO polariton *wavelength* and propagation *direction* strongly disperse with frequency. Second, we demonstrate that the asymmetric nature of optical loss in such crystals gives rise to shear, resulting in polariton propagation with tilted wave fronts. Such tilted wave fronts are a direct consequence of the low symmetry of the material and are one of the most significant and unique features of HShPs. New opportunities for polaritonics arise for HShPs stemming directly from their non-Hermitian and topological nature. Yet, quite surprisingly, they can be observed in low-loss, naturally occurring materials, without the need for artificial structuring of a material surface[79].

To highlight the role of the asymmetry of monoclinic crystals in their polariton response, we compare HShPs with HPs supported by higher-symmetry anisotropic crystals, such as aQ[209]. In this vein, we compare the crystal structure of monoclinic bGO in Fig 3.3a with the trigonal crystal of aQ in Fig. 3.3b, illustrating the non-perpendicular crystal axes present in bGO. In general, the description of the dielectric response of monoclinic crystals requires inclusion of off-diagonal elements in the monoclinic plane within the frequency-dependent, complex-valued dielectric tensor

$$\overline{\overline{\varepsilon(\omega)}} = \begin{bmatrix} \varepsilon_{xx}(\omega) & \varepsilon_{xy}(\omega) & 0 \\ \varepsilon_{xy}(\omega) & \varepsilon_{yy}(\omega) & 0 \\ 0 & 0 & \varepsilon_{zz}(\omega) \end{bmatrix}. \quad (3.1)$$

Due to reciprocity, the off-diagonal elements are identical. The coordinate systems employed to define the response of bGO and aQ are sketched in Fig. 3.3a and b, respectively. To analyze the properties of HShPs in monoclinic materials, we first rigorously solve Maxwell's equations (see methods) to calculate the dispersion relation of the polaritonic modes supported by bGO and – for comparison – aQ, each at two distinct frequencies. Initially, we consider the lossless case, in which the imaginary part of each term in the dielectric tensor is neglected for both bGO and aQ. The solutions for the polariton wavevectors in both materials at two different frequencies are provided in Fig. 3.3c and d. For aQ, we observe two open hyperboloid surfaces – as expected for uniaxial hyperbolic materials – where a change in frequency results in a corresponding change in wavevector, while preserving the hyperboloid orientation, i.e., the direction of polariton propagation (Fig. 3.3d). In contrast, as we change the frequency, not only does the bGO polariton wavevector magnitude change, but the direction of the hyperboloid also rotates within the monoclinic plane, as can be appreciated by examining the k_z=0 projections (Fig. 3.3c, bottom). This is a direct consequence of the non-trivial relative orientation of the phonon resonances supporting the hyperbolic response[188], which results in polariton bands that disperse in azimuth angle as a function of frequency. This feature represents a signature of the reduced symmetry associated with HShPs supported in monoclinic crystals (and is also anticipated in triclinic crystals), in contrast to HPs observed in higher symmetry lattices.

When we also account for natural material losses resulting from inherent phonon scattering processes, the polariton propagation in bGO displays a reduced symmetry in comparison to

hyperbolic polaritons in aQ, even at individual frequencies, as illustrated in Fig. 3.3e and f. In these panels, we show the results of full-wave calculations of light propagating across the surface of a semi-infinite slab of bGO and y-cut aQ, where in both cases natural material losses were explicitly considered. The surface waves are launched by a point dipole placed just above the material surface. For in-plane hyperbolic materials, these surface waves are referred to as hyperbolic surface polaritons or hyperbolic Dyakonov polaritons[210,211], and constitute a subset of HPs supported in these materials similar to volume-confined HPs in thin films. At an isotropic-hyperbolic material interface, HPs display a hyperbolic dispersion within the surface plane, and have been analytically studied for uniaxial and biaxial materials previously[211–214]. For aQ, HPs spread out along one crystal axis of the surface, and are symmetric with respect to the crystal axes, as it can be confirmed by a Fourier transform of the real-space electric field profile (Fig. 3.3h). However, for bGO in Fig. 3.3e we observe that HPs are rotated with respect to the coordinate system of the monoclinic plane, as anticipated by the isofrequency contours (Fig. 3.3c). In addition, the wavefronts are tilted with respect to the direction of energy flow, with no apparent mirror symmetry. This feature can also be clearly seen by examining the Fourier transform of the real-space profile (Fig. 3.3g), exhibiting a stronger intensity along one side of the hyperbola. These observations constitute the discovery of HShPs in low-symmetry crystals.

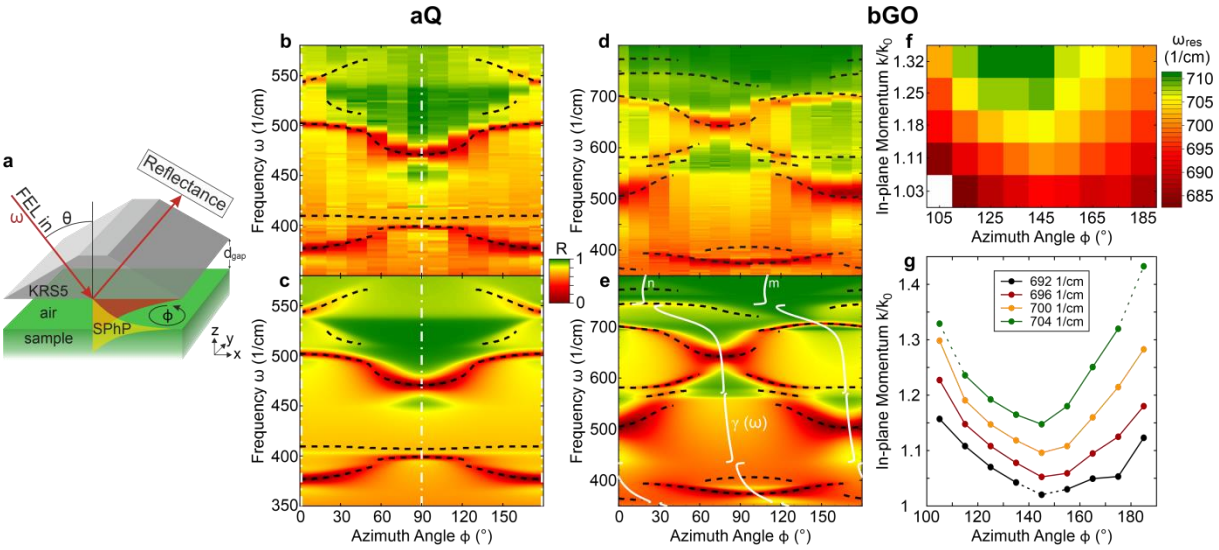

Figure 3.4 *Experimental observation of HPs on aQ and HShPs on bGO. (a) Otto-type prism coupling configuration for the experimental observation of surface waves. The p-polarized free-electron laser (FEL) excitation beam is reflected at the prism back side at an incident angle of* $\theta = 28°$*. The reflectance detection is unpolarized. The gap size was fixed to* $d_{gap} \approx 10.4\ \mu m$ *for aQ, and* $d_{gap} \approx 8.3\ \mu m$ *for bGO. (b) Experimental azimuth dependence of HPs on aQ, and (c) corresponding simulated reflectance map calculated by means of a transfer matrix method*[271]*. (d) Experimental azimuth dependence of HShPs on bGO, and (e) corresponding simulated reflectance map. The white lines in (e) correspond to the directions of the frequency-dependent major polarizability axes n and m, see text. (f) Polariton resonance frequency map for bGO in the 680-720* cm^{-1} *frequency range, extracted from Otto reflectance measurements at various incidence angles* θ *and azimuth angles* Φ *at constant gap size* $d_{gap} \approx 4.0\ \mu m$*. (g) In-plane hyperbolic dispersion for bGO at selected frequencies interpolated from (f). Dashed lines and symbols mark extrapolated values outside the accessed*

In order to experimentally demonstrate the effects of reduced symmetry in polariton propagation in bGO in contrast to higher-symmetry materials, we compare the dispersion of HShPs in bGO to the one of HPs in aQ using an Otto-type prism coupling geometry[35,215] (sketched in Fig. 3.4a). This method measures the spectral dependence of surface waves through sharp absorption peaks observed as dips in the reflectance spectra, by using a prism placed near the material surface. The crystals are oriented such that the monoclinic plane (bGO) and the optical axis (aQ) are

parallel to the sample surface. By following the spectral position of the polariton resonances as a function of azimuth angle, we probe the dispersion of hyperbolic waves at the surface for both bGO and aQ. The Otto geometry effectively selects a specific in-plane momentum component of those surface waves induced by the dipole excitation in Fig 3.3e and f, as set by the incidence angle θ and azimuth angle ϕ that define the magnitude[35,215] and direction of the selected momentum, respectively. The retrieved experimental dispersion of HPs on the surface of aQ is shown in Fig. 3.4b, in excellent agreement with the corresponding simulations (Fig. 3.4c). The dips in the measured reflectance spectra reveal the supported polariton modes, which are only observable along specific azimuth angles and are symmetric about the crystal axes, $\phi = 0°\ (180°)$ and $90°$. In contrast, the experimentally measured azimuthal dependence of HShPs on monoclinic bGO (Fig. 3.4d) is in excellent agreement with the simulated dispersion curves (Fig. 3.4e) and exhibits no mirror symmetry. To experimentally access the in-plane hyperbolic dispersion of the HShP in bGO observed in Fig. 3.3e, we mapped out the frequency-momentum dispersion in close spectral proximity of that mode (680-720 cm^{-1}) at many azimuth angles. The resulting map of polariton resonance frequencies is displayed in Fig. 3.4f. These data allow extraction of single-frequency in-plane dispersion curves as demonstrated in Fig. 3.4g for a number of selected frequencies, clearly showing a hyperbolic dispersion in excellent agreement with Fig. 3.3e.

The reduced symmetry observed within the polaritonic dispersion of bGO (Fig. 3.4d) is a direct consequence of the lack of symmetry in its vibrational structure[188]. Thus, the HShPs are not propagating along fixed axes, but display a continuous rotation of the HShP propagation direction as the frequency is varied. To describe the nature of this rotation, we diagonalize the real part of the permittivity tensor of bGO individually at each frequency. Since $\mathrm{Re}\left[\overline{\overline{\varepsilon(\omega)}}\right]$ is

Hermitian, we can diagonalize it, following the Spectral Theorem, by rotating the monoclinic plane by the frequency-dependent angle

$$\gamma(\omega) = \frac{1}{2} \arctan\left(\frac{2\,\mathrm{Re}(\varepsilon_{xy})(\omega)}{\mathrm{Re}(\varepsilon_{xx})(\omega) - \mathrm{Re}(\varepsilon_{yy})(\omega)}\right). \tag{3.2}$$

The dispersion of $\gamma(\omega)$ is shown in Fig. 3.4e (white lines), illustrating that the major polarizability directions within the monoclinic plane, denoted as *m* and *n*, widely vary across the spectrum. This frequency-dependent coordinate system enables an easier understanding of the polaritonic response, in particular a straightforward classification of dielectric, elliptical, as well as type I and II hyperbolic frequency ranges for the polariton dispersion. The rotated coordinate axes are shown in Fig. 3.3e and g, illustrating their alignment with the hyperbolic dispersion.

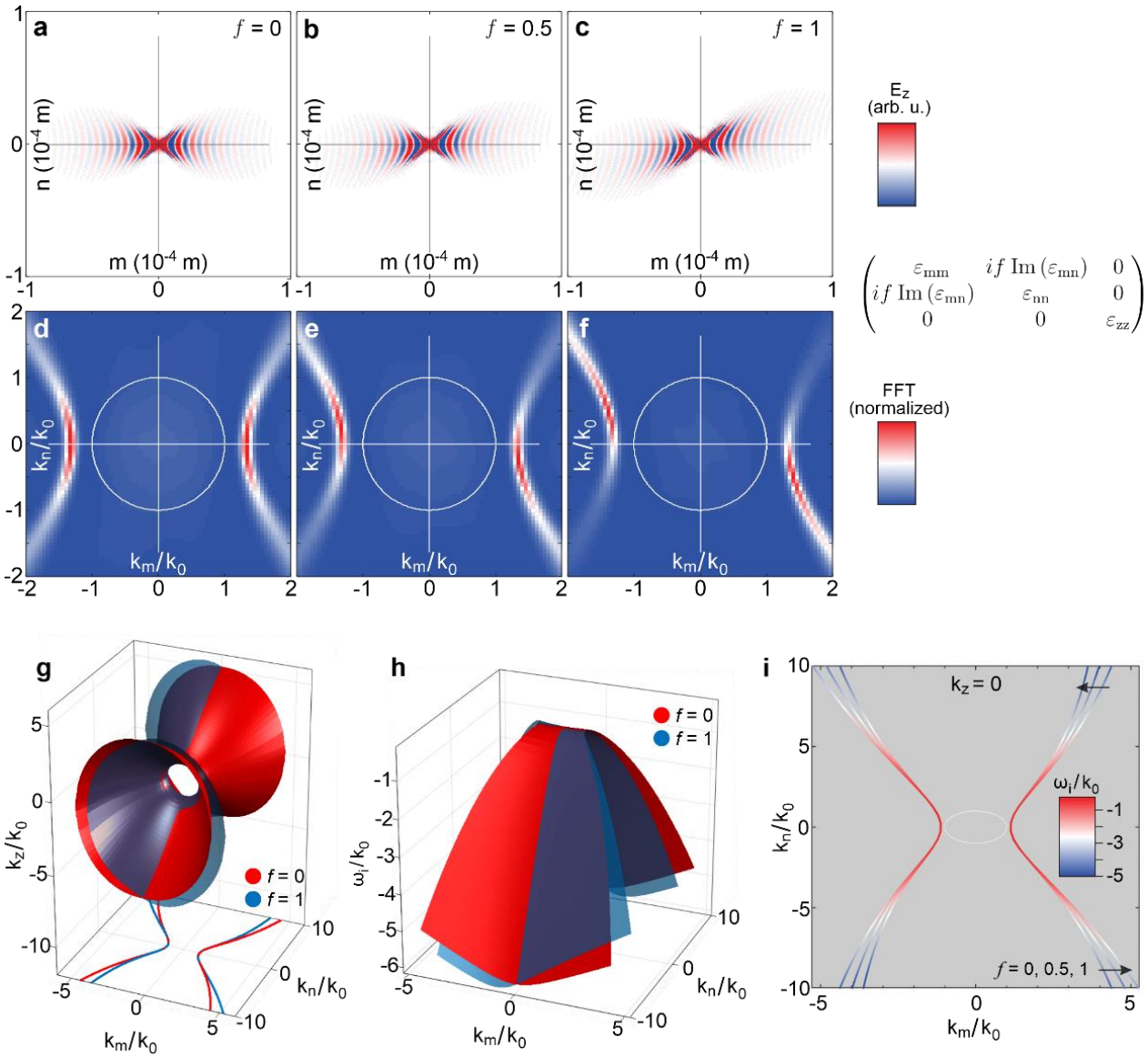

$$\begin{pmatrix} \varepsilon_{mm} & if\,\mathrm{Im}(\varepsilon_{mn}) & 0 \\ if\,\mathrm{Im}(\varepsilon_{mn}) & \varepsilon_{nn} & 0 \\ 0 & 0 & \varepsilon_{zz} \end{pmatrix}$$

Figure 3.5 *Symmetry breaking by shear dissipation for hyperbolic polaritons in monoclinic bGO. (a-c) Real-space electric fields at the bGO surface for three different magnitudes of the off-diagonal permittivity element* $i\,f\,Im(\varepsilon_{mn})$ *calculated in the frequency-dispersive rotated coordinate system at* $718\,cm^{-1}$*, and (d-f) respective Fourier transformation k-space maps in arbitrary units. The thin crosshairs indicate the principal axes in the frequency-dispersive rotated coordinate system, aligned horizontally and vertically because the maps were calculated within the rotated coordinate system [mnz]. (g) Isofrequency surface of bulk eigenmodes in bGO with complex frequency* $\tilde{\omega} = \omega/k_0 = 1 + i\,\omega_i/k_0$ *calculated in the rotated frame for* $f = 0, 1$ *(red and blue, respectively). (h) Imaginary part* ω_i *for* $f = 0, 1$*. (i) Contour lines of the isofrequency surface at* $k_z = 0$ *for* $f = 0, 0.5, 1$*. The imaginary part* ω_i *at the corresponding point in k-space is color-coded.*

Whilst the frequency variation of the propagation direction can be described by the coordinate

rotation in Eq. 3.2, such rotation does not capture the tilted wave fronts observed in Fig. 3.3e. This is because as we choose the rotated coordinate system [mnz] we still retain a purely imaginary off-diagonal permittivity component. These terms are associated with the non-orthogonal relative orientation of the material resonances, coupling the two crystal axes in the monoclinic plane. As a result, even in the rotated coordinate system [mnz], the dielectric tensor has off-diagonal terms associated with shear dissipation, linking different propagation directions purely through light absorption, analogous to the physics of viscous fluid flow[203].

To selectively probe the role of shear dissipation, we simulate the polariton propagation in the rotated coordinate system [mnz] at 718 1/cm. To highlight the role of shear, we include an arbitrary scaling factor for the magnitude of the off-diagonal imaginary component, indicated as $i * f\ \mathrm{Im}(\varepsilon_{\mathrm{mn}})$, with $f = 0$, 0.5, and 1 (shown in Fig. 3.5a-c), while retaining the diagonal loss terms. When we remove the off-diagonal component ($f = 0$), bGO essentially becomes a *shear-free* biaxial material, akin to α-MoO_3 and similar to uniaxial aQ, with polaritons propagating along the optical axes (Fig. 3.5a). Thus, while polariton propagation in such an fictional form of bGO is anisotropic in specific spectral ranges (similar to polaritons in MoO_3 [186,197]), mode propagation without shear dissipation is symmetric about the (frequency-dependent) major polarizability axes (Fig. 3.5a). As we gradually increase the magnitude of the off-diagonal loss term back to its natural value ($f = 1$), the wavefronts become increasingly skewed from the major polarizability axis (Fig. 3.5b,c). This behavior cannot be expected in higher-symmetry materials where polariton propagation is directed only along the principal crystal axes[186,187,197]. To extract the polariton dispersion from the real-space profiles (Fig. 3.5 a-c), we perform a 2D Fourier transformation for each of the modes, revealing strong symmetry breaking in the

intensity distribution within the isofrequency hyperbolae observed in the reciprocal space maps in Fig. 3.5d-f. This observation provides further evidence that the propagation of polaritons is non-trivial within low-symmetry monoclinic, and by extension triclinic, systems.

To connect the reduced symmetry of the surface subset of HShPs observed here experimentally (Fig. 3.4) and through our simulations (Fig. 3.5a-c) to the more general HShPs in the bulk, we now calculate isofrequency surfaces for polariton modes in bGO explicitly including loss, in order to account for the effect of shear dissipation. To this end, we solve Maxwell's equations for real momentum values, yielding complex frequency eigenvalues, whose imaginary part accounts for the finite lifetime of the supported mode.

The results of these calculations are shown in Fig. 3.5g-i. Here the real part of the eigen-frequency is fixed and we find its imaginary part ω_i (Fig. 3.5h) and the corresponding value of k_z (Fig. 3.5g) for each pair of k_m and k_n. We note that ω_i is proportional to the inverse of the modal lifetime $\tau \sim 2\pi/\omega_i c$, where c is the speed of light speed in vacuum. The lifetime in our example at 718 cm^{-1} is estimated as 0.22 ps near $k_n = 0$, consistent with experimental records in the literature[147]. The calculations are performed in the rotated coordinate system for both $f = 0$ and $f = 1$, showing that both the shape of the isofrequency surfaces, as well as their lifetimes, change significantly with the inclusion of the shear dissipation term in the off-diagonal imaginary components. Notably, these calculations prove that at individual frequencies and in the major polarizability frame, mirror symmetry of polariton propagation is lost in monoclinic materials as a direct consequence of the shear dissipation.

To relate the isofrequency contours of HShPs to the surface mode dispersions in Fig. 3.5d-f, we plot the $k_z = 0$ solution in Fig. 3.5i with the color scale indicating the relative loss ω_i of the

mode. Two important observations can be made: first, the mirror symmetry of the isofrequency curves is broken for $f > 0$ and it requires higher-order terms to account for the asymmetric shape; second, the mode losses are redistributed asymmetrically, with losses decreasing in one arm of the hyperbolae, while increasing on the other arm. This redistribution of loss is in excellent qualitative agreement with the point dipole simulations presented in Fig. 3.3 and suggests that the reduced/increased loss within the two arms of the hyperbolae contributes to the asymmetry in the intensity distributions in Fig. 3.5d-f. Interestingly, in this example we also observe an *increase* in propagation lengths as we increase f, despite the fact that the loss in the diagonal terms are kept constant. In this scenario, the additional shear dissipation induces an effective *reduction* of propagation losses, associated with the tilting of the eigen-vectors. We note that also in the experimental data, Fig. 3.4f,g, we see an indication of asymmetric distribution of polariton quality factors along the hyperbolic dispersion curves.

Interestingly, because of the asymmetry induced by the off-diagonal loss, we see a relationship where the maximum propagation lengths increase in proportion to the scaling factor f (Fig. 3.6). This is a unique contrast to conventional polariton propagation where imaginary permittivity (referred to as loss or absorption) results in decreased propagation lengths. It's likely that there is a balance between the increasing asymmetry (increasing propagation length in one direction) and the increasing absorption (decreasing propagation lengths in all directions) will balance out, but more work would need to be done to understand this.

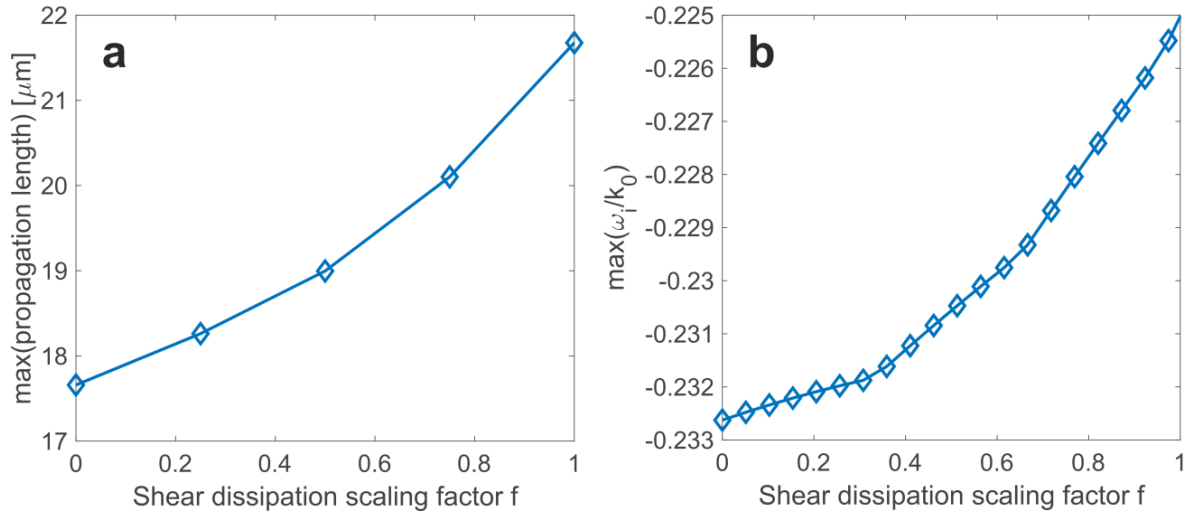

Figure 3.6 *Propagation losses as function of shear dissipation scaling. (a) Extracted propagation length from COMSOL field patterns for various values of the scaling factor f, see main text. The decay lengths of the surface waves were fitted for all azimuthal directions, and the maximum value was taken for each f. (b) Minimum loss $min(-\frac{\omega_i}{k_0})$ at $k_z = 0$ for analytical solutions of the complex frequency calculations as a function of the shear dissipation scaling factor f, compare Fig. 3i. Both calculations predict systematic reduction of propagation losses with increasing f, i.e. going from the artificial biaxial to the natural monoclinic bGO. All calculations were performed at* $718\ 1/cm$.

Another unique consequence of the off-diagonal contributions occurs when incorporating additional resonances into the material. Beyond the results provided here for intrinsic, undoped bGO, we also note that the presence of free charge carriers in bGO[216] – introduced either by impurity doping or transiently through photo doping – may allow for methods to modulate the major polarizability axes, enabling direct steering of the HShP propagation direction (Fig. 3.7).

These observations naturally link HShPs in monoclinic crystals to the rich emerging area of non-Hermitian and topological photonics. While loss in orthogonal systems alone can already have interesting consequences for polariton propagation[217], the off-diagonal shear dissipation highlighted here can provide new opportunities for non-Hermitian photonics and for manipulation of topological polaritons in low-symmetry materials. For instance, we envision asymmetric topological transitions experienced by HShPs, generalizing previous results in

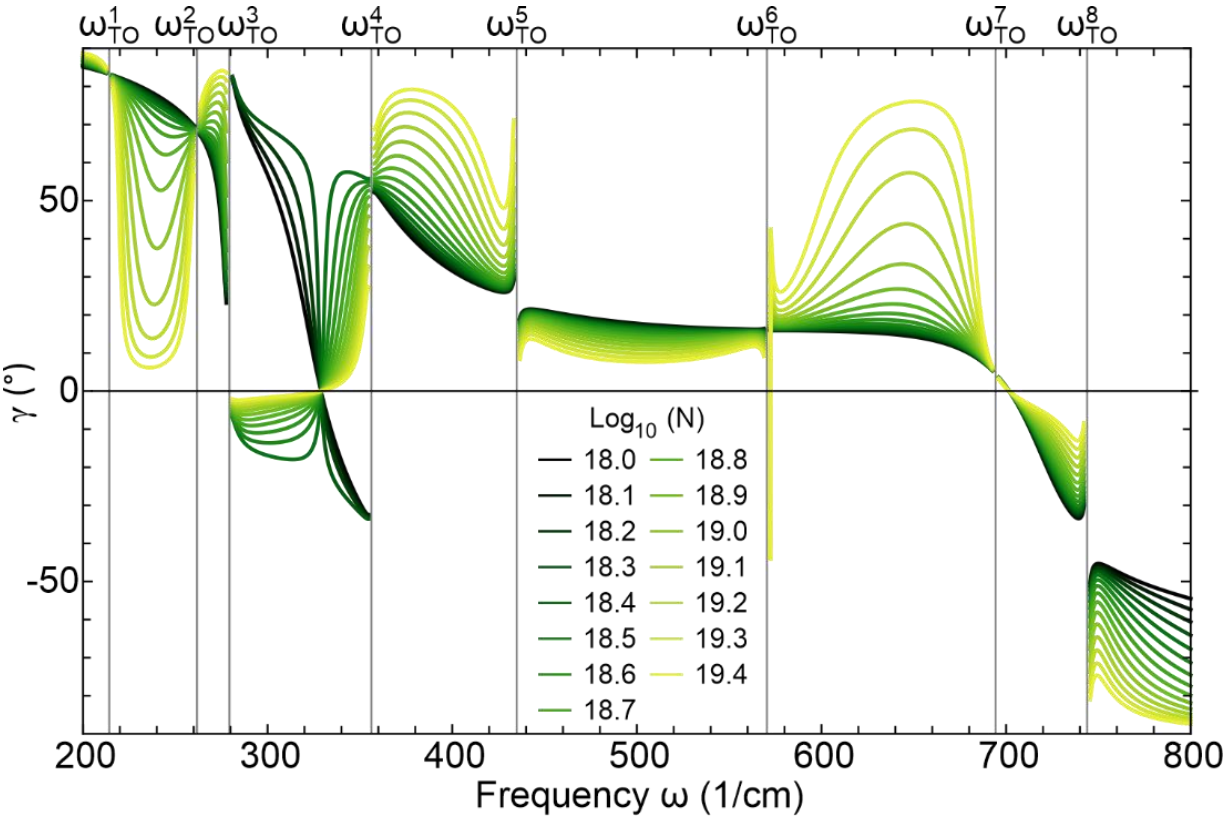

Figure 3.7 *Active tuning of the propagation direction of HShPs in bGO. Rotation angle γ (Eq. 2 of the main text) calculated as a function of doping concentration N (in cm^{-3}), assuming a Drude contribution with anisotropic charge carrier mobility, μ_x=296 $cm^2V^{-1}s^{-1}$, $\mu_y=\mu_z$=37 $cm^2V^{-1}s^{-1}$. (Literature values of μ in bGO feature a large variance*[315]*. We here assume strong anisotropy of the charge carrier mobility in order to emphasize the rotation mechanism.) Clearly, between the TO frequencies where the HShPs disperse, the rotation angle γ is strongly dependent on the doping concentration, enabling active tuning of the propagation direction of the supported polariton modes. Note that for an isotropic Drude contribution, on the other hand, Eq. 2 predicts no rotation of the propagation direction as a function of doping concentration.*

orthorhombic systems[185] by exploiting the unique non-Hermitian features emerging in low-symmetry materials. In addition, there have been recent studies suggesting the connection between Dyakonov surface waves and surface states emerging from one-dimensional band degeneracy (nodal lines) of topological nature of high-symmetry metacrystals[218]. We anticipate that HShPs may generalize these opportunities to asymmetric topological bands in which non-Hermiticity in the natural materials plays a dominant role.

In this work we have demonstrated that low-symmetry crystals can support a new class of hyperbolic polariton modes with their symmetry broken by shear phenomena, which we refer to as HShPs. We introduce bGO as an exemplary material to enable the observation of these phenomena, and experimentally demonstrate the symmetry-broken dispersion of the supported surface waves. The non-diagonalizable dielectric permittivity plays a key role in the unique properties of low-symmetry crystals including monoclinic and triclinic lattices. Our results are generalizable to engineered photonic systems with at least two non-orthogonal oscillators, including new metasurface designs capturing these physics. We anticipate that HShPs may have important implications in the manipulation of phase and directional energy transfer, including radiative heat transport[219,220], ultrafast asymmetric thermal dissipation in the near-field[220], and gate-tunability for on-chip all-optical circuitry[136,221]. Beyond advances in nanophotonics, infrared polariton propagation has been demonstrated as a means for quantifying crystal strain[83,222,223], polytypes[224,225], variations in free-carrier density, as well as phononic and electronic properties around defects[83] with nanoscale precision (< 20nm), thereby also promising a novel metrology tool for characterizing low-symmetry ultra-wide bandgap semiconductors. We highlight that our results are applicable to any material with non-orthogonal optically active transitions, and therefore may be extended to other optical phenomena, such as excitons in triclinic $ReSe_2$, which have recently been shown to support multiple in-plane selective excitons[226].

Finally, exfoliation of thin flakes of single-crystal bGO has also been recently reported[227]. Making use of volume confined HShPs in bGO will enable all the functionalities of uniaxial/biaxial hyperbolic systems, with the additional features unveiled by shear dissipation. As such, HShPs supported in low-symmetry semiconductors offer a broad scope for uncovering

and exploiting new types of light-matter waves and utilizing their properties in the mid- to far-infrared for an extensive range of applications, including on-chip photonics, light focusing, beam steering, and controlling thermal emissivity and radiation.

3.3 Controlling the Asymmetric Propagation of HShPs in bGO

In the previous section (3.2), we showed that the enhanced anisotropy and non-orthogonal structure of the monoclinic crystal β-Ga_2O_3 induce a remarkable rotation of the optical axis with frequency ("axial dispersion") associated to microscopic shear phenomena, resulting in hyperbolic polaritons that exhibit dramatic propagation asymmetry along axisymmetric polaritonic branches. However, the limitations of conventional laser sources in the mid- to far-infrared have so far precluded direct near-field observation of polariton propagation in real space for this monoclinic crystal. Here, we overcome these difficulties by employing a Free-Electron Laser (FEL) coupled to a scattering-type scanning near-field optical microscope (s-SNOM), providing direct imaging of the symmetry-broken propagation patterns of hyperbolic shear polariton in bGO. We also demonstrate how propagation asymmetry can be enhanced by momentum selection upon excitation. Our work paves a foundation for wide-spread utilization and device implementation of polaritons in low-symmetry crystals.

Crystalline structure largely defines the propagation of light in highly anisotropic materials, providing a means for controlling its behavior in conventional optical systems using polarizers, filters and waveplates. In the infrared spectral range, where photon frequencies overlap with lattice resonances, crystalline structure strongly affects light propagation, with optical phonons dominating the dielectric response of a material. In polar materials, Coulomb interactions break the degeneracy between transverse (TO) and longitudinal optical (LO) phonons, allowing the material to strongly couple with light. This coupling is responsible for the Reststrahlen band[228]

between the TO and LO phonon frequencies, within which light cannot propagate, and the material becomes highly reflective.

Under appropriate momentum-matching conditions, the optical phonons may couple to light to form phonon polaritons (PhPs) that behave similarly to plasmon polaritons in metals[27,32], albeit with much lower losses[32,46] and within a narrower spectral region. However, the inherent coupling of PhPs to lattice vibrations also enables a far greater degree of nanophotonic control in materials with lower crystal symmetry. This was first demonstrated in quartz[229] and hexagonal boron nitride[45,64], where the significant structural anisotropy between in- and out-of-plane crystal axes results in energetically offset optical phonons. This anisotropy gives rise to different spectral bands supporting hyperbolic phonon polaritons (HPhPs). These HPhPs are not confined to the interface, but they can propagate within the volume of the crystal at an angle defined by the open angle of the hyperbola[50], and support modes characterized by extremely large momentum, offering stronger light confinement, as well as increased control over the propagation direction, compared to conventional surface polaritons. The increased control offered by HPhPs has enabled applications such as hyperlensing[50,78,82,167], polariton refraction[66], waveguiding[66,230], and on-chip reconfigurable metasurfaces[66,80]. In orthorhombic lattices with even lower crystal symmetry, all three lattice constants may differ (while being orthogonal). In these biaxial materials, such as MoO_3, it has been shown that in-plane, in addition to out-of-plane hyperbolicity can be realized[43,69,231], enabling further control over polariton propagation[185], and even independent control over the wavevector and Poynting vector[232].

Recently, we extended this concept to crystals with even lower symmetry, such as monoclinic β-Ga_2O_3 (bGO), which not only exhibit three axes with distinct lattice constants, but also a non-orthogonality of the crystal basis in one lattice plane. The non-orthogonality between the axes of

monoclinic crystals results in significant off-diagonal elements in the dielectric permittivity in the monoclinic plane. As a result, in the presence of loss the permittivity tensor can no longer be diagonalized via real rotations. However, the real part of the permittivity tensor can be diagonalized by a frequency-dependent rotation in the monoclinic plane[29,188,189]. This rotation of the permittivity tensor represents a frequency dispersion of the major polarizability axes ("axial dispersion"), while a purely imaginary off-diagonal permittivity component – the shear term – is retained. We explored the polariton behavior in bGO by leveraging theory and prism-coupled measurements of the azimuthal polariton dispersion in this material[29]**.** Both theory and experiment demonstrate strong axial dispersion, as well as shear, measured as an asymmetry of the polariton quality factor about the rotated optical axes due to the off-diagonal loss in the rotated frame. As a result of these fundamental differences from traditional hyperbolic polaritons, these polaritons were dubbed 'Hyperbolic Shear Polaritons' (HShPs).

The unique properties of HShPs are highly promising for a range of nanophotonic applications as they offer a new degree of control over light propagation. On the one hand, slight changes in the incident frequency result in a dispersion in both the HShP wavelength and propagation direction. On the other hand, the shear effect leads to a symmetry breaking of the near-field propagation. With appropriate schemes, this symmetry breaking may be pushed to the extreme, where true single-directional light propagation is achieved in a natural material.

In this work, we experimentally map the unique propagation of HShPs in bGO in real space using scattering-type scanning near field microscopy (s-SNOM). As the excitation frequency is changed, we observe the rotation of the hyperbolic axis compared to the crystal axis. S-SNOM allows us to directly image the asymmetry in the shear polariton propagation. The broad range of momenta accessible by the s-SNOM experiment allows us to study in detail the momentum

dependence of the shear effect, specifically at large momenta. This regime was inaccessible in prism-coupling studies due to inherent limitations of the prism's refractive index[29]. Here, by using nano-antennas of different sizes coupling to different momentum components of the HShPs, we are able to experimentally demonstrate steeply increasing asymmetry with increasing HShPs momentum in agreement with theoretical predictions. Thus, we show that, conveniently, HShPs naturally provide the highest control over their propagation characteristics at the largest confinement conditions, ideally matching requirements for nanophotonic applications.

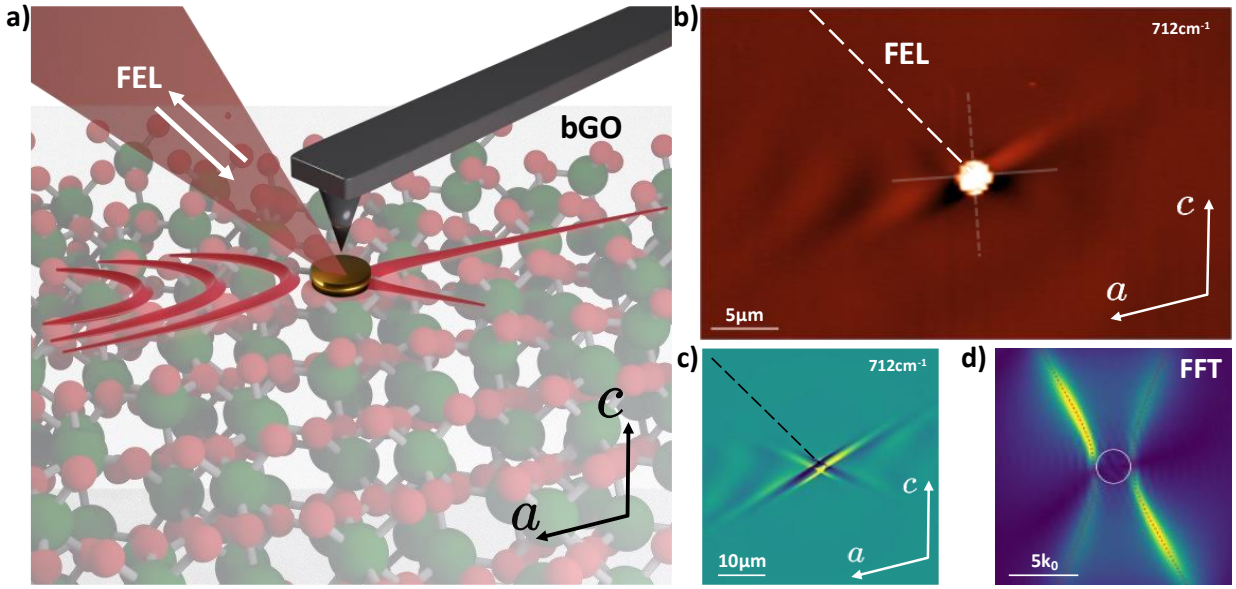

Figure 3.8 *Real-space imaging of HShPs launching from infrared antenna on the surface of bGO observed via FEL-coupled s-SNOM.* ***(a)*** *Schematic of FEL-coupled near-field imaging experiment.* ***(b)*** *Experimental near-field image of HShPs launched by a 2 μm gold disc by the incident FEL beam (oriented along the dashed white line) at a frequency of 712 cm^{-1}.* ***(c-d)*** *Finite element modeling of HShP launched by a 2 μm gold disc under similar launching conditions to the experiment shown in (b), in real-space (c) and Fourier space (d). Red dashed curves denote the dispersion of HShPs calculated from theory.*

To explore the shear propagation in real-space, we launch HShPs from gold disc antennas fabricated on the monoclinic surface of a bulk, [010]-face bGO crystal (Fig. 3.8a). These antennas allow us to launch HShPs along the surface of the bGO crystal, which we measure with s-SNOM. Due to the low energy of optical phonons in bGO (primarily ranging from ~200 cm^{-1}

to 750 cm^{-1}), commercial s-SNOM infrared sources are limited or nonexistent in this range. Instead, we leverage a broadly tunable, narrow linewidth free-electron laser (FEL). The FEL s-SNOM system offers a frequency range spanning the infrared to THz range (4-250 um)[233], allowing us to probe the full spectral range of HShPs supported in bGO.

In Fig. 3.8b we observe evident axial dispersion and shear asymmetry of HShPs in real-space propagation, characterized by strongly tilted wavefronts propagating at a skewed angle relative to the principal axes. In the experiment, the FEL is incident on the sample as shown by the white dashed line, at 45° off-normal. To the left of the 2 μm diameter gold disc, we observe an in-plane hyperbolic, tilted wavefront propagating at an angle rotated away from the [100] axis. To the right, rather than fringes of a hyperbolic propagation, we observe ray-like polaritons (similar to previous observations of so-called Ghost-polaritons in calcite[44]) propagating along one arm of the hyperbola (Fig. 3.8b). We note that these results are in excellent agreement with our numerical simulations shown in Fig. 3.8c-d, as well as the theoretical HShP dispersion relation (the red dashed curves in Fig. 3.8d). The Fourier analysis of the disc-launched simulations (Fig. 3.8d) shows a dramatic clockwise bias in intensity along one arm of the hyperbola due to the shear asymmetry.

For the numerical simulations, COMSOL version 6.0 was used for simulating both point dipole excitation and disc launcher excitation of shear polaritons at the interface of [010] **β-Ga_2O_3** and air. Scattering boundary conditions were used on the boundaries to absorb all outgoing radiation. The area of the interface between air and the bGO slab was (80×80) μm, such that shear polaritons are sufficiently damped when it reaches the boundary as not to influence the results.

For near field simulation, a point dipole source was placed 200 nm above the surface of the material. For disc-launcher simulations, a plane wave source with p-polarization and a fixed

incident angle of 45° is placed 6 μm above the interface. The gold disc launcher is 2 um in diameter and 100 nm in thickness. In far field simulations, to filter out the background due to plane wave illumination and reflection from the interface and extract the near field distribution of polaritons from disc launcher excitation, we performed twice the same simulation with and

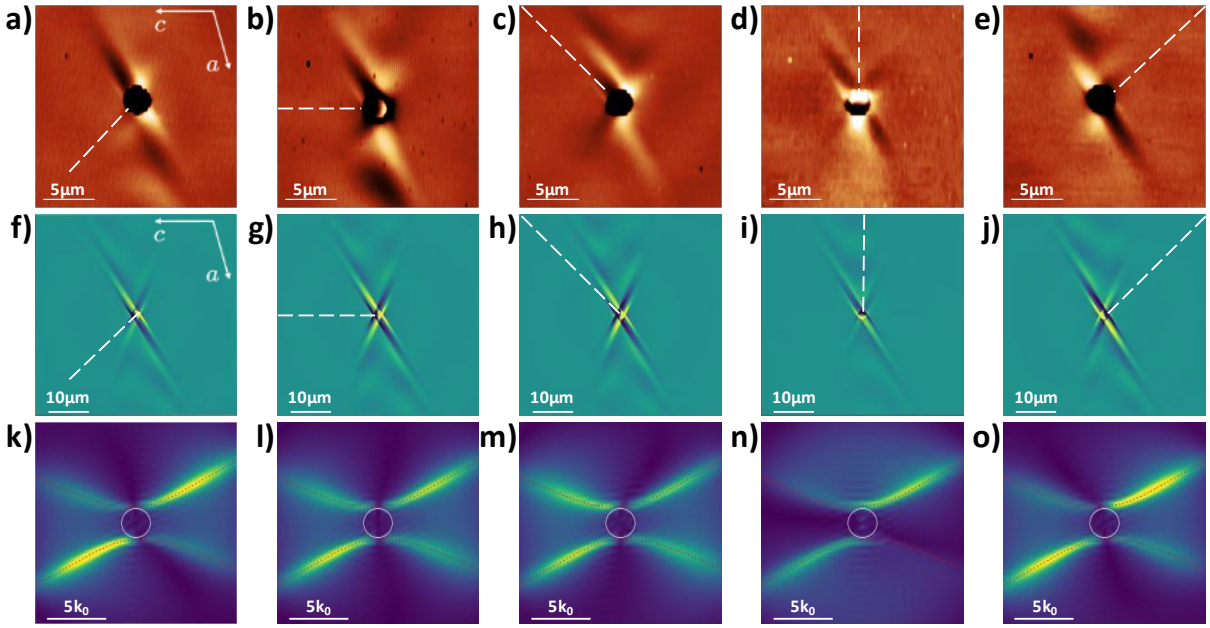

Figure 3.9 *Dependence on illumination orientation of HShPs in a bulk bGO crystal.* (a-e) *Experimental near-field images of HShP propagation, launched by a 2 μm gold disc at a frequency of 712 cm^{-1}, with FEL illumination rotated in 45-degree steps, as illustrated by white dashed line.* (f-j) *Finite element modeling of HShP propagation from gold disc, with illumination conditions similar to (a-e).* (k-o) *Fourier transforms of (f-j), illustrating the shear asymmetry in the polariton propagation. The red dashed curves in k-o are the dispersion of HshPs calculated from theory.*

without the presence of the disc launcher, respectively, and calculate the difference of fields in the two cases evaluated at 100 nm above the interface.

Due to the oblique illumination in s-SNOM experiments, there is an inherent degree of orientation dependence in experiments. In uniaxial crystals like hBN, this results in a slight change in the polariton wavelength and real-space image depending on the orientation of the

crystal edge with respect to the illumination[234]. Especially in crystals where the hyperbolic polariton axis is in-plane, the orientation dependence can be more important. In calcite it was shown that the fringe vs ray-like behavior of ghost polaritons depends on the orientation of illumination with respect to the hyperbolic axis[44]. As such, it is critical to determine that the asymmetric propagation observed is not an artifact induced by the oblique s-SNOM excitation.

In bGO, the frequency dispersion of the polarizability axes makes aligning the illumination to the polariton axes impossible for more than a single frequency. As such, we explore the orientation dependence of HShPs at a single frequency (712 cm^{-1}) by rotating the incidence direction of the incident laser with respect to the crystal axes (Fig. 3.9a-e). In these experimental images, it is clear that the FEL incidence direction affects the visibility of polariton fringes, as well as the propagation length and intensity of the ray-like modes yet does not dramatically modify the overall modal character. In Fig. 3.9a,c,e, the polariton propagation is clearly asymmetric horizontally across the antenna, with fringe-like propagation on one side, and ray-like behavior on the opposite side. Additionally, we see that after rotating by a full 180 degrees (Fig. 3.9a,e), the shear tilt of the propagating wave is clockwise in both orientations rather than mirrored across a symmetry axis – indicating the direction of shear is inherent to the crystal lattice and not to the incident direction. When the incident beam is aligned with the c-axis which coincides with one polarizability axis at this wavenumber, and therefore perpendicular to the propagation direction (Fig. 3.9b), fringes are clearly visible to both sides of the antenna. In the other case where the incident beam is nearly parallel to the propagation axis (Fig. 3.9d), no fringes are visible and instead ray-like modes with a clear yet less pronounced asymmetry (in comparison to Fig. 3.9a,e) are launching weakly along the hyperbolic arms.

The simulated field profiles with matching incidence orientations to the experiments (Fig. 3.9f-j)

show varying degrees of asymmetry across the launcher. The orientation-dependent asymmetry is clear in the Fourier space plots (Fig. 3.9k-o). The asymmetric effects in disc-launcher excitation origin from two mechanisms. The first contribution comes from the shear contribution to the permittivity tensor, causing the inherent asymmetry in polariton propagation, which can be best seen in near-field point-dipole excitation. The second mechanism is the orientation-dependent phase matching condition between the illuminated disc launcher and the excited polaritons. In fact, when the projected in-plane momentum of the source is aligned to one of the asymptotic lines of the hyperbola, HShPs in the corresponding arms are mostly excited. On the contrary, HShPs in other arms are less coupled with the source, causing the largest asymmetric excitation. As such, the asymmetry is strongest for incidence near the clockwise hyperbola arms (Fig. 3.9f,k,j,o) when the shear effect and the largest asymmetric excitation act on the same arm, maximizing the overall asymmetry. The asymmetry is reduced if the excitation is nearly along a polarizability axis (Fig. 3.9g,l), and weakest for excitation nearly along the counter-clockwise arm (Fig. 3.9h,m), because the shear effect acts on the clockwise hyperbola arm while the largest asymmetric excitation acts on the other arm. In Fig. 3.9i,n, the asymmetric excitation from phase matching condition is nearly diminished since the illumination direction is almost parallel to the major axis of the hyperbola and thus the source couples equally to the two arms. As a result, the shear effect solely contributes to the asymmetry, leading to a slightly less prominent asymmetry compared to the cases in Fig. 3.9f,j. Despite varying degrees of asymmetry observed here, HShP excitation is always biased clockwise, demonstrating that the shear effect is dominant compared to any illumination effects that break the symmetry of the polariton propagation. Moreover, the dependence of asymmetry on the illumination orientation also highlights that the phase matching mechanism is a crucial degree of control over the shear polariton propagation.

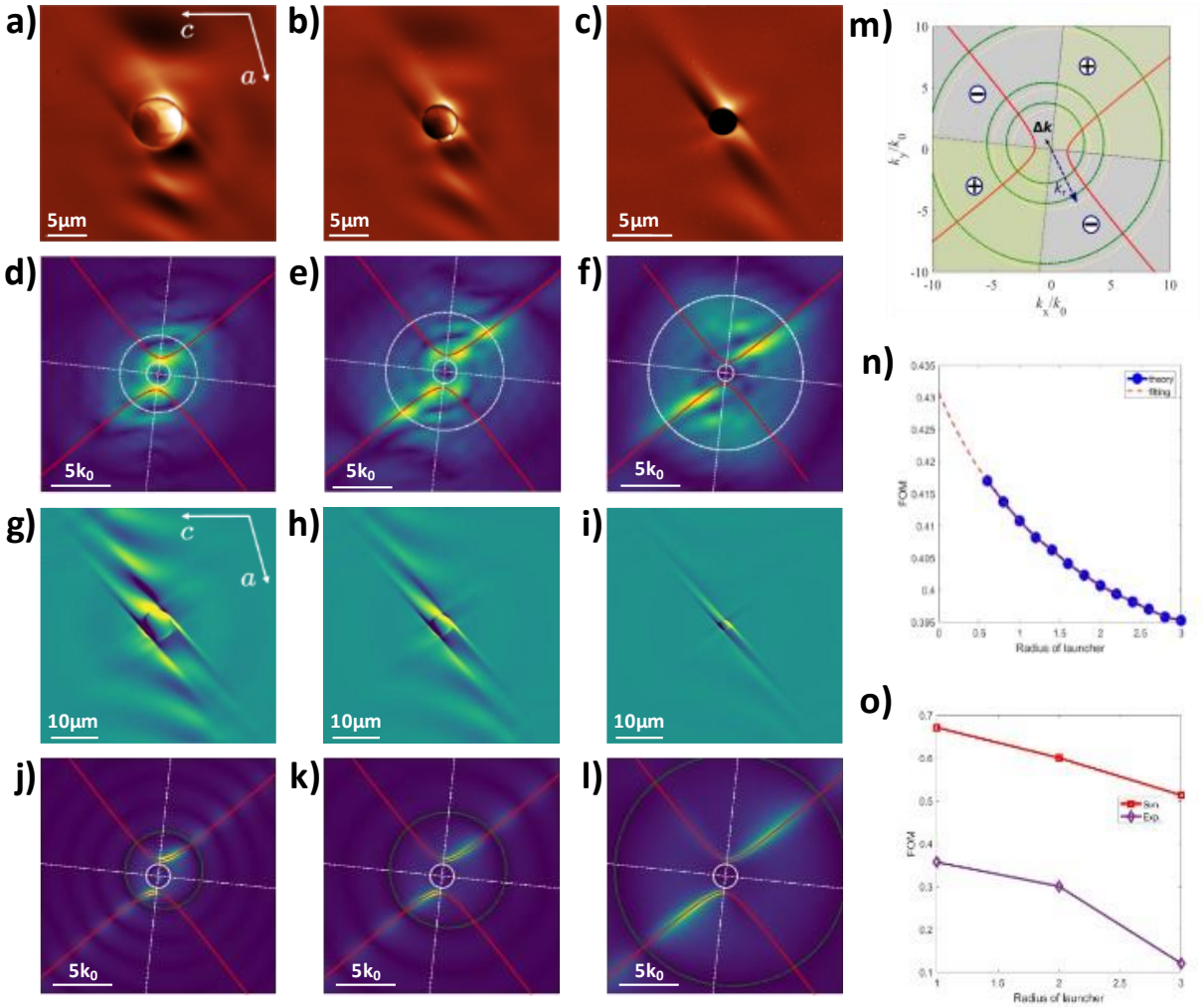

Figure 3.10 *Momentum dependence of HShPs computed analytically and probed by illuminating gold resonators of different size.* (a-c) *Experimental near-field images of HShP propagation, launched by a (6,4,2) µm gold disc at a frequency of 720 cm^{-1}, with illumination incident from the lower left corner.* (d-f) *Fourier transform of the experimental images in (a-c), with a zero-filling factor = 5. g-i) Finite element modeling of HShP propagation from gold discs to match experiment (a-c). j-l) Fourier transforms of (g-i). m) Schematic for extracting the HShP figure of merit (FOM) as a function of the launcher radius from the k-space dispersion. n) Analytical FOM dependence on the launcher radius – extracted by integrating the damping rate along the path of HShPs dispersion which is cut off in momentum determined by the launcher radius. o) Dependence of FOM on the launcher radius, extracted from Fourier transforms of the experimental and simulated field profiles (a-c, g-i).*

Our near-field experiments uniquely enable us to access polariton wavevectors that are much larger than the free space values. This is particularly interesting for HShPs, where theory predicts an increase of loss asymmetry with wavevector magnitude[29]. In our previous work, we were able to experimentally show such increasing shear through careful prism-coupled studies. However, the asymmetry was faint due to inherent limitations of the technique to low wavevectors. Here, we use gold disc antennas with varying sizes ranging from 2 to 6 μm diameter (Fig. 3.10a-c), which allows us to excite polaritons at extremely large wavevectors to study the momentum dependence of shear in the ultra-confined polariton regime.

Launched by a 6 μm diameter gold disc, HShPs propagate with tilted wavefronts from the bottom of the antenna (Fig. 3.10a), however, the ray-like mode is not clear. Around the disc we observe a radial fringe, as well. As the disc size decreases to 4 μm (Fig. 3.10b) and then 2 μm (Fig. 3.10c), the radial fringes become less prominent, and the ray-like modes become clearer. By taking a 2D Fast Fourier Transform (FFT) of the experimental images (Fig. 3.10d-f), we observe a clear progression towards a single strong branch of the hyperbolic dispersion – indicating that by launching at higher wavevectors, i.e. smaller disc size, the excited HShPs become not only increasingly directional and confined, but they are also effectively excited exclusively along one dispersion branch, further enhancing their directionality. Simulated field profiles and FFTs of the same sized gold discs (Fig. 3.10g-l) match well with experiment.

We can quantify the degree of shear in the polariton propagation based on complex-momentum eigenmode analysis to gain a more quantitative view of the momentum-dependence of HShPs [SI]. To do this, we perform a line integral of the damping rate $\gamma = \frac{q_i}{q_r}$ along the arm of the HShP hyperbola in each quadrant of the k-space dispersion (supplementary Fig. xx), and

compare the integrals following two arms of the hyperbola to get a figure of merit for the shear asymmetry (FOM_{Sh}):

$$\mathrm{FOM}_{Sh}(R) = \frac{\left|\sum_i (-1)^i \int_{k_i}^{k_R} dk\gamma\right|}{\sum_i \int_{k_i}^{k_R} dk\gamma}. \tag{3.3}$$

, where k_R is the cut-off radius in momentum space determined by the radius of the disc launcher, and k_i is the intersection of rotated hyperbola axis and hyperbolic dispersion in the according quadrant. Equation (3.3) allows us to calculate the FOM_{Sh} from the analytical description of HShPs by analyzing propagation losses of the shear polaritons and taking into account the wavevector shift due to the illumination angle of incidence. We see that the FOM_{Sh} obtained using (3.3) on γ obtained analytically, is inversely proportional to the launcher size, suggesting an increase of asymmetry with wavevector magnitude (Fig. 3.10n). However, we are also able to extract FOM_{Sh} from our direct measurement and simulation of the HShPs launched from the differently sized launchers by integrating over the intensities along the dispersion in the experimental and simulated FFT maps. We observe a similar relationship to the analytical case, but the change in the FOM_{Sh} with launcher size appears to be significantly larger in amplitude (Fig. 3o). This is consistent with what we analyzed in Fig. 3.9: two mechanisms contribute to the measured asymmetry upon launcher excitation, while the theoretical calculation only accounts for the shear effect of the HShPs, thus FOM_{Sh} from the simulation is expected to be larger than the one from theory. The inclusion of a s-SNOM tip in the experiment reduces oblique-incidence induced asymmetry, which also accounts for the change in magnitude of FOM_{Sh} between experiment and simulation, yet we observe a strong as well as strongly launcher-size dependent FOM_{Sh} also experimentally. From these results, we can quantitatively show that shear increases significantly with smaller disc size and, thus larger polariton momentum components excited, laying out a promising avenue for full symmetry

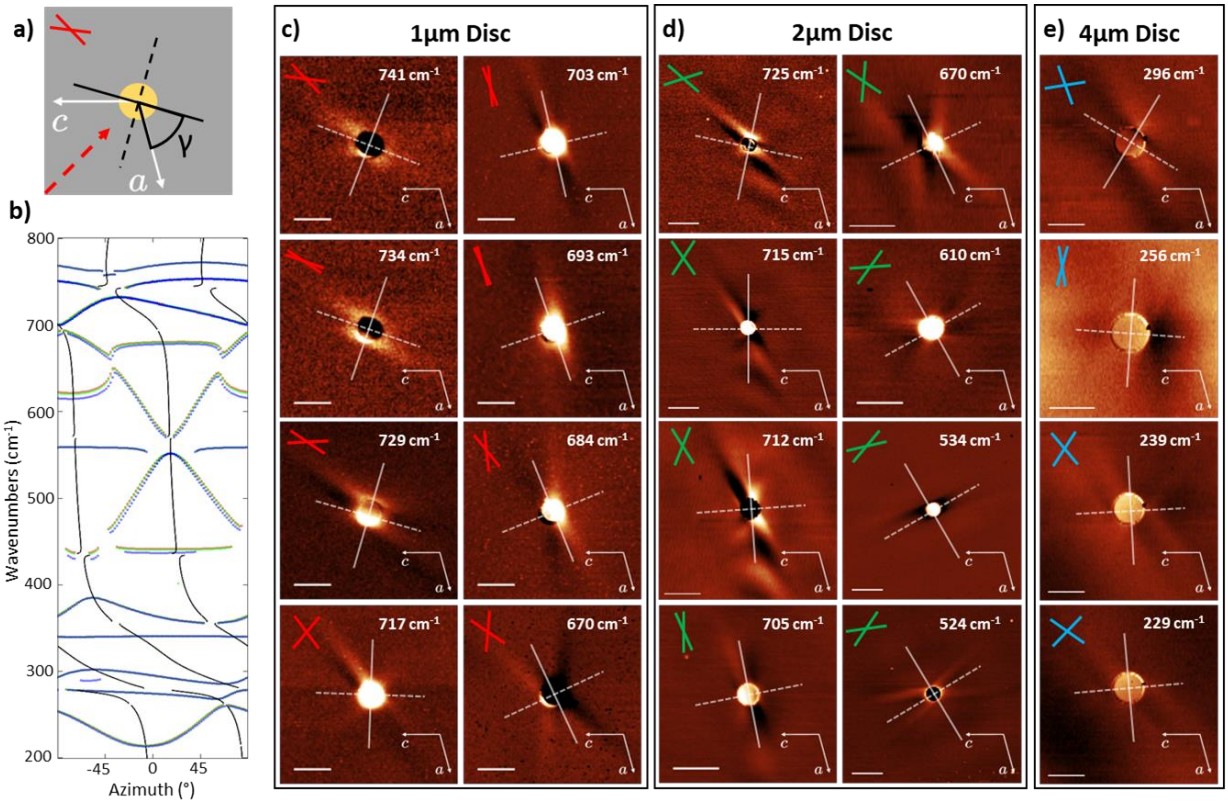

Figure 3.11 *Frequency dependent rotation of HShP propagation. a) Schematic of the frequency-dependent rotation of the polariton axis, with hyperbola arms in upper left. b) Plot of the permittivity rotation angle γ, with TMM calculation of the polariton peaks for the different gold disc sizes, marking the opening angle of the hyperbolic dispersion across the HShP range. Transparency of TMM calculations is given by the peak intensity of Im(rpp) divided by the maximum peak intensity for a given azimuthal angle. c-e) Rotated polariton axis plotted, as in (a), against c) Near-field images of HShPs launched by a 1 μm diameter gold disc, at varying frequencies (Scale bar = 2 μm). d) Near-field images of HShPs launched by a 2 μm diameter gold disc, at varying frequencies (Scale bar = 5 μm). e) Near-field images of HShPs launched by a 4 μm diameter gold disc, at varying frequencies (Scale bar = 5 μm). Upper left of c,d,e show the arms of the hyperbolic dispersion as extracted from b.*

control of strongly confined HShPs.

Aside from the shear asymmetry that we have explored thus far, HShPs are also defined by a strong rotation of the hyperbola axis with changing frequency that we refer to as axial dispersion[29]. To quantify this, we calculate the polarizability axes rotation angle γ (Fig. 3.11a) across the spectral range where HShPs are supported (Fig. 3.11b). To verify that the excited polaritons are HShPs at various frequencies, we provide disc-launcher simulations in the SI and

confirm their shear hyperbolic nature. We also plot the azimuthal dependence of polariton resonances at the corresponding wavevectors for 1,2, and 4 μm gold discs, providing an estimate of the expected opening angle of the hyperbola (azimuthal spacing of two resonances at each frequency in the upper left corner). These data can be compared to the experimental real-space polariton propagation that we acquired over a wide range of incident frequencies (Fig. 3.11c-e). We highlight that different sized disks are used to ensure efficient launching of polaritons over the wide range of frequencies studied, ensuring a similar range of k/k_0 shown. The propagation patterns align well with the frequency-dependent polariton axes (shown in white), while the propagating fringes (when visible) are tilted due to the shear. At different frequencies, we observe varying degrees of ray-like propagation vs tilted polariton fringes. This is due in part to the inherent dispersion of the polariton behavior and specifically to the frequency-dependent magnitude of the shear but is also affected by the interplay between axial dispersion and the fixed illumination orientation as discussed in Fig. 2. Our data clearly demonstrates that bGO supports sub-diffractional ($\sim\lambda_0/4$), strongly asymmetric directional polaritons with long propagation (>10 μm) across a wide spectral range in the far-infrared.

In conclusion, we have explored symmetry breaking at the nanoscale in the near-field propagation of hyperbolic shear polaritons in bGO. These results represent the first near-field measurements of the nano-scale real-space HShP propagation in bGO, exhibiting wide tunability of the propagation direction and a strong rotational asymmetry as a result of the monoclinic structure of the underlying crystal lattice and strong anisotropy in the phonon resonances, leading to giant microscopic shear effects. We have demonstrated that polaritons in monoclinic crystals offer significant control over polariton propagation via excitation frequency, illumination direction, and disc launcher size, exceeding that offered by higher symmetry polaritonic systems.

Furthermore, we theoretically and experimentally reveal a hidden synergy between shear, and hence extreme polaritonic directionality, with increasing HShP confinement. We believe that the exquisite control over the degree of symmetry-breaking offered by HShPs via shear and axial dispersion provides an avenue for enhanced efficiency of light-guiding at deeply sub-wavelength scales.

CHAPTER 4

Engineered Uniaxial Materials for Nanophotonics

4.1 Effective Anisotropy in Layered Materials

While the suite of natural materials offers a wide range of polaritons in varying spectral ranges and degrees of anisotropy, there is limited engineerability in such systems. If we instead consider the growth of thin films, whereby one can create a material with an engineered unit cell, we can see a path towards designed anisotropy in a stack of materials.

Periodic subwavelength structures, such as those described above, can be treated as a homogeneous uniaxial material, with the dielectric tensor described by effective medium theory[235]. In particular, for a periodic stack of thin films grown along the z-axis, the effective permittivities can be calculated as follows.

$$\varepsilon_{x,y}(\omega) = \sum_i f_i \, \varepsilon_i(\omega) \tag{4.1}$$

$$\varepsilon_z^{-1}(\omega) = \sum_i f_i \, \varepsilon_i^{-1}(\omega) \tag{4.2}$$

Where f_i is the filling fraction of the layer within the unit cell. In principle this can be done with an arbitrary number of layers (so long as the period remains subwavelength). In practice, such structures are commonly used for hyperbolic metamaterials[63] (HMMs), consisting of alternating metal and dielectric layers. These HMMs were the first forays into anisotropic nanophotonics – and provided much of the groundwork for the phonon polariton work described in this dissertation.

Initial efforts with metal-dielectric HMMs were able to achieve a number of exciting nanophotonic behaviors, including negative refraction[152,236–238], subwavelength focusing[76,239–242], and controlled spontaneous emission[243–248]. However, the heavy losses from metal plasmons present a significant limitation. Efforts to mitigate the losses have shown some successes, using lower loss doped semiconductors such as InAs[249,250] and CdO[251] have achieved high quality factor, broadly tunable hyperbolic polaritons.

In order to fully minimize losses, we can use the HMM concept, and replace the metal layer with the optically metallic Reststrahlen band of a polar semiconductor. In such a structure, we could leverage the low losses of phonon polaritons, but gain control over the anisotropic permittivity by manipulating the fill factor. This concept also enables hyperbolic polariton behavior from crystals which have elliptical polaritons in bulk samples, offering a significant degree of flexibility.

Additionally, it has been shown that in atomic-scale superlattices of polar crystals, the optical phonons of constituent materials are confined within individual layers[252–254] and have thickness-dependent phonon characteristics which diverge from bulk properties, and new phonons arise at the interfaces[255–257] between layers, enabling a unique degree of tunability to the typically inflexible optical phonon properties. In this chapter, we explore atomic-scale polar superlattices for engineered IR optical and nanophotonic materials.

4.2 Controlling the IR Dielectric Function through Atomic-Scale Heterostructures

One of the most important technological hurdles for the implementation of SPhPs in nanophotonic and metamaterial technologies is that once a polar material is chosen, the spectral characteristics of the SPhPs it supports are fixed[139]. While there are many polar materials that

occur in nature featuring Reststrahlen bands that combine to cover the entire MIR to THz spectral domain[258], any given material will only support SPhPs within its own relatively narrow specific band. Here, we experimentally demonstrate an approach for broadening the spectral range of the SPhPs by using atomic-scale superlattices (SLs) comprised of commercially established polar semiconductors. When materials are combined into SLs, the SL vibrational modes are modified from that of the bulk phonons of the constituent materials by interfacial chemical bonding, electrostatic effects, and changes to the material lattice constants[259,260]. Confinement effects can arise, resulting in confined phonon modes that oscillate predominantly in one material[259], or new vibrational states can occur that feature phonons redistributed over both materials. Interface phonon modes may also be supported, wherein the vibration is localized to the interfaces between the constituent materials[261]. In addition, significant strain can develop in such atomic-scale SLs, resulting in controllable spectral shifts in the phonon frequencies. As the SL layer thickness is reduced down to a length scale approaching a few monolayers, chemical bonding between the interfacial layers plays an increasingly prominent role in determining the phonon modes in the SL. These phonon modes, in turn, have a direct impact on the SL dielectric function. We refer to such atomic-scale SL structures where the IR dielectric function diverges from its constituents as a crystalline hybrid (XH)[139,262] since it is these changes to the chemical structure of the crystal lattice that modify the IR response.

We demonstrate the XH approach by using atomic-scale AlN/GaN SLs, which exhibit a highly anisotropic IR response featuring multiple Reststrahlen bands. Using second harmonic generation (SHG) phonon spectroscopy, we probe the SL phonon modes and identify multiple confined phonons. We further show that the phonon modes, which define the upper and lower limits of the Reststrahlen bands, shift by >10 cm^{-1} dependent upon the SL layer thicknesses. By

extracting the SL dielectric function via IR ellipsometry, we further illustrate that the SL has spectral regions that support surface-confined SPhPs as well as volume-confined hyperbolic phonon polaritons (HPhPs). In spectral ranges where hyperbolicity is present, the spectral dispersion in both the negative and positive permittivity directions is quite strong, in stark contrast to typical natural hyperbolic materials[43,45,64] and hyperbolic metamaterials[63]. Our results are corroborated by density-functional perturbation theory (DFPT) calculations of the SL vibrational patterns, which show the characteristics of confined and interface modes as well as those of hybrid modes that do not resemble any established profile in macroscopic theory. The XH approach therefore provides the opportunity to modify the optic phonon frequencies, the dielectric function and dispersion of the optical constants, as well as the width of the Reststrahlen bands. Therefore, with more extensive investigations into the XH design principles, we envision the ability to create new engineered materials for IR and THz nanophotonics and optoelectronics, incorporating additional functionalities through appropriate material selection.

In order to demonstrate the XH concept, multiple AlN/GaN SL samples, each with layer thicknesses of ~10 or fewer monolayers, were grown along the wurtzite *c*-axis using molecular beam epitaxy (MBE). A representative schematic of the layered sample configuration is provided in Fig. 4.1a for an AlN/GaN SL grown on a SiC semi-insulating substrate. Wurtzite GaN and AlN are both birefringent with A_1(TO) and A_1(LO) phonon modes that oscillate parallel to the crystal *c*-axis and E_1(TO) and E_1(LO) phonon modes that oscillate perpendicular to the *c*-axis. For GaN (AlN), these bulk phonon frequencies[263,264] are: $A_1(TO) = 533\ (614)\ cm^{-1}$, $A_1(LO) = 735\ (893)\ cm^{-1}$, $E_1(TO) = 561\ (673)\ cm^{-1}$, and $E_1(LO) = 743\ (916)\ cm^{-1}$. In bulk form, AlN and GaN have a similar IR response, with partially overlapping Reststrahlen bands bound by their respective optic phonon frequencies. This is shown in Fig. 4.1b, which

plots the calculated reflectance of bulk GaN (blue), AlN (orange), and SiC (red).

Two representative SL structures, referred to as Samples 'A' and 'B', are discussed here. Sample A, shown in the cross-sectional scanning transmission electron microscope (STEM) image in Fig. 4.1c, consists of 50 alternating layers of AlN and GaN grown on a ~50 nm thick AlN buffer layer. Since this sample was deliberately not rotated during growth, a gradient in the Al- and Ga-flux across the wafer surface resulted in a strong variation in the corresponding layer thicknesses, with values ranging from 2 to 3 nm for the AlN and GaN layers depending on the position on the sample. At the particular location displayed in Fig. 4.1c, each layer is ~ 2 nm thick. Sample B (STEM image in Fig. 4.1e) consists of a SL with 500 atomically thin, alternating layers of AlN and GaN with thicknesses of ~1.2 nm (~4 monolayers) and ~1.4 nm (~5 monolayers), respectively. The layer thicknesses in Sample B are much more uniform across the sample surface, resulting from the sample rotation performed during growth. The STEM and X-ray diffraction (XRD) measurements imply chemical intermixing at the interfaces, and that the SLs are partially relaxed, but with an overall high degree of chemical segregation.

The optic phonon modes of SLs consisting of polar materials[265] including III-nitride materials systems[266–270]have been extensively studied and generally described using both microscopic and macroscopic models[261]. For sufficiently thick layers, it is accepted that the effect of the phonon modes on the SL IR response can be described using macroscopic electromagnetic modeling, e.g. the transfer-matrix method, starting from the bulk permittivity of each layer[271]. A particularly simple macroscopic approximation that applies when the SL layers are much thinner than the wavelength of the light within the materials is the well-known effective-medium theory. However, as the layer thicknesses in the SL are reduced to just a few atomic layers, the SL phonon modes are no longer well described by such macroscopic models. This is because

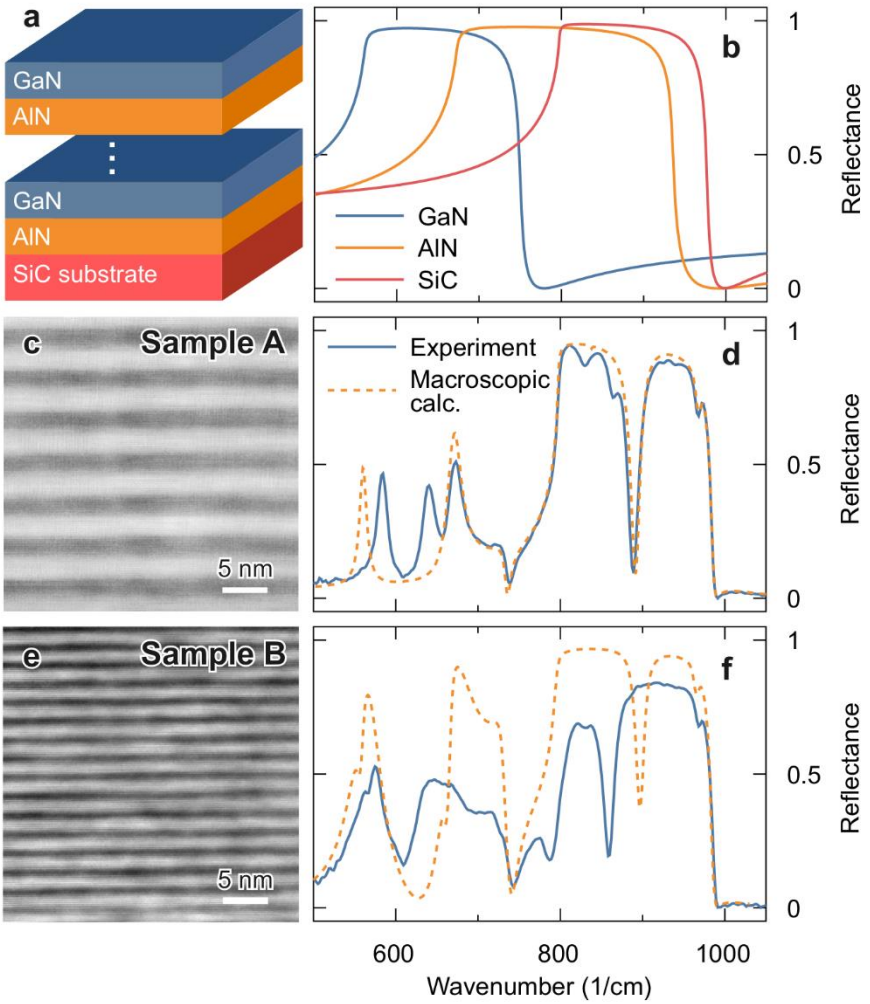

Figure 4.1 *STEM images and reflectance of AlN/GaN heterostructures and Reststrahlen bands. a) Illustration depicting AlN/GaN heterostructures. b) Calculated reflectance of bulk GaN, AlN, and SiC for normal incidence light in the IR, showing the spectral overlap of the Reststrahlen bands. c) and e) display cross-sectional high-angle annular dark-field STEM images of AlN/GaN heterostructures with AlN (GaN) thicknesses of ~2.2 nm (2.2 nm) for Sample A and ~1.2 nm (1.4 nm) for Sample B, respectively. The AlN layers appear as dark-gray bands, and the GaN layers as light-gray bands. d) and f) show the measured reflectance spectra (blue line) at an incidence angle of 65° and the calculations (orange dashed lines) based on the bulk properties of the AlN/GaN SL from c) and e), respectively.*

atomic-scale interactions modify the SL phonon modes, namely, the prominent effects of the interface bonds impose different boundary conditions, and the lattice constants of the epitaxially grown layers deviate from bulk values. This point is illustrated in Fig. 4.1d and 4.1f, where the measured IR reflectance (blue line) is plotted for Samples A and B, respectively, along with the calculated reflectance (orange dotted line) of the SLs using the transfer-matrix method based on

the bulk optical constants of AlN and GaN. It is clear that the conventional approach towards predicting the IR reflectance fails, due to the strong quantitative mismatch of peak positions and the emergence of additional spectral features in the experimental spectra. It is even less accurate for Sample B that features thinner layers and hence exhibits more prominent interface and confinement effects.

In order to compare the DFPT calculation with the IR response of Sample B, we extracted the XH dielectric function from IR ellipsometric spectra. For these XH structures, where the layer thicknesses are only a few monolayers, interfacial bonding plays a significant role in shaping the phonon density of states. In order to account for this effect, we treat the XH structure as a whole and derive a dielectric function for the entire layer. The AlN/GaN XH is strongly birefringent, with very different in-plane and out-of-plane dielectric responses, denoted $\varepsilon_{\perp}$ and $\varepsilon_{\parallel}$, respectively. The dielectric function for a polar semiconductor with *k* phonon modes is given by:

$$\epsilon(\omega)_j = \epsilon_{\infty,j} \prod_k \left(1 + \frac{\omega_{LOk,j}^2 - \omega_{TOk,j}^2}{\omega_{TOk,j}^2 - \omega^2 - i\omega\gamma_{k,j}}\right) \tag{4.3}$$

where $j = \parallel$ or $\perp$ for the permittivity parallel or perpendicular to the *c*-axis[272]. The parameter $\epsilon_{\infty}$is the high frequency dielectric constant, and ω_{LO} and ω_{TO} are the LO and TO phonon frequencies, with a damping parameter of γ. The $\omega_{TO,\parallel}$ and $\omega_{LO,\parallel}$ phonon modes with A_1 symmetry oscillate parallel to the *c*-axis, while the $\omega_{TO,\perp}$ and $\omega_{LO,\perp}$ phonons with E_1 symmetry oscillate perpendicular to the *c*-axis. We extracted the dielectric function of the SL from Sample B (Fig. 4.2 a and b) through least-squares fitting of IR ellipsometry data, using Eq. 4.3 as the fitting function and the WVASE program from J.A. Woollam. However, as spectroscopic ellipsometry is insensitive to the A_1(TO) mode for a basal-plane oriented uniaxial crystal[273]the frequencies of the A_1(TO) mode was determined separately using confocal Raman spectroscopy and fixed as 552 cm^{-1} in the ellipsometric fit. We also used Eq. 4.3 to calculate the dielectric

function using the DFPT-derived phonon modes (Fig. 4.2c and d). For this dielectric function, the damping parameter was empirically chosen to be 10 cm^{-1} for all phonon modes. The extracted parameters from ellipsometry are given in Table 4.1. For comparison, the effective-medium calculations of the XH dielectric function using the optical constants for bulk GaN and AlN measured by ellipsometry are also provided (Fig. 4.2e and f).

Sample	*Mode*	ε_∞	ω_{TO} $[cm^{-1}]$	ω_{LO} $[cm^{-1}]$	γ $[cm^{-1}]$
A	$(E_1)_1$	4.7	584.3	608.3	6.0
	$(E_1)_2$	-	640.2	879.0	8.3
	$(A_1)_1$	8.3	560.0	736.8	8.6
	$(A_1)_2$	-	818	828	15
	$(A_1)_3$	-	852	863.3	10.1
B	$(E_1)_1$	4.8	572	599	14.2
	$(E_1)_2$	-	629	808	18.1
	$(A_1)_1$	5.2	552	725	9.8
	$(A_1)_2$	-	727	740	15.8
	$(A_1)_3$	-	766	798	27.9
	$(A_1)_3$	-	829	859	6.1

Table 4.1 *Phonon mode best-fit parameters of ellipsometry data using Eq. (4.3).*

The effective-medium calculation is based on the average of the GaN and AlN dielectric functions weighted by the relative thickness of the layers. It is clear that the effective-medium calculation fails to predict several important features of the IR response because it does not account for the atomic-scale interactions between the layers. On the other hand, good qualitative agreement with experiment is found with the DFPT-derived dielectric function. The small frequency shifts of the modes between the DFPT and experiment are typical and can be

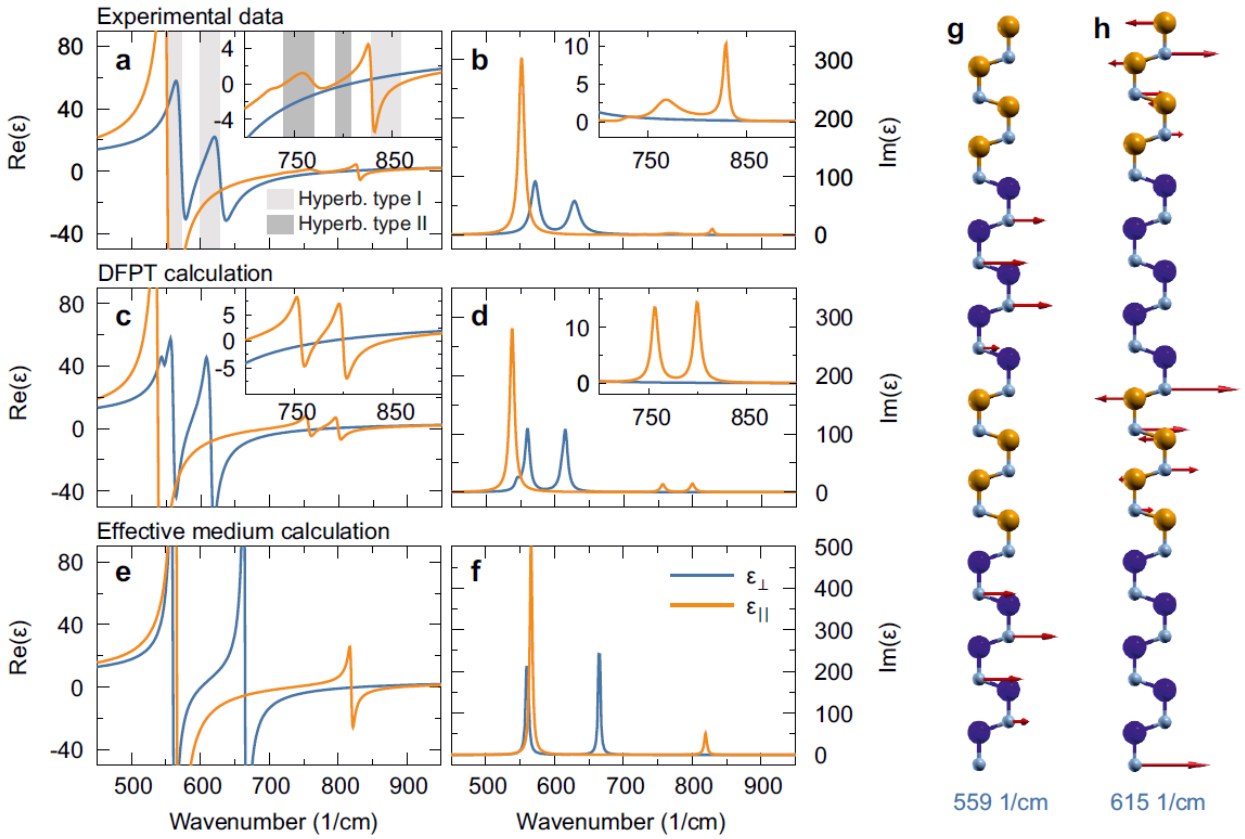

Figure 4.2 *Dielectric function of the atomic-scale AlN/GaN SL. a-b) measured, c-d) calculated using DFPT, and e-f) calculated using effective-medium theory real and imaginary parts of the dielectric function of the AlN/GaN SL (Sample B). The in-plane component, $\varepsilon_{\perp}$, and the out-of-plane component, $\varepsilon_{\parallel}$, are shown in blue and orange, respectively. Highlighted areas in a) mark the hyperbolic regions of type I (light gray) and type II (dark grey). g) and h) phonon vibrational patterns associated with the 559-583 cm^{-1} and 615-784 cm^{-1} Reststrahlen bands, respectively, for $\varepsilon_{\perp}$ shown in c). Blue, orange, and gray spheres denote Ga, Al, and N, respectively, and red arrows denote atomic displacement.*

attributed to the choice of the exchange-correlation functional. The DFPT calculation accurately predicts multiple short-wavelength phonon modes for the out-of-plane permittivity induced by the reduced crystal symmetry of the SL. It can also provide physical insight into the qualitative vibrational character of the modes. Thus, the atomic-scale SL should be considered as a new XH material, with a distinct dielectric function dictated by the atomic-scale interactions within the SL.

From the extracted XH dielectric function, it is found that Sample B exhibits multiple

Reststrahlen bands (identified by regions with $Re(\varepsilon) < 0$) as a result of the induced and shifted optic phonon modes. The poles in the dielectric function occur at E_1(TO)-like and A_1(TO)-like phonon frequencies and the zero crossings near E_1(LO)-like and A_1(LO)-like phonon frequencies for $\varepsilon_\perp$ and $\varepsilon_\parallel$, respectively. The in-plane dielectric function $\varepsilon_\perp$ displays two Reststrahlen bands: one narrow region from 572 cm^{-1} to 599 cm^{-1} and another from 629 cm^{-1} to 807 cm^{-1}. Similar Reststrahlen bands occur in the dielectric function derived from the DFPT calculations (Fig. 4.2c), but with a ≈ 15 cm^{-1} redshift. The calculated phonon vibrational pattern associated with the 559-583 cm^{-1} Reststrahlen band (Fig. 4.2g) illustrate that they most closely resembles a GaN-confined mode. In contrast, the vibrational character associated with the phonons occurring at the phonon frequencies of the 615-784 cm^{-1} Reststrahlen band (Fig. 4.2h) are confined predominantly within the AlN layers, but are centered at the AlN/GaN interface. Importantly, the in-plane Reststrahlen bands of the XH cover a broader range than that of GaN (~561-743 cm^{-1}) and are on the same scale as AlN (~673-916 cm^{-1}). To our knowledge, the only other way to achieve such broadening of the Reststrahlen band is through the inclusion of high densities of free carriers, e.g. via doping[274]. However, this approach introduces substantial increases in loss due to the inclusion of free-carrier scattering, dopant scattering of optic phonons and the increased Drude weight within the dielectric function. To put this in context, we estimate that shift of the Reststrahlen band of GaN out to 800 cm^{-1} via free carriers would require a carrier density of ~$3x10^{18}$ cm^{-3} and would increase $Im(\varepsilon)$ by about six-fold at 800 cm^{-1}. In contrast, even within the non-optimized XH structures discussed here with multiple interfaces and significant strain increased $Im(\varepsilon)$ by about a factor of 3.

The out-of-plane dielectric function $\varepsilon_\parallel$ is dominated by a broad Reststrahlen band extending from ~536 cm^{-1} to ~740 cm^{-1}. Examination of the corresponding vibrational pattern from the DFPT

calculation shows that the phonon mode includes the displacement of nitrogen atoms in both layers. While the nitrogen atomic displacement is larger in the GaN layers, the phonon vibration exhibits an extended character. Two additional Reststrahlen bands are observed within $\varepsilon_{\parallel}$, with one extending from 769 cm^{-1} to 791 cm^{-1} and the other from 828 cm^{-1} to 859 cm^{-1}. Examination of the lattice vibrational patterns indicates that these modes involve atomic movement in both layers, but a larger amplitude in the AlN due to its lighter reduced mass. The energy scale of the optic phonons is mostly driven by the lighter of the two atomic species in a diatomic lattice (here, nitrogen)[275]. The small difference in the reduced masses of GaN (~11 amu) and AlN (~9 amu) results in a spectral overlap of the respective Reststrahlen bands and the limited degree of confinement of the SL phonon modes observed in these structures.

The strongly anisotropic Reststrahlen bands of the XH result in both elliptical (the same sign of $\varepsilon_{\perp}$ and $\varepsilon_{\parallel}$) and hyperbolic (opposite signs) behaviors within the long-wave IR[63]. However, unlike most hyperbolic systems studied to date, the vibrational resonances of the XH and the strong spectral dispersion result in a wide spectral range over which both the positive and negative permittivities vary rapidly with frequency. Due to the rapidly changing dispersion, the birefringence, $\Delta n = n_e - n_o$, of Sample B reaches a maximum of $\approx$ 10 at 527 cm^{-1}, but then drops to ~8 at 566 cm^{-1}. Such extreme birefringence is about an order of magnitude larger than the recently reported materials of $BaTiS_3$ and MoO_3[43,73,276], which exhibit birefringence values of about 0.76 and 0.31, respectively. This highlights an important opportunity to engineer hyperbolic spectral behavior through careful selection of the SL polar semiconductor constituents, thicknesses and epitaxial mismatch.

One challenge associated with using atomic-scale SL designs to modify the IR dielectric function is to ensure the optical loss is not substantially increased. The loss can be quantified by

comparing the damping parameter, γ, of the different modes of the XH to the bulk constituents, GaN and AlN. The damping parameters were extracted from the dielectric function fits for each of the XH phonon modes, with the values falling within the 10 - 25 cm^{-1} range. For comparison with the XH, we also grew films of bulk GaN and AlN and used ellipsometry to determine γ for the phonon modes. The extracted value of γ was ~5 cm^{-1} for the GaN phonon modes and ~15 cm^{-1} for the AlN modes. Therefore, the XH IR losses are on the order of the bulk constituents, and thus can be modified without a dramatic rise in optical losses.

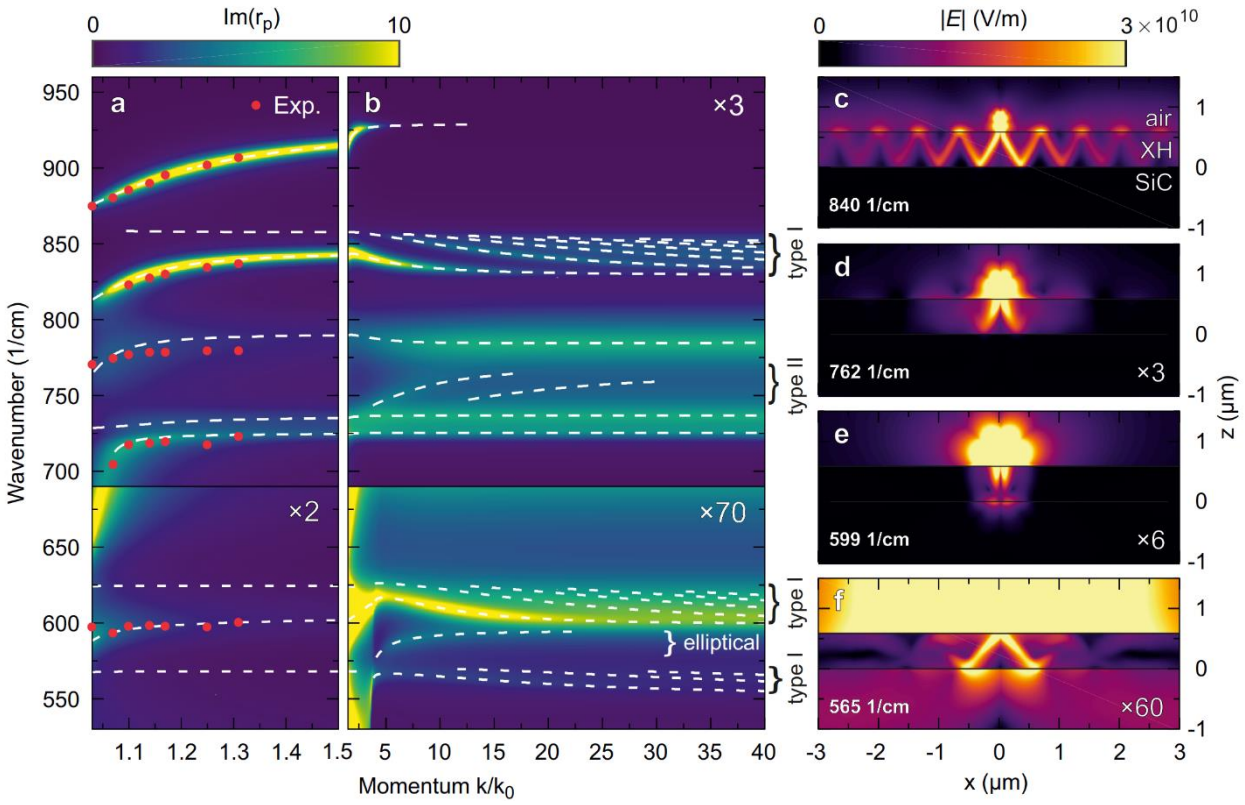

Figure 4.3 *Theoretical polariton dispersion and strongly confined phonon polaritons of the XH. a-b) Imaginary part of the Fresnel reflection coefficient for p-polarized light Im(r_p) of Sample B for evanescent wave excitation as a function of the relative in-plane momentum k/k_0. The dashed lines represent the modes extracted from calculations with reduced damping. The red dots in a) mark the positions of the reflectance dips in the Otto geometry experiments. Hyperbolic mode progression is observed in b) for all three type-I hyperbolic regions. Additionally, one type II hyperbolic mode and a strongly elliptical mode are observed as indicated. c-f) Spatial electric field profiles for localized excitation of hyperbolic modes of type I (c,e,f) and type II (d). The mode shown in e) exhibits a rigid angle of propagation close to zero, since here the positive epsilon component $\varepsilon_\perp$ is nearly zero.*

One test of the validity of the experimentally extracted XH dielectric function is to make accurate predictions of the polariton modes. To this end, we employed prism-coupling in the Otto geometry[215,277,278] which provides experimental access to the dispersion of the polariton modes for wave vectors near the light line, as shown in the schematic of Fig. 4a. Strongly confined hyperbolic and elliptical polariton modes of the XH emerge at larger wavevectors as shown in Fig. 4.3b), as expected from the hyperbolic and elliptical regions of the XH dielectric function, (Fig. 4.2a). Notably, we observe three hyperbolic bands of type I (830-860 cm^{-1}, 599-

625 cm^{-1}, 555-571 cm^{-1}), where only one crystal axis exhibits a negative real part of the dielectric function, which show the typical mode progression[64]. Additionally, we also observe one hyperbolic band of type II (two axes with negative permittivity; 740-770 cm^{-1}) and one elliptical band (all three axes negative; 572-599 cm^{-1}). As a consequence of the rapid dispersion of the XH dielectric tensor and its anisotropy, the properties of these polaritons vary strongly for the different Reststrahlen bands and even within each band. This is in stark contrast to other hyperbolic materials, where the respective positive component of the dielectric tensor is typically constant throughout the hyperbolic dispersion[45,64,78,143]. To illustrate this unique behavior, we calculated optical field profiles of polariton modes from the various branches, with representative examples shown in Fig. 4.3c-f. The strong modulations of both components of the dielectric tensor result in hyperbolic modes whose rigid angle of propagation[141,142,177] and propagation length vary drastically in with small spectral changes.

Notably, the XH concept provides two independent tuning parameters of the polaritonic dispersion: i) modification of the optic phonons through the individual atomic-scale layer thicknesses as demonstrated here, leading to modified number, positions and widths of the polaritonic bands; ii) the total SL stack thickness through the number of SL repeated layers changing the dispersion of the modes within each band. Therefore, the XH concept provides unique opportunities for super-resolution imaging and nanolithography[76,279] with increased spectral flexibility.

An additional major benefit of the XH approach is that it allows for the combination of two materials to achieve a desired IR response, while potentially maintaining their individual mechanical, electrical, and/or optoelectronic functionality. In many instances, it is necessary to combine other material properties (e.g., an accessible band-gap for active tuning[111] or

ferroelectric response[280]) with the polaritonic behavior at a given frequency. For example, while AlN offers a Reststrahlen band that overlaps with the 8-12 μm atmospheric window, its 6 eV bandgap implies that free-carrier-based tuning methods[111] are impractical. However, one can envision active devices based on GaN/AlN SLs, in which the accessible bandgap and controllable doping of GaN can enable free-carrier-based SPPs alongside the SPhP modes. In that case, the electromagnetic hybridization effect[139] and carrier injection could offer routes towards high-speed modulation of the XH polaritonic response[111].

We have demonstrated the use of atomic-scale AlN/GaN SLs for creating hybrid optic phonon modes offering a unique and tunable IR dielectric function. For layer thicknesses approaching the atomic scale, new phonon modes emerge, such that the XHs IR properties are qualitatively distinct from their bulk components. This implies that the resulting SL does not behave as an effective medium comprised of the two bulk materials, but rather as a new XH material with its own unique phonon modes and IR response. We have shown the tunability of the XH optic phonons based on changes to the constituent layer thicknesses, with frequency shifts >10 cm^{-1}, and the emergence of new modes with only atomic-scale differences in the layer thickness required. This provides the opportunity to manipulate the IR response, including the frequencies of the polariton modes and control over the magnitude and dispersion in the IR optical constants, with less additional optical loss as compared to broadening the Reststrahlen band via carrier doping. The AlN/GaN XH has multiple, strongly anisotropic Reststrahlen bands, offering the potential for tailoring the spectral dispersion of both elliptical and hyperbolic spectral regions. The XH offers very large birefringence, with Δn in excess of unity over a large portion of the spectral range, reaching values >10. Such extremely large values of birefringence offer opportunities in a number of application spaces including on-chip optical elements, polarization

control for waveguides, hyperlensing, and enhancing local emitters. In addition, the large birefringence of the XH makes it a promising material for probing the physics of propagating Dyakonov surface waves[214]. By manipulating the IR response, while maintaining other material parameters, XHs provide immense potential for multifunctional nanophotonic devices, for instance by layer-selective ultrafast modulation of the carrier densities. We believe that the implementation and further development of this XH approach will lead to significant advances in IR nanophotonic devices.

4.3 Optical Phonon Confinement Modifications to the IR Dielectric Function

Polar dielectrics have gathered significant interest for infrared (IR) nanophotonic applications. In such materials, optical phonons largely determine the dielectric function and allow for polar materials to host phonon-polaritons: quasi-particles that enable strong light-matter interactions. Phonon-polaritons, in turn, enable low-loss, deeply sub-diffractional confinement of light, with low-symmetry crystals offering significant control over the polariton wave- and Poynting vectors. Cultivating the phonon-polariton for application is therefore an exercise in controlling optical phonons. While different materials will host optical phonons of varying properties; the energies, scattering rates, and orientation of optical phonons are fixed for most individual "bulk" materials, limiting the ability to engineer the IR response. Taking inspiration from hyperbolic metamaterials, superlattices composed of atomically thin layers alternating between dissimilar polar materials offer designed anisotropy by varying the ratio of constituents, and optical phonons are modified by the macro- and micro-structure – creating phonons which are confined to individual layers and interfaces, as well as phonons emerging from the supercell periodicity. Some of these new superlattice modes can interact with IR light, opening the possibility of

creating so-called crystalline hybrids whose IR properties cannot be described as a simple mixture of the bulk constituents. To date, however, studies have primarily focused on identifying the presence of new optical phonon modes rather than assessing their impact on the IR response. Here, we focus on the impact of confined phonon modes on the IR dielectric function of lattice-matched superlattices of GaSb and AlSb to provide an alternative pathway for engineering IR optical materials. Using a combination of first principles modeling of lattice dynamics, Raman, FTIR, and ellipsometric spectroscopy, the dielectric function is found to track directly with the confinement of optical phonons resulting in optical phonon spectral shifts up to $20cm^{-1}$ within GaSb.

Phonons play a key role in dictating many material properties, including acoustic, thermal, electronic, and optical properties. Optical phonons within polar crystals offer a principal driver for nanophotonics in the mid- to far-IR[27,35,145], as they enable the excitation of phonon polaritons (PhPs) which offer lower losses and higher quality factors compared to plasmons [32,88] However, PhPs suffer from limited spectral tunability as they can only be supported within the relatively narrow, nominally fixed spectral window bound by the transverse optical (TO) and longitudinal optical (LO) phonons of the host crystal. Therefore, there is significant interest in methods for tuning the optical phonons, such as through manipulating the isotopic content of the materials[46,168,281], their carrier concentration[282,283], strain[39,222,284–287], or in some cases through ion intercalation[187].

Beyond these extrinsic factors, phonons can also be changed intrinsically by changing the periodicity of the solid. This has been demonstrated by several recent studies that have leveraged crystalline anisotropy as a means to control phonon polaritons. In hBN[45,78], it was shown that the structural anisotropy results in optical phonons with different energies along different crystal

axes, causing the PhPs to become hyperbolic due to the opposite sign of the permittivity along different axes[63]. These hyperbolic phonon polaritons (HPhPs) are of great interest due to their volume propagation, directionality, and large wavevectors[86]. Offering a further degree of asymmetry, MoO_3 has risen as a platform that hosts in-plane hyperbolic polaritons[43,69] which propagate at fixed directions in-plane as well as through the volume, providing enormous utility for steering light propagation in planar optical applications[183–185,198,232]. Crystals which have strong anisotropy as well as non-orthogonal lattice vectors (monoclinic and triclinic systems) have been shown to host exotic polaritonic behavior where both the polaritonic wavevector and the propagation direction disperse as a function of frequency[29].

While natural crystals offer a broad toolbox of optical phonons, the lack of control over bulk phonon properties remains a significant limitation for applications. Instead, anisotropy can be purposely designed in heterostructures via a change in periodicity. This provides additional freedom in the tailoring of PhPs. Twisted two-dimensional slabs (I.e., "twist-optics"), for example, can modify the hyperbolicity of PhPs[184,185,198,288] and even serve as a mode of active tuning[289]. Alternatively, so-called crystalline hybrids can be created via more traditional semiconductor superlattices (periodic stacks of thin films) to sculpt the IR response[140,254]. Ratchford et al.[254] demonstrated that the confined and interface phonon modes that occur in atomic-scale superlattices of GaN and AlN are capable of significantly altering the IR dielectric function. The resulting hybrid material with its modified dielectric function enables a suite of extremely dispersive elliptical and hyperbolic polaritons as a result of the complex phonon interactions and superlattice anisotropy. In order to predictively design such systems using this approach, it is necessary to develop our understanding of the emergent phonon behavior and determine how this impacts the IR optical properties (i.e., the dielectric function) of the resultant

hybrid material.

It is known that in semiconductor superlattices, phonons exhibit new behaviors not seen in the bulk material constituents. Acoustic phonons in the different superlattice layers have largely overlapping energy ranges and long wavelengths due to the nature of their dispersion and are thus able to propagate through the entire superlattice, undergoing zone-folding due to the long-range periodicity within the structure[290,291]. These folded phonons can be used to significantly modify the thermal conductivity of the structure[292,293] .In SiC, optical phonons can also exhibit zone-folding resulting from the different super-cell structures associated with the multiple natural polytypes[294], which can interact with transverse phonon polaritons for novel nanophotonic applications[295]. However, for superlattices where the optical phonons in different layers occur at different energies, the optical phonons can become 'trapped' within a single layer, resulting in a so-called confined phonon[252,253,296–299]. In addition, new phonons resulting from the modified bonding, strain and local dielectric environments occurring at the interfaces between superlattice layers are also observed[300]. The combination of these modifications to the optical phonon properties is the basis for the anticipated modifications in the IR dielectric functions at the heart of the crystalline hybrid approach.

Optical phonon confinement has been extensively demonstrated in Raman scattering studies for superlattices in multiple material systems[252–254,301,302] and has even been observed in a singular thin film[303]. The confinement of the optical phonon manifests in Raman measurements as a spectral shifting of the optical phonon frequencies as well as the introduction of additional TO and LO phonons. These confined phonons have been described as sampling the bulk phonon dispersion along the confinement direction, with the momentum given by:

$$k(m) = \frac{2\pi m}{(n+\delta)d_0}, \quad m = 1,2,\dots,n \tag{4.4}$$

where m is the mode order, n is the number of monolayers (ML) in the confined layer, d_0 is the lattice constant, and δ is a correction term which is typically attributed to the interface leakage – i.e. how many MLs past the interface are included in the phonon oscillation[298,299]. The δ term has typically been assumed to be 0 or 1, indicating that the atomic displacement from the phonon stops at the interface or the first atom (half of a ML on both sides) past the interface.

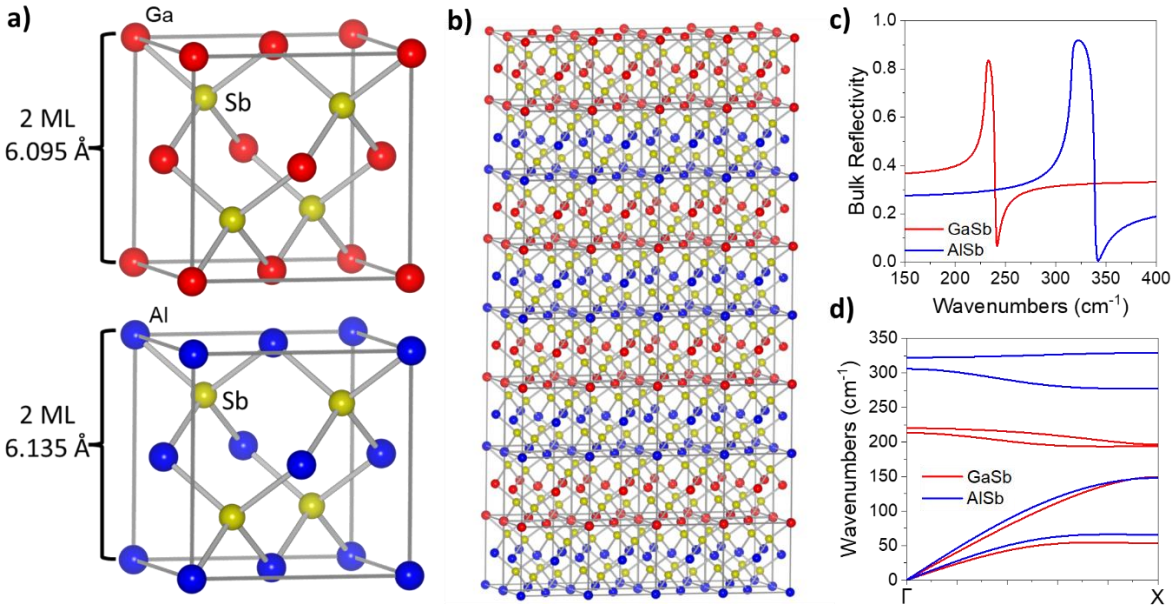

Figure 4.4 *Superlattice Diagram. A) Crystal structure of GaSb and AlSb unit cells. b) Diagram of 2ML/2ML superlattice. c) Bulk Reflectivity of constituent materials. d) Bulk phonon dispersion plots along the Γ-X Brillouin zone (superlattice direction) of GaSb (red) and AlSb (blue).*

Most studies of confined phonons have relied on superlattices with layer thicknesses on the order of 10s of MLs, supporting many higher-order modes. This approach is an efficient way to probe the phonon confinement using Raman spectroscopy investigations and has been considered as an alternative to neutron scattering measurements for mapping the optical phonon dispersion. However, using superlattices with high layer thicknesses results in weakly shifted first order modes and small deviations between higher order modes. In order to explore the tunability of the $m = 1$ mode, which we expect to be the primary driver for the IR optical response, we instead

vary the layer thickness across a number of samples.

The initial proof-of-concept demonstration of crystalline hybrid materials showed the ability to create a modified dielectric material with novel nanophotonic properties through deterministic, atomic-scale superlattice design. However, while AlN/GaN superlattices studied previously[254,273] host polaritons within a technologically important atmospheric window, the large lattice mismatch and partial overlap of the Reststrahlen bands in GaN and AlN lead to strain-induced phonon shifts in addition to a suite of new confined, quasi-confined, and unconfined phonons that limit predictive design.

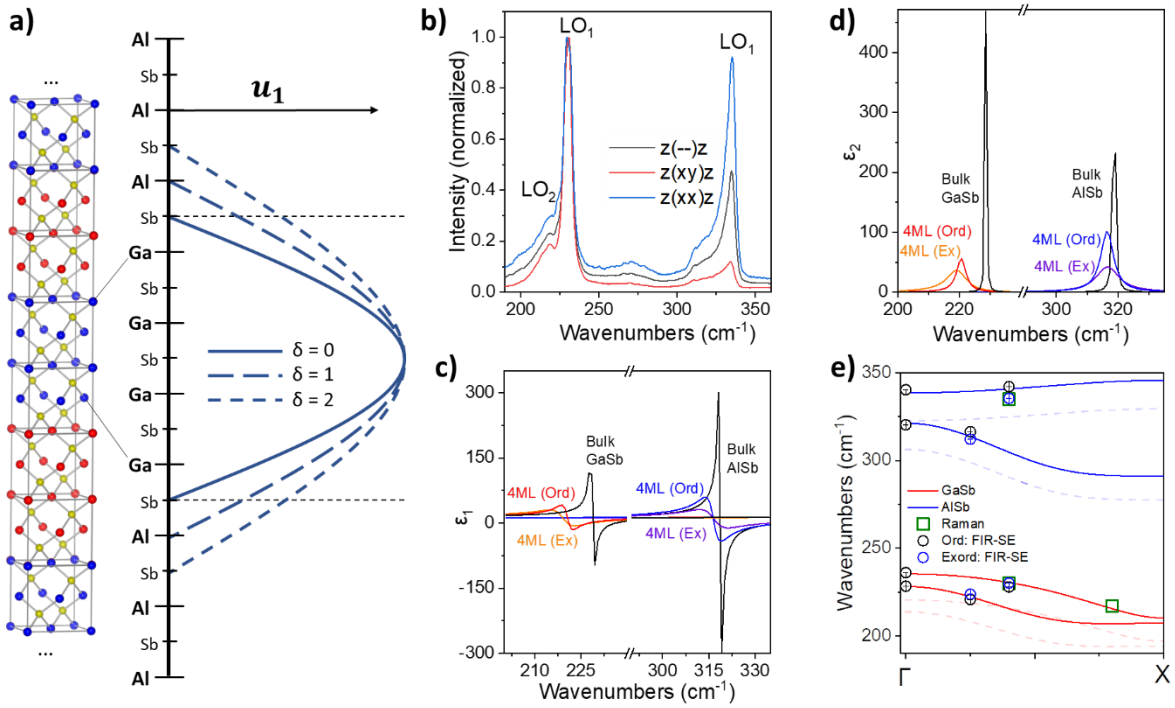

Figure 4.5 *Phonon confinement in 4 ML GaSb /4 ML AlSb superlattice. a) schematic of 4 ML/4ML superlattice, with atomic displacement shown for m=1 mode. Multiple δ values are shown, indicating the meaning of the interface leakage term. b) Raman spectra of 4ML/4ML superlattice, with single LO phonon (LO_1) observed in the AlSb range, and 2 LO phonon peaks observed in the GaSb range (LO_1, LO_2). c-d) Real (c) and imaginary (d) permittivity for the 4ML GaSb and AlSb layers, in the ordinary and extraordinary axes, compared to the bulk dielectric function (black).e) Bulk dispersion curves for GaSb and AlSb, calculated in DFT, with overlaid phonon frequencies from Raman (green squares) and FIR-SE (circles).*

To isolate and explore the impact of optical phonon confinement upon the IR dielectric function, we leverage superlattices of GaSb and AlSb (Fig. 4.4a,b). This system offers a low lattice mismatch to minimize strain, spectrally separate Reststrahlen bands (Fig. 4.4c,d), and a shared cation (Sb) to minimize the interface phonon contribution. The minimization of the interlayer strain is imperative as this allows for the investigation of the corresponding optical phonon modifications without the presence of significant strain induced spectral shifts. Thin films of GaSb and AlSb are currently used in optoelectronic devices such as IR detectors and lasers[304–306], so high-quality growth is well developed. In addition, the zinc blende structure (Fig. 4.4a) makes the bulk constituent materials optically isotropic, simplifying measurements and dielectric function modeling. The superlattices employed here were grown using molecular beam epitaxy (MBE), enabling ML-level control of layer thickness and high-quality interfaces[307].

To start, we use an exemplary superlattice with thin (4ML) layers of GaSb and AlSb and with a large overall thickness (~10μm) to mitigate any contribution from the underlying substrate. Within such a superlattice, the vibrational amplitude of confined phonons can be described as:

$$u_m(B_2) \propto \cos\left(\frac{m\pi z}{n+\delta}\right),\ m = 1,3,5,\ldots \tag{4.5}$$

$$u_m(A_1) \propto \sin\left(\frac{m\pi z}{n+\delta}\right),\ m = 2,4,6,\ldots \tag{4.6}$$

The m=1 mode (Fig. 4.5a) is typically much stronger than higher-order modes in Raman studies, so we expect it to dominate the dielectric function. Using superlattice samples with spectrally-offset constituent Reststrahlen bands allows us to confine the phonons within a single material, enabling individual control over the phonon properties in layered materials. To model the AlN/GaN atomic scale superlattice, Ratchford et al. used a single, anisotropic model to fit the full hybrid material simultaneously[254]. This was necessary due to the complex phonon interaction

between layers resulting from the partially spectrally-overlapping Reststrahlen bands of AlN and GaN. Our use of materials with spectrally-offset Reststrahlen bands eliminates folded optical phonon modes and allows us to extract the dielectric function of superlattice layers individually to determine the thickness dependence of the phonons within an individual, nanoscale-thickness material.

We measure Raman scattering from the superlattice under multiple polarization conditions with a 532nm excitation laser, observing a number of features which vary with polarization (Fig. 4.5b). Under non-resonant conditions, cross-polarized Raman preferentially scatters odd-ordered LO phonons, whereas parallel polarized Raman scatters more of the even-ordered LO phonons, as well as TO and interface phonons[308]. Using these rules, we can attribute the peaks in the parallel-polarized Raman spectra to the even-order confined phonons and interface modes, and the other prominent peaks in the cross-polarization spectra to odd-order confined LO modes. The spectra show a strong LO_1 mode in both the GaSb and AlSb regions, as well as a much weaker LO_2 peak in the GaSb region. There are some weak background features which were previously attributed to large wavevector scattering processes and electronic transitions,[308] which we will not consider in this study.

In order to precisely determine the optical response of the thin layers of GaSb and AlSb, we leverage far-IR spectroscopic ellipsometry (FIR-SE) measurements of the 4ML/4ML superlattice. Using the FIR-SE spectra, we model the dielectric function of each layer in the sample (GaSb substrate, 350nm AlSb buffer, 3279 periods of 4ML AlSb/ 4ML GaSb, and a 5nm GaSb capping layer) as a TOLO oscillator. Bulk GaSb and AlSb are isotropic, so we treat the thick layers (substrate, buffer, capping layer) as isotropic. For the thin layers, we assume that phonon confinement will change the ordinary and extraordinary axes differently; so, we model

the 4ML layers as uniaxial TOLO oscillators (Note: we ignore any variation between the 4ML layers and assume they are identical – using one model for the 4ML GaSb, and another for the 4ML AlSb layers). The uniaxial TOLO model relies on the phonon frequencies, and a phonon damping term γ:

$$\varepsilon_j = \varepsilon_\infty \left(1 + \frac{\omega_{LO,j}^2 + \omega_{TO,j}^2}{\omega_{TO,j}^2 - \omega^2 - i\omega\gamma_j}\right) \qquad j = ex, ord \tag{4.7}$$

Our ellipsometric modelling provides a dielectric function for the thick layers of GaSb and AlSb which agree with literature values for bulk crystals, as well as our measurements of bulk samples, so we use these as the bulk dielectric functions for comparison.

We find that our single uniaxial TOLO model for the 4ML layers provides an excellent fit to the FIR-SE measurements, suggesting that the optical response is indeed dominated by a single set of TO and LO phonons. The TOLO resonance is red-shifted and broadened in both axes compared to the bulk dielectric function in both GaSb and AlSb (Fig. 4.5c,d). We expected the ordinary and extraordinary phonon frequencies to diverge since the layer thickness is only confined in the ordinary axis – instead the phonon frequencies do not diverge strongly, but the extraordinary TOLO resonance is further broadened compared to the ordinary axis.

The altered dielectric function of the thin layers suggests that we may be seeing the effects of confinement on the optical phonons. However, in order for this change in the dielectric function to provide an effective design tool, it needs to follow a predictable trend – ideally the phonon confinement model from literature. In order to determine whether the phonon shifts are attributable to confinement effects, we use Eq. 1 to map the measured phonon frequencies from Raman and FIR-SE measurements to a calculated bulk phonon dispersion in the Γ-X Brillouin zone (superlattice direction) for GaSb and AlSb (Fig. 4.5e).

The calculated phonon dispersions from DFT (faint dashed lines in Fig. 4.5e) fall slightly short

of the bulk phonon frequencies at the Γ-point. To compensate for this discrepancy, we offset the dispersion curves by ~ 14cm^{-1} to match our measurements and literature values of the bulk phonon frequencies at the Γ-point (solid lines in Fig. 4.5e). For the measured LO phonons, we use a δ value of 1, indicating that the vibrational amplitude of the confined phonon terminates at the first anion atom (Al or Ga) after the interface (Fig. 4.5a). We find that for both the Raman measurements (black circles) and the phonon frequencies extracted from the FIR-SE measurements, the observed phonons correspond well to a confined *m*=1 mode. The ordinary and extraordinary phonon frequencies from our ellipsometric modeling do not overlap perfectly – we suspect that there is a slight variation in how strongly the confinement affects these phonons.

Most previous work on phonon confinement has relied on Raman scattering, which is typically insensitive to TO phonons. Therefore, while the TO phonon provides the main contribution to the optical response, understanding of TO phonon confinement is limited. In the initial works describing phonon confinement in GaAs/AlAs superlattices, both confined TO and LO phonons were observed and mapped to the bulk dispersion, but the same δ value could not be used for both sets – suggesting that TO and LO phonons experience different levels of confinement. Here, we find that using δ=1 works well for the observed LO phonons but provides a poor fit for the TO phonons. However, δ=3 results in good agreement to the bulk dispersion for both the GaSb and AlSb confined TO phonons. This suggests that the confined TO phonon vibration continues for one ML past the interface and stops at the next anion atom. This discrepancy in the δ term suggests that the TO phonons are more weakly confined by the superlattice barrier, and that the anion (Ga,Al) still provides the vibrational barrier.

While the optical phonons observed in the 4ML/4ML superlattice appeared to show phonon confinement-induced changes to both the AlSb and GaSb phonons, we cannot make any

conclusive observations from a single superlattice sample. In order to use the layer thickness to engineer the phonon properties, we must understand how phonon confinement develops as the layer thickness changes. The AlSb LO phonon dispersion is much flatter than the GaSb phonon dispersions, making it difficult to discern confined LO phonons in the AlSb layers. Therefore, we focus on further exploration of the GaSb optical phonons.

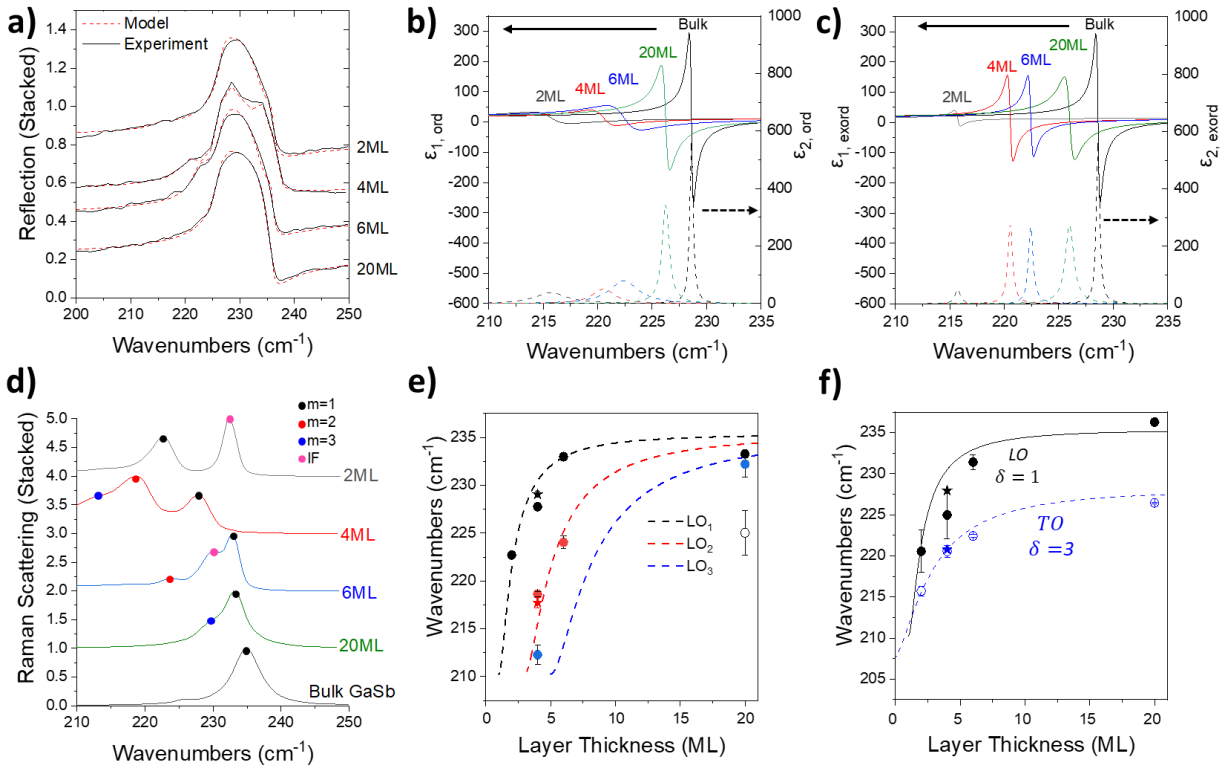

Figure 4.6 *Exploring thickness dependence of phonon confinement. a) FTIR reflectance spectra of superlattices with 20ML AlSb alternating with varying thicknesses of GaSb. b) Ordinary dielectric function of GaSb layer at varying GaSb layer thicknesses, as extracted from FTIR studies. c) Extraordinary dielectric function of GaSb layer at varying thicknesses. d) Raman measurements of confined GaSb phonons for varying GaSb layer thicknesses. e) Confined phonon peaks from Raman (d), plotted against the confined phonon dispersion (dashed lines). Measurements of the 4ML/4ML superlattice from Fig. 2 included as stars. f) Ordinary phonon frequencies from (b), plotted against the confined phonon dispersion (m=1). Phonon frequencies from ellipsometry (Fig. 2) plotted as stars.*

To explore the changing thickness, we use samples consisting of superlattices with 20ML AlSb layers alternating with GaSb layers with thicknesses of 20, 6, 4, and 2ML. Measuring the

reflectance using a Fourier Transform infrared (FTIR) spectrometer (Fig. 3a), we observe the underlying Reststrahlen band from the bulk GaSb substrate, but we also observe subtler features from the superlattice layers which shift with the change in thickness. Using the same method of permittivity modelling as with the previous FIR-SE data, we extract the dielectric function of the GaSb layers (Fig. 3b,c). With FTIR, we are less sensitive to the extraordinary optical response, so we fix the extraordinary TO phonon frequency equal to the ordinary TO phonon frequency, which did not diverge strongly at 4ML (Fig. 4.5e). From the extracted dielectric function, we clearly see the phonon resonance redshift and broaden with decreasing thickness (Fig. 4.6b,c). The staggered trend in the extraordinary amplitude (Fig. 4.6c) is attributed to our decreased sensitivity, otherwise there is good agreement between the ordinary and extraordinary axes.

We also characterize these thickness-varying superlattices with Raman spectroscopy (Fig. 4.6d). In these samples, we observe multiple peaks corresponding to up to m=3 confined LO phonons which shift monotonically with the changing thickness. We also observe strong peaks in a few samples which do not correspond to confined phonons. From the Raman selection rules discussed previously, we attribute these to interface phonons and disregard them.

With multiple higher-order phonons observed in varying thickness samples, the conventional method of plotting confined phonon peaks on the bulk phonon dispersion provides little information. Instead, we can invert Eq. 4.4 to get an expression for the confined phonon dispersion, which is a function of the mode order *m* and the number of MLs *n*.

$$\mathrm{k_0(m) = k(m) \div \frac{\pi}{d_0} = \frac{2m}{n+\delta}} \tag{4.8}$$

$$\mathrm{n = \frac{2m}{k_0} - \delta} \tag{4.9}$$

Now we can use this to plot the thickness-dispersion for the different order confined phonon modes. Note that for this we have to choose a value for δ, which simply shifts the curve to the

left or right on the x-axis. As in Figure 4.5, we use δ=1 for the LO phonons, and δ=3 for the TO phonons.

Using this confined phonon dispersion, we can overlay the observed Raman peaks for the different GaSb thicknesses and see how the confined phonons disperse as a function of the layer thickness (Fig. 4.6e). This confined phonon dispersion exaggerates any deviation from the confinement model but shows confinement shift of the various-order phonons as a function of the number of layers – providing a more predictive view which we can use to evaluate engineering potential. It is clear from this view that for GaSb, there is significant first-order phonon shift with thickness up to about 8ML, after which the frequency asymptotically approaches its bulk value (Fig. 4.6e). The confined phonons observed in Raman fit well with the confined phonon dispersion. Higher order modes exhibit larger shifts and a wider range of thickness-tunability.

The TO and LO phonons extracted from FTIR measurements track well with the *m=1* confined phonon dispersion (Fig. 4.6f). The thickness dependent behavior of the TO phonons agrees very well with a δ value of 3 – supporting our observations from the 4ML/4ML superlattice in Figure 4.5. The extracted LO phonons follow the confined phonon dispersion fairly well, but because LO phonons are not IR-active we have larger error bars and worse agreement. We also want to note here that the confined GaSb phonons measured in the 4ML/4ML superlattice agree well with those observed in a 4ML GaSb / 20ML AlSb superlattice (Fig. 4.6e-f stars indicate 4ML/4ML sample). This suggests that in spite of the interface leakage described by δ, phonon confinement is largely tolerant of the barrier layer width (i.e., GaSb phonon confinement is only a function of the GaSb layer thickness).

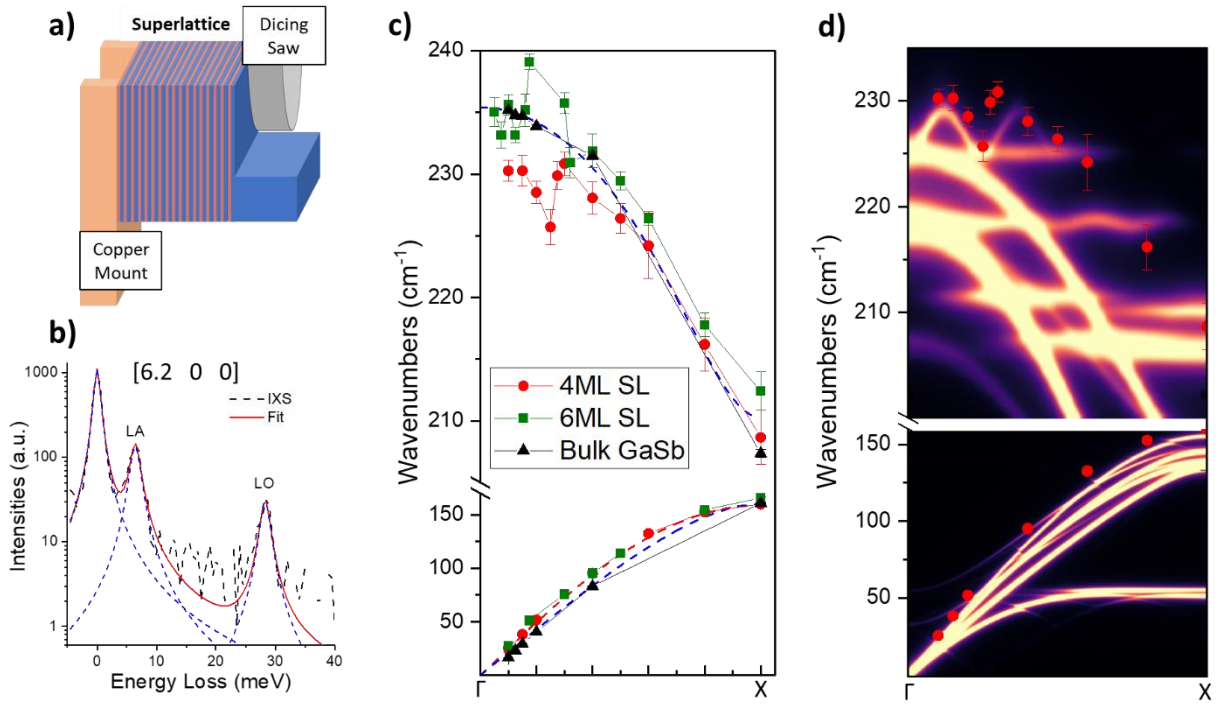

Figure 4.7 *High-resolution momentum resolved inelastic X-ray scattering to probe the superlattice phonon dispersion. a) Schematic of mechanically thinning the substrate supporting the superlattice sample (The sample was not mounted on a cooper post during dicing, it was mounted on a copper post during the measurements) . b) Inelastic X-ray scattering spectrum, with peak-fits showing the elastic (zero loss) peak, the longitudinal acoustic phonon peak, and longitudinal optical phonon peak, at 0.2 reduced momentum in the Γ-X Brillouin Zone. c) LO and LA phonon peaks observed in inelastic X-ray scattering of bulk GaSb (black triangles), the 4ML superlattice from Fig. 2 (red circles), and a 6ML GaSb/ 6ML AlSb superlattice (green squares) Overlaid on LO and LA dispersions of bulk GaSb (blue dashed lines) and bulk AlSb (red dashed lines) . d) DFT phonon dispersion of 4ML GaSb/ 4ML AlSb superlattice, with overlaid IXS LO phonon peaks.*

properties. From the Γ-point measurements, it is clear that phonon confinement alters the phonon dispersion – but the size of superlattices is incompatible with neutron scattering which typically requires bulk samples, precluding direct measurements of the confinement-induced changes to the phonon dispersion.

High-energy-resolution inelastic x-ray scattering [309] is an alternative to neutron scattering which allows to perform momentum and energy-resolved measurements of the phonons on smaller samples, down to ~ few μm in size. While this is pushing the limits of MBE-grown atomic-scale

superlattices, it is achievable. To that end, the 4ML/4ML superlattice discussed in Fig. 4.5 was grown to an overall superlattice thickness of ~10 μm. For comparison, we also grew a 6ML GaSb/ 6ML AlSb sample with similar overall thickness, the 4ML and 6ML samples were grown on GaSb substrate.

The bulk GaSb substrate of these samples introduced an additional scattering due to the large penetration of the x-ray beam, 23.72 keV, which interfered with a signal coming from the superlattice. In order to minimize the scattering from the substrate and isolate the scattering signal to the superlattice, we thinned down most of the substrate supporting the 4ML using a diamond dicing machine, as demonstrated in Fig. 4a). As a result of that, we were able to remove most of the substrate, so that the overall sample thickness was within a few μm of the superlattice thickness. The 4ML was then mounted on a copper holder on the HERIX spectrometer at sector 30 at the Advanced Photon Source., The measurements were done in transmission mode. We then measured the energy loss spectrum by scanning the energy of the incident x-ray beam at a fixed momentum. From our choice of momentum, we selectively scatter from the longitudinal phonons (Fig. 4.7b) and map out the Γ-X Brillouin zone (Fig. 4.7c). The measurements were performed close to (600).

Our measurements of a bulk GaSb substrate align very well with the longitudinal phonon dispersion we calculated using DFT (after shifting to match Raman frequencies), confirming our bulk GaSb phonon dispersion. The observed phonon features in the 4ML and 6ML superlattices agree well in the acoustical region – although the peaks are slightly blue-shifted due to the addition of AlSb acoustical phonons, which are too closely overlapping to resolve in IXS. At higher momenta, nearing the X-point, the LO phonons of the superlattice also largely agree with the bulk GaSb phonons outside of some energy offset we attribute to strain induced by the

mechanical thinning. However, near the confined layer thickness (~1/4 for the 4ML superlattice, and ~1/6 and ~1/3 for the 6ML superlattice) there is a marked deviation from the slowly dispersing bulk trends. In order to understand this deviation, we calculated the phonon dispersion for a 4ML GaSb / 4ML AlSb superlattice in DFT (Fig. 4.7d). Unfolding the superlattice phonons prevents us from including TO-LO splitting, so the bulk-like mode is shifted down – but there is a new superlattice feature near the Γ-point which damps out quickly with increasing momentum but appears to align well with the feature observed in IXS (Fig. 4d).

Our IXS measurements, coupled with DFT calculations support the idea that phonon confinement impacts the off- Γ phonon dispersion. These results suggest that the phonon confinement effect results in a highly dispersive phonon branch which dominates the scattering behavior near the Γ-point, and the phonon behavior approaches the bulk dispersion as the momentum increases. This behavior is inherently different from zone-folding and other superlattice effects which have been demonstrated previously.

Here, we have shown that optical phonon confinement in thin film superlattices can be employed as a means to directly modify the IR dielectric function of the material. We have also shown that this phonon confinement appears to be largely independent of the barrier width, offering the possibility to modify the constituent phonon behavior independently of the overall superlattice anisotropy. Additionally, we have provided an alternative view of the phonon confinement model, which enables predictions of optical phonon properties in thin films that may be useful not only for IR optics, but also for applications benefiting from controlling optical phonon behavior at the atomic scale. We demonstrate some initial efforts to understand the impact of phonon confinement on the phonon dispersion, which may have significant consequences in phonon scattering applications.

CHAPTER 5

Conclusions and Future Directions

While goal of this dissertation is to cover our efforts in the field of anisotropic nanophotonics, I hope it can also serve as an introduction to the field for future students and other readers. This field of study is quite young, and many of the efforts described here represent exciting new thrusts which we hope will branch out into further discoveries. In this chapter, I provide my thoughts on relevant advances and the future directions I find most exciting.

5.1 hBN Devices

In Chapter 2, we describe many of our efforts to manipulate the prototypical hyperbolic phonon polaritons in hexagonal Boron Nitride. Our efforts go a long way towards developing real devices from these nanophotonic modes – demonstrating the first refractive polariton devices, ultrafast modulation, and unique access of the assorted momenta of the polariton resonances.

Recent works from other groups have built on our initial refractive polaritonic metasurface work to demonstrate phase-change lensing with the GST phase change material[310], and in patterned resonators on MoO_3[94]. Other work in our group has integrated a similar type of waveguide in hBN polaritons with silicon waveguides for telecom wavelengths, for dual use waveguides[230]. Future work combining refractive propagation control with fast modulation, such as our demonstration with doped substrates, would be a powerful motivation for applications in on-chip optics and computing.

5.2 Low Symmetry Crystals

In Chapter 3, we explore the unique nanophotonic properties of phonon polaritons in lower

symmetry crystals. Our work here supports MoO_3, and particularly β-Ga_2O_3 (bGO) as exemplary materials for gaining further control over the polariton propagation – and also strongly supports general interest in the broad range of natural crystals with low degrees of symmetry.

Future studies of other naturally occurring monoclinic and triclinic crystals will yield an incredible toolbox for infrared nanophotonics. In particular, the monoclinic system is by far the most prevalent system of naturally occurring crystals, presenting an excellent space for future discoveries. There are also a number of triclinic crystals which have garnered attention recently, including ReS_2 and $ReSe_2$[226], that should exhibit even more exotic polariton behavior.

The studies presented in this chapter represent the first explorations of nanophotonics in such low symmetry crystals. The next steps of incorporating such materials into more complex devices, such as heterostructures like those discussed in Chapter 2, the tunable graphene/phonon polariton devices demonstrated with hBN[137,221] and MoO_3[311], or "twist-optics" heterostructures like those demonstrated in rotated MoO3 bilayers[184,185] are all incredibly promising avenues of study.

Lastly, the 'shear' behavior of the phonon polaritons in bGO are strictly a result of the monoclinic axis residing on the sample surface. Other crystal-cuts of bGO are available, which place the monoclinic axis out of the sample surface, which will change the orientation of the off-diagonal permittivity. This would result in the rotation of the optic axis being out-of-plane, which will have unique consequences on the polariton propagation, and hints at phenomena like the "ghost" polaritons in off-cut Calcite[44]. Additionally, exploring volume-confined hyperbolic modes in thin films or flakes[312] of these materials should present an entirely new facet to these polaritons which is thus far unexplored.

5.3 Engineered Anisotropy

In Chapter 4, we explore superlattice systems in which we can engineer crystal anisotropy, as well as leverage the changes in optical phonons in thin films as a way to engineer the optical phonon properties of the material. Our work here shows the power of atomic-scale superlattices for creating highly anisotropic optical and nanophotonic materials – and also provides some insight into the phonon confinement mechanism which largely dominates the changes to the optical phonon properties.

While our goal was to develop the understanding of this concept for engineered uniaxial materials, this could be extended to more anisotropic materials, or to more heterogeneous constituent materials where strain effects might allow for control over the in-plane asymmetry.

5.4 Closing Perspective

Including the works described in this dissertation, there is rising interest in the use of anisotropic materials for nanophotonics. While phonon polaritons are of interest for infrared optoelectronic devices[313], much of the work described in this dissertation is broadly generalizable. The implications of anisotropic permittivity, and off-diagonal permittivities on the supported optical topology have strong relevance for metasurfaces, photonic crystals, and other physical systems with multiple coupled oscillators.

References

1. Karim, F., Smith, T. B. & Zhao, C. Review of optical detection of single molecules beyond the diffraction and diffusion limit using plasmonic nanostructures. *https://doi.org/10.1117/1.JNP.12.012504* **12**, 012504 (2017).
2. Acuna, G., Grohmann, D. & Tinnefeld, P. Enhancing single-molecule fluorescence with nanophotonics. *FEBS Lett.* **588**, 3547–3552 (2014).
3. Mivelle, M., Van Zanten, T. S., Manzo, C. & Garcia-Parajo, M. F. Nanophotonic approaches for nanoscale imaging and single-molecule detection at ultrahigh concentrations. *Microsc. Res. Tech.* **77**, 537–545 (2014).
4. Nüesch, M. F. *et al.* Single-molecule Detection of Ultrafast Biomolecular Dynamics with Nanophotonics. *J. Am. Chem. Soc.* **144**, 52–56 (2022).
5. Vlasov, Y. A. Silicon CMOS-integrated nano-photonics for computer and data communications beyond 100G. *IEEE Commun. Mag.* **50**, (2012).
6. Karabchevsky, A., Katiyi, A., Ang, A. S. & Hazan, A. On-chip nanophotonics and future challenges. *Nanophotonics* **9**, 3733–3753 (2020).
7. Fang, Y. & Sun, M. Nanoplasmonic waveguides: towards applications in integrated nanophotonic circuits. *Light Sci. Appl. 2015 46* **4**, e294–e294 (2015).
8. Atwater, H. A. *et al.* Materials challenges for the Starshot lightsail. *Nat. Mater. 2018 1710* **17**, 861–867 (2018).
9. Brewer, J. *et al.* Multiscale Photonic Emissivity Engineering for Relativistic Lightsail Thermal Regulation. *Nano Lett.* (2022) doi:10.1021/acs.nanolett.1c03273.
10. Gansel, J. K. *et al.* Gold helix photonic metamaterial as broadband circular polarizer. *Science (80-.).* **325**, 1513–1515 (2009).
11. Yu, N. & Capasso, F. Flat optics with designer metasurfaces. *Nat. Mater.* **13**, 139–150 (2014).
12. Folland, T. G. *et al.* Probing hyperbolic polaritons using infrared attenuated total reflectance micro-spectroscopy. *MRS Commun.* (2018) doi:10.1557/mrc.2018.205.
13. Molesky, S. *et al.* Inverse design in nanophotonics. *Nat. Photonics* **12**, 659–670 (2018).
14. Gomez-Diaz, J. S. & Alù, A. Flatland Optics with Hyperbolic Metasurfaces. *ACS Photonics* **3**, 2211–2224 (2016).

15. García-Meca, C. *et al.* On-chip wireless silicon photonics: From reconfigurable interconnects to lab-on-chip devices. *Light Sci. Appl.* **6**, 1–11 (2017).
16. Autore, M. *et al.* Boron nitride nanoresonators for Phonon-Enhanced molecular vibrational spectroscopy at the strong coupling limit. *Light Sci. Appl.* **7**, (2018).
17. Langer, J. *et al.* Present and future of surface-enhanced Raman scattering. *ACS Nano* **14**, 28–117 (2020).
18. Ding, S. Y. *et al.* Nanostructure-based plasmon-enhanced Raman spectroscopy for surface analysis of materials. *Nat. Rev. Mater.* **1**, (2016).
19. Li, J. F. *et al.* Shell-isolated nanoparticle-enhanced Raman spectroscopy. *Nature* **464**, 392–395 (2010).
20. Santori, C. *et al.* Nanophotonics for quantum optics using nitrogen-vacancy centers in diamond. *Nanotechnology* **21**, (2010).
21. Tran, K. *et al.* Evidence for moiré excitons in van der Waals heterostructures. *Nature* **567**, 71–75 (2019).
22. Tran, T. T., Bray, K., Ford, M. J., Toth, M. & Aharonovich, I. Quantum emission from hexagonal boron nitride monolayers. *Nat. Nanotechnol.* **11**, 37–41 (2016).
23. Scholl, J. A., Koh, A. L. & Dionne, J. A. Quantum plasmon resonances of individual metallic nanoparticles. *Nature* **483**, 421–427 (2012).
24. Lu, J. & Vučković, J. Nanophotonic computational design. *Opt. Express* **21**, 13351 (2013).
25. Rogalski, A. History of infrared detectors. (2012) doi:10.2478/s11772−012−0037−7.
26. Basov, D. N., Asenjo-Garcia, A., Schuck, P. J., Zhu, X. & Rubio, A. Polariton panorama. *Nanophotonics* **10**, 549–577 (2020).
27. Basov, D. N., Fogler, M. M. & García De Abajo, F. J. Polaritons in van der Waals materials. *Science (80-.).* **354**, (2016).
28. Schuller, J. A. *et al.* Plasmonics for extreme light concentration and manipulation. *Nat. Mater.* **9**, 193–204 (2010).
29. Passler, N. C. *et al.* Hyperbolic shear polaritons in low-symmetry crystals. *Nat. 2022 6027898* **602**, 595–600 (2022).
30. Boltasseva, A. & Atwater, H. A. Low-loss plasmonic metamaterials. *Science (80-.).* **331**, 290–291 (2011).

31. Naik, G. V., Shalaev, V. M. & Boltasseva, A. Alternative plasmonic materials: Beyond gold and silver. *Adv. Mater.* **25**, 3264–3294 (2013).
32. Caldwell, J. D. *et al.* Low-loss, infrared and terahertz nanophotonics using surface phonon polaritons. *Nanophotonics* vol. 4 44–68 (2015).
33. Huber, A. J., Ocelic, N. & Hillenbrand, R. Local excitation and interference of surface phonon polaritons studied by near-field infrared microscopy. *J. Microsc.* **229**, 389–395 (2008).
34. Yu, P. Y. & Cardona, M. Fundamentals of semiconductors : physics and materials properties. 775 (2010).
35. Folland, T. G., Nordin, L., Wasserman, D. & Caldwell, J. D. Probing polaritons in the mid- to far-infrared. *J. Appl. Phys.* **125**, 191102 (2019).
36. Takagi, K. *et al.* Surface plasmon polariton resonance of gold, silver, and copper studied in the kretschmann geometry: Dependence on wavelength, angle of incidence, and film thickness. *J. Phys. Soc. Japan* **86**, (2017).
37. Link, S. & El-Sayed, M. A. Size and temperature dependence of the plasmon absorption of colloidal gold nanoparticles. *J. Phys. Chem. B* **103**, 4212–4217 (1999).
38. Link, S. & El-Sayed, M. A. Spectral Properties and Relaxation Dynamics of Surface Plasmon Electronic Oscillations in Gold and Silver Nanodots and Nanorods. *J. Phys. Chem. B* **103**, 8410–8426 (1999).
39. Huber, A. J., Wittborn, J. & Hillenbrand, R. Infrared spectroscopic near-field mapping of single nanotransistors. *Nanotechnology* **21**, (2010).
40. Atkin, J. M., Berweger, S., Jones, A. C. & Raschke, M. B. Nano-optical imaging and spectroscopy of order, phases, and domains in complex solids. *Adv. Phys.* **61**, 745–842 (2012).
41. Davis, C. C. The optics of anisotropic media. *Lasers and Electro-optics* 539–579 (2014) doi:10.1017/CBO9781139016629.018.
42. He, M. *et al.* Anisotropy and Modal Hybridization in Infrared Nanophotonics Using Low-Symmetry Materials. *ACS Photonics* (2021) doi:10.1021/ACSPHOTONICS.1C01486/ASSET/IMAGES/MEDIUM/PH1C01486_0011.GIF.
43. Ma, W. *et al.* In-plane anisotropic and ultra-low-loss polaritons in a natural van der Waals

crystal. *Nature* **562**, 557–562 (2018).

44. Ma, W. *et al.* Ghost hyperbolic surface polaritons in bulk anisotropic crystals. *Nature* **596**, 362–366 (2021).
45. Caldwell, J. D. *et al.* Sub-diffractional volume-confined polaritons in the natural hyperbolic material hexagonal boron nitride. *Nat. Commun.* **5**, (2014).
46. Giles, A. J. *et al.* Ultralow-loss polaritons in isotopically pure boron nitride. *Nat. Mater.* **17**, (2018).
47. Chaudhary, K. *et al.* Engineering phonon polaritons in van der Waals heterostructures to enhance in-plane optical anisotropy. *Sci. Adv.* **5**, (2019).
48. Noginov, M. A. *et al.* Bulk photonic metamaterial with hyperbolic dispersion. *Appl. Phys. Lett.* **94**, (2009).
49. Kidwai, O., Zhukovsky, S. V. & Sipe, J. E. Effective-medium approach to planar multilayer hyperbolic metamaterials: Strengths and limitations. *Phys. Rev. A - At. Mol. Opt. Phys.* **85**, (2012).
50. Li, P. *et al.* Hyperbolic phonon-polaritons in boron nitride for near-field optical imaging and focusing. *Nat. Commun. 2015 61* **6**, 1–9 (2015).
51. Staude, I. & Schilling, J. Metamaterial-inspired silicon nanophotonics. *Nat. Photonics* **11**, 274–284 (2017).
52. Kildishev, A. V, Boltasseva, A. & Shalaev, V. M. Planar Photonics with Metasurfaces. *Science (80-.).* **339**, (2013).
53. Meinzer, N., Barnes, W. L. & Hooper, I. R. Plasmonic meta-atoms and metasurfaces. *Nat. Photonics* **8**, 889–898 (2014).
54. Khurgin, J. B. Relative merits of phononics vs. plasmonics: the energy balance approach. *Nanophotonics* **7**, 305–316 (2018).
55. Wuttig, M., Bhaskaran, H. & Taubner, T. Phase-change materials for non-volatile photonic applications. *Nat. Photonics* **11**, 465–476 (2017).
56. Li, P. *et al.* Reversible optical switching of highly confined phonon–polaritons with an ultrathin phase-change material. *Nat. Mater.* **15**, 870–875 (2016).
57. Yin, X. *et al.* Beam switching and bifocal zoom lensing using active plasmonic metasurfaces. *Light. Sci. Appl.* **6**, e17016–e17016 (2017).
58. Karvounis, A., Gholipour, B., MacDonald, K. F. & Zheludev, N. I. All-dielectric phase-

change reconfigurable metasurface. *Appl. Phys. Lett.* **109**, 51103 (2016).

59. Guo, P. J. et al. Conformal Coating of a Phase Change Material on Ordered Plasmonic Nanorod Arrays for Broadband All-Optical Switching. *ACS Nano* **11**, 693–701 (2017).
60. Kats, M. A. *et al.* Ultra-thin perfect absorber employing a tunable phase change material. *Appl. Phys. Lett.* **101**, 221101 (2012).
61. Giles, A. J. *et al.* Ultralow-loss polaritons in isotopically pure boron nitride. *Nat. Mater.* **17**, 134–139 (2017).
62. Vuong, T. Q. P. *et al.* Isotope engineering of van der Waals interactions in hexagonal boron nitride. *Nat. Mater.* **17**, 152–158 (2017).
63. Poddubny, A., Iorsh, I., Belov, P. & Kivshar, Y. Hyperbolic metamaterials. *Nat. Photonics* **7**, 948–957 (2013).
64. Dai, S. *et al.* Tunable phonon polaritons in atomically thin van der Waals crystals of boron nitride. *Science (80-.).* **343**, 1125–1129 (2014).
65. Duan, J. *et al.* Launching Phonon Polaritons by Natural Boron Nitride Wrinkles with Modifiable Dispersion by Dielectric Environments. *Adv. Mater.* **29**, 1702494 (2017).
66. Folland, T. G. *et al.* Reconfigurable infrared hyperbolic metasurfaces using phase change materials. *Nat. Commun.* **9**, (2018).
67. Yu, N. *et al.* Light Propagation with Phase Discontinuities: Generalized Laws of Reflection and Refraction. *Science (80-.).* **334**, 333–337 (2011).
68. Vakil, A. & Engheta, N. Transformation Optics Using Graphene. *Science (80-.).* **332**, 1291–1294 (2011).
69. Zheng, Z. *et al.* Highly Confined and Tunable Hyperbolic Phonon Polaritons in Van Der Waals Semiconducting Transition Metal Oxides. *Adv. Mater.* **30**, 1705318 (2018).
70. He, M. *et al.* Deterministic inverse design of Tamm plasmon thermal emitters with multi-resonant control. *Nat. Mater.* **20**, 1663–1669 (2021).
71. Abedini Dereshgi, S. *et al.* Lithography-free IR polarization converters via orthogonal in-plane phonons in α-MoO(3) flakes. *Nat. Commun.* **11**, 5771 (2020).
72. Dixit, S., Sahoo, N. R., Mall, A. & Kumar, A. Mid infrared polarization engineering via sub-wavelength biaxial hyperbolic van der Waals crystals. *Sci. Rep.* **11**, 6612 (2021).
73. Folland, T. G. & Caldwell, J. D. Precise control of infrared polarization using crystal vibrations. *Nature* **562**, 499–501 (2018).

74. Bergman, D. J. & Stockman, M. I. Surface Plasmon Amplification by Stimulated Emission of Radiation: Quantum Generation of Coherent Surface Plasmons in Nanosystems. *Phys. Rev. Lett.* **90**, (2003).
75. Jacob, Z. Hyperbolic phonon–polaritons. *Nat. Mater.* **13**, 1081–1083 (2014).
76. Liu, Z., Lee, H., Xiong, Y., Sun, C. & Zhang, X. Far-Field Optical Hyperlens Magnifying Sub-Diffraction-Limited Objects. *Science (80-.).* **315**, 1686 (2007).
77. Xiong, Y., Liu, Z. & Zhang, X. A simple design of flat hyperlens for lithography and imaging with half-pitch resolution down to 20 nm. *Appl. Phys. Lett.* **94**, 203108 (2009).
78. Dai, S. *et al.* Subdiffractional focusing and guiding of polaritonic rays in a natural hyperbolic material. *Nat. Commun.* **6**, (2015).
79. Li, P. *et al.* Infrared hyperbolic metasurface based on nanostructured van der Waals materials. *Science (80-.).* **359**, 892–896 (2018).
80. Chaudhary, K. *et al.* Polariton nanophotonics using phase-change materials. *Nat. Commun. 2019 101* **10**, 1–6 (2019).
81. Rivera, N., Rosolen, G., Joannopoulos, J. D., Kaminer, I. & Soljačić, M. Making two-photon processes dominate one-photon processes using mid-IR phonon polaritons. *Proc. Natl. Acad. Sci. U. S. A.* **114**, 13607–13612 (2017).
82. Dai, S. *et al.* Internal Nanostructure Diagnosis with Hyperbolic Phonon Polaritons in Hexagonal Boron Nitride. *Nano Lett.* **18**, 5205–5210 (2018).
83. Hauer, B. *et al.* Exploiting Phonon-Resonant Near-Field Interaction for the Nanoscale Investigation of Extended Defects. *Adv. Funct. Mater.* **30**, 1907357 (2020).
84. Sun, J., Litchinitser, N. M. & Zhou, J. Indefinite by Nature: From Ultraviolet to Terahertz. *ACS Photonics* **1**, 293–303 (2014).
85. Taboada-Gutiérrez, J. *et al.* Broad spectral tuning of ultra-low-loss polaritons in a van der Waals crystal by intercalation. *Nat. Mater. 2020 199* **19**, 964–968 (2020).
86. Caldwell, J. D. *et al.* Photonics with hexagonal boron nitride. *Nat. Rev. Mater. 2019 48* **4**, 552–567 (2019).
87. Khurgin, J. B. How to deal with the loss in plasmonics and metamaterials. *Nat. Nanotechnol.* **10**, 2–6 (2015).
88. Foteinopoulou, S., Devarapu, G. C. R., Subramania, G. S., Krishna, S. & Wasserman, D. Phonon-polaritonics: Enabling powerful capabilities for infrared photonics.

Nanophotonics **8**, 2129–2175 (2019).

89. Fali, A. *et al.* Refractive Index-Based Control of Hyperbolic Phonon-Polariton Propagation. *Nano Lett.* **19**, 7725–7734 (2019).
90. Ambrosio, A. *et al.* Selective excitation and imaging of ultraslow phonon polaritons in thin hexagonal boron nitride crystals. *Light. Sci. Appl.* **7**, 27 (2018).
91. Dai, S. *et al.* Phase-Change Hyperbolic Heterostructures for Nanopolaritonics: A Case Study of hBN/VO2. *Adv. Mater.* **31**, 1900251 (2019).
92. Kim, K. S. *et al.* The Effect of Adjacent Materials on the Propagation of Phonon Polaritons in Hexagonal Boron Nitride. *J. Phys. Chem. Lett.* **8**, 2902–2908 (2017).
93. Shen, J. *et al.* Hyperbolic phonon polaritons with positive and negative phase velocities in suspended α-MoO_3. *Appl. Phys. Lett.* **120**, 113101 (2022).
94. Duan, J. *et al.* Planar refraction and lensing of highly confined polaritons in anisotropic media. *Nat. Commun.* **12**, 4325 (2021).
95. Fröch, J. E. *et al.* Purcell Enhancement of a Cavity-Coupled Emitter in Hexagonal Boron Nitride. *Small* **18**, 2104805 (2021).
96. Yang, J. *et al.* Boundary-Induced Auxiliary Features in Scattering-Type Near-Field Fourier Transform Infrared Spectroscopy. *ACS Nano* **14**, 1123–1132 (2019).
97. Feres, F. H., Mayer, R. A., Barcelos, I. D., Freitas, R. O. & Maia, F. C. B. Acceleration of Subwavelength Polaritons by Engineering Dielectric-Metallic Substrates. *ACS Photonics* **7**, 1396–1402 (2020).
98. Blundo, E. *et al.* Vibrational Properties in Highly Strained Hexagonal Boron Nitride Bubbles. *Nano Lett.* **22**, 1525–1533 (2022).
99. Lyu, B. *et al.* Phonon Polariton-assisted Infrared Nanoimaging of Local Strain in Hexagonal Boron Nitride. *Nano Lett.* **19**, 1982–1989 (2019).
100. Lee, I.-H., Yoo, D., Avouris, P., Low, T. & Oh, S.-H. Graphene acoustic plasmon resonator for ultrasensitive infrared spectroscopy. *Nat. Nanotechnol.* **14**, 313–319 (2019).
101. Dai, S. *et al.* Hyperbolic Phonon Polaritons in Suspended Hexagonal Boron Nitride. *Nano Lett.* **19**, 1009–1014 (2018).
102. Menabde, S. G. *et al.* Near-field probing of image phonon-polaritons in hexagonal boron nitride on gold crystals. *Sci. Adv.* **8**, eabn0627–eabn0627 (2022).
103. Nagpal, P., Lindquist, N. C., Oh, S.-H. & Norris, D. J. Ultrasmooth Patterned Metals for

Plasmonics and Metamaterials. *Science (80-.).* **325**, 594–597 (2009).

104. McPeak, K. M. *et al.* Plasmonic Films Can Easily Be Better: Rules and Recipes. *ACS photonics* **2**, 326–333 (2015).
105. Lee, I.-H. *et al.* Image polaritons in boron nitride for extreme polariton confinement with low losses. *Nat. Commun.* **11**, 3649 (2020).
106. Law, S., Adams, D. C., Taylor, A. M. & Wasserman, D. Mid-infrared designer metals. *Opt. Express* **20**, 12155 (2012).
107. Nolen, J. R. *et al.* Ultraviolet to far-infrared dielectric function of n-doped cadmium oxide thin films. *Phys. Rev. Mater.* **4**, (2020).
108. Wagner, M. *et al.* Ultrafast Dynamics of Surface Plasmons in InAs by Time-Resolved Infrared Nanospectroscopy. *Nano Lett.* **14**, 4529–4534 (2014).
109. Yang, Y. *et al.* Femtosecond optical polarization switching using a cadmium oxide-based perfect absorber. *Nat. Photonics* **11**, 390–395 (2017).
110. Cassabois, G., Valvin, P. & Gil, B. Hexagonal boron nitride is an indirect bandgap semiconductor. *Nat. Photonics* **10**, 262–266 (2016).
111. Dunkelberger, A. D. *et al.* Active tuning of surface phonon polariton resonances via carrier photoinjection. *Nat. Photonics* **12**, 50–56 (2017).
112. Xiao, Y., Charipar, N. A., Salman, J., Piqué, A. & Kats, M. A. Nanosecond mid-infrared pulse generation via modulated thermal emissivity. *Light. Sci. Appl.* **8**, 51 (2019).
113. Dazzi, A., Glotin, F. & Carminati, R. Theory of infrared nanospectroscopy by photothermal induced resonance. *J. Appl. Phys.* **107**, (2010).
114. Centrone, A. Infrared Imaging and Spectroscopy beyond the Diffraction Limit∗. *Annu. Rev. Anal. Chem.* **8**, 101–126 (2015).
115. Chae, J. *et al.* Nanophotonic Atomic Force Microscope Transducers Enable Chemical Composition and Thermal Conductivity Measurements at the Nanoscale. *Nano Lett.* **17**, 5587–5594 (2017).
116. Katzenmeyer, A. M., Canivet, J., Holland, G., Farrusseng, D. & Centrone, A. Assessing Chemical Heterogeneity at the Nanoscale in Mixed-Ligand Metal-Organic Frameworks with the PTIR Technique. *Angew. Chemie Int. Ed.* **53**, 2852–2856 (2014).
117. Ruggeri, F. S. *et al.* Infrared nanospectroscopy characterization of oligomeric and fibrillar aggregates during amyloid formation. *Nat. Commun.* **6**, 7831 (2015).

118. Baldassarre, L. *et al.* Mapping the amide I absorption in single bacteria and mammalian cells with resonant infrared nanospectroscopy. *Nanotechnology* **27**, 75101 (2016).
119. Strelcov, E. *et al.* CH(3)NH(3)PbI(3) perovskites: Ferroelasticity revealed. *Sci. Adv.* **3**, e1602165–e1602165 (2017).
120. Ghosh, S. *et al.* Conducting polymer nanostructures for photocatalysis under visible light. *Nat. Mater.* **14**, 505–511 (2015).
121. Morsch, S., Liu, Y., Lyon, S. B. & Gibbon, S. R. Insights into Epoxy Network Nanostructural Heterogeneity Using AFM-IR. *ACS Appl. Mater. & Interfaces* **8**, 959–966 (2015).
122. Van Eerdenbrugh, B., Lo, M., Kjoller, K., Marcott, C. & Taylor, L. S. Nanoscale Mid-Infrared Evaluation of the Miscibility Behavior of Blends of Dextran or Maltodextrin with Poly(vinylpyrrolidone). *Mol. Pharm.* **9**, 1459–1469 (2012).
123. Lahiri, B., Holland, G. & Centrone, A. Chemical Imaging Beyond the Diffraction Limit: Experimental Validation of the PTIR Technique. *Small* **9**, 439–445 (2012).
124. Chae, J., Lahiri, B. & Centrone, A. Engineering Near-Field SEIRA Enhancements in Plasmonic Resonators. *ACS photonics* **3**, 87–95 (2016).
125. Khanikaev, A. B. *et al.* Experimental demonstration of the microscopic origin of circular dichroism in two-dimensional metamaterials. *Nat. Commun.* **7**, 12045 (2016).
126. Dazzi, A. & Prater, C. B. AFM-IR: Technology and Applications in Nanoscale Infrared Spectroscopy and Chemical Imaging. *Chem. Rev.* **117**, 5146–5173 (2016).
127. Greffet, J.-J. *et al.* Coherent emission of light by thermal sources. *Nature* **416**, 61–64 (2002).
128. Hillenbrand, R., Taubner, T. & Keilmann, F. Phonon-enhanced light–matter interaction at the nanometre scale. *Nature* **418**, 159–162 (2002).
129. Schuller, J. A., Taubner, T. & Brongersma, M. L. Optical antenna thermal emitters. *Nat. Photonics* **3**, 658–661 (2009).
130. Wang, T. *et al.* Phonon-Polaritonic Bowtie Nanoantennas: Controlling Infrared Thermal Radiation at the Nanoscale. *ACS Photonics* **4**, 1753–1760 (2017).
131. Caldwell, J. D. *et al.* Low-Loss, Extreme Subdiffraction Photon Confinement via Silicon Carbide Localized Surface Phonon Polariton Resonators. (2013) doi:10.1021/nl401590g.
132. Chen, Y. *et al.* Spectral Tuning of Localized Surface Phonon Polariton Resonators for

Low-Loss Mid-IR Applications. *ACS Photonics* **1**, 718–724 (2014).

133. Wang, T., Li, P., Hauer, B., Chigrin, D. N. & Taubner, T. Optical Properties of Single Infrared Resonant Circular Microcavities for Surface Phonon Polaritons. *Nano Lett.* **13**, 5051–5055 (2013).
134. Feng, K. *et al.* Localized surface phonon polariton resonances in polar gallium nitride. *Appl. Phys. Lett.* **107**, 81108 (2015).
135. Razdolski, I. *et al.* Resonant Enhancement of Second-Harmonic Generation in the Mid-Infrared Using Localized Surface Phonon Polaritons in Subdiffractional Nanostructures. *Nano Lett.* **16**, 6954–6959 (2016).
136. Dai, S. *et al.* Graphene on hexagonal boron nitride as a tunable hyperbolic metamaterial. *Nat. Nanotechnol.* (2015) doi:10.1038/nnano.2015.131.
137. Kumar, A., Low, T., Fung, K. H., Avouris, P. & Fang, N. X. Tunable Light–Matter Interaction and the Role of Hyperbolicity in Graphene–hBN System. *Nano Lett.* **15**, 3172–3180 (2015).
138. Woessner, A. *et al.* Highly confined low-loss plasmons in graphene–boron nitride heterostructures. *Nat. Mater.* **14**, 421–425 (2014).
139. Caldwell, J. D. *et al.* Atomic-scale photonic hybrids for mid-infrared and terahertz nanophotonics. *Nat. Nanotechnol.* **11**, 9–15 (2016).
140. Caldwell, J. D. & Novoselov, K. S. Mid-infrared nanophotonics. *Nat. Mater. 2015 144* **14**, 364–366 (2015).
141. Giles, A. J. *et al.* Imaging of Anomalous Internal Reflections of Hyperbolic Phonon-Polaritons in Hexagonal Boron Nitride. *Nano Lett.* **16**, 3858–3865 (2016).
142. Ishii, S., Kildishev, A. V, Narimanov, E., Shalaev, V. M. & Drachev, V. P. Sub-wavelength interference pattern from volume plasmon polaritons in a hyperbolic medium. *Laser & Photonics Rev.* **7**, 265–271 (2013).
143. Li, P. *et al.* Hyperbolic phonon-polaritons in boron nitride for near-field optical imaging and focusing. *Nat. Commun.* **6**, 7507 (2015).
144. Korzeb, K., Gajc, M. & Pawlak, D. A. Compendium of natural hyperbolic materials. *Opt. Express* **23**, 25406 (2015).
145. Low, T. *et al.* Polaritons in layered two-dimensional materials. *Nat. Mater. 2016 162* **16**, 182–194 (2016).

146. Xu, X. G. *et al.* One-dimensional surface phonon polaritons in boron nitride nanotubes. *Nat. Commun.* **5**, (2014).
147. Yoxall, E. *et al.* Direct observation of ultraslow hyperbolic polariton propagation with negative phase velocity. *Nat. Photonics* **9**, 674–678 (2015).
148. Sun, Z., Gutiérrez-Rubio, Á., Basov, D. N. & Fogler, M. M. Hamiltonian Optics of Hyperbolic Polaritons in Nanogranules. *Nano Lett.* **15**, 4455–4460 (2015).
149. Rivera, N., Kaminer, I., Zhen, B., Joannopoulos, J. D. & Soljačić, M. Shrinking light to allow forbidden transitions on the atomic scale. *Science (80-.).* **353**, 263–269 (2016).
150. Yang, X., Yao, J., Rho, J., Yin, X. & Zhang, X. Experimental realization of three-dimensional indefinite cavities at the nanoscale with anomalous scaling laws. *Nat. Photonics* **6**, 450–454 (2012).
151. Guo, Y., Newman, W., Cortes, C. L. & Jacob, Z. Applications of Hyperbolic Metamaterial Substrates. *Adv. Optoelectron.* **2012**, 1–9 (2012).
152. Hoffman, A. J. *et al.* Negative refraction in semiconductor metamaterials. *Nat. Mater.* **6**, 946–950 (2007).
153. Chae, J., Dong, Q., Huang, J. & Centrone, A. Chloride Incorporation Process in $CH_3NH_3PbI(3-x)Cl(x)$ Perovskites via Nanoscale Bandgap Maps. *Nano Lett.* **15**, 8114–8121 (2015).
154. Tang, F., Bao, P. & Su, Z. Analysis of Nanodomain Composition in High-Impact Polypropylene by Atomic Force Microscopy-Infrared. *Anal. Chem.* **88**, 4926–4930 (2016).
155. Katzenmeyer, A. M. *et al.* Nanoscale Imaging and Spectroscopy of Plasmonic Modes with the PTIR Technique. *Adv. Opt. Mater.* **2**, 718–722 (2014).
156. Brown, L. V. *et al.* Nanoscale Mapping and Spectroscopy of Nonradiative Hyperbolic Modes in Hexagonal Boron Nitride Nanostructures. *Nano Lett.* (2018) doi:10.1021/acs.nanolett.7b04476.
157. Lu, F., Jin, M. & Belkin, M. A. Tip-enhanced infrared nanospectroscopy via molecular expansion force detection. *Nat. Photonics* **8**, 307–312 (2014).
158. Wieland, K. *et al.* Nanoscale Chemical Imaging of Individual, Chemotherapeutic Cytarabine-loaded Liposomal Nanocarriers. *Nano Res.* **12**, 10.1007/s12274-018-2202–x (2019).
159. Ma, X. *et al.* Revealing the Distribution of Metal Carboxylates in Oil Paint from the

Micro- to Nanoscale. *Angew. Chemie Int. Ed.* **58**, 11652–11656 (2019).

160. Ramer, G., Ruggeri, F. S., Levin, A., Knowles, T. P. J. & Centrone, A. Determination of Polypeptide Conformation with Nanoscale Resolution in Water. *ACS Nano* **12**, 6612–6619 (2018).
161. Tuteja, M., Kang, M., Leal, C. & Centrone, A. Nanoscale partitioning of paclitaxel in hybrid lipid-polymer membranes. *Analyst* **143**, 3808–3813 (2018).
162. Mathurin, J. *et al.* How to unravel the chemical structure and component localization of individual drug-loaded polymeric nanoparticles by using tapping AFM-IR. *Analyst* **143**, 5940–5949 (2018).
163. Schwartz, J. J. *et al.* Chemical Identification of Interlayer Contaminants within van der Waals Heterostructures. *ACS Appl. Mater. Interfaces* **11**, 25578–25585 (2019).
164. Caldwell, J. D. *et al.* Sub-diffractional volume-confined polaritons in the natural hyperbolic material hexagonal boron nitride. *Nat. Commun.* **5**, (2014).
165. Tamagnone, M. *et al.* High Q-factor resonators and nanoantennas based on phonon polaritons in van der Waals materials. *Conference on Lasers and Electro-Optics* (2020) doi:10.1364/cleo_qels.2020.fth4n.2.
166. Verbiest, G. J. & Rost, M. J. Beating beats mixing in heterodyne detection schemes. *Nat. Commun.* **6**, (2015).
167. He, M. *et al.* Ultrahigh-Resolution, Label-Free Hyperlens Imaging in the Mid-IR. *Nano Lett.* acs.nanolett.1c01808 (2021) doi:10.1021/ACS.NANOLETT.1C01808.
168. Cuscó, R. *et al.* Isotopic effects on phonon anharmonicity in layered van der Waals crystals: Isotopically pure hexagonal boron nitride. *Phys. Rev. B* **97**, (2018).
169. Cuscó, R., Edgar, J. H., Liu, S., Li, J. & Artús, L. Isotopic Disorder: The Prevailing Mechanism in Limiting the Phonon Lifetime in Hexagonal BN. *Phys. Rev. Lett.* **124**, (2020).
170. Ni, G. *et al.* Long-Lived Phonon Polaritons in Hyperbolic Materials. *NANO Lett.* **21**, 5767–5773 (2021).
171. Wang, L. *et al.* Manipulating phonon polaritons in low loss ^{11}B enriched hexagonal boron nitride with polarization control. *Nanoscale* **12**, 8188–8193 (2020).
172. Brown, L. V. *et al.* Nanoscale Mapping and Spectroscopy of Nonradiative Hyperbolic Modes in Hexagonal Boron Nitride Nanostructures. *Nano Lett.* **18**, 1628–1636 (2018).

173. Dai, S. *et al.* Manipulation and Steering of Hyperbolic Surface Polaritons in Hexagonal Boron Nitride. *Adv. Mater.* **30**, 1706358 (2018).
174. Yang, Z., Aizpurua, J. & Xu, H. Electromagnetic field enhancement in TERS configurations. *J. Raman Spectrosc.* **40**, 1343–1348 (2009).
175. Hu, D. *et al.* Probing optical anisotropy of nanometer-thin van der waals microcrystals by near-field imaging. *Nat. Commun.* **8**, 1471 (2017).
176. Wong, K. P. *et al.* Edge-Orientation Dependent Nanoimaging of Mid-Infrared Waveguide Modes in High-Index $PtSe_2$. *Adv. Opt. Mater.* **9**, 2100294 (2021).
177. Caldwell, J. D. *et al.* Photonics with hexagonal boron nitride. *Nat. Rev. Mater.* **4**, 552–567 (2019).
178. Huber, A., Ocelic, N., Kazantsev, D. & Hillenbrand, R. Near-field imaging of mid-infrared surface phonon polariton propagation. *Appl. Phys. Lett.* **87**, 81103 (2005).
179. Dai, S. *et al.* Efficiency of Launching Highly Confined Polaritons by Infrared Light Incident on a Hyperbolic Material. *Nano Lett.* **17**, 5285–5290 (2017).
180. Babicheva, V. E. *et al.* Near-Field Surface Waves in Few-Layer MoS_2. *ACS Photonics* **5**, 2106–2112 (2018).
181. Hu, G., Shen, J., Qiu, C., Alù, A. & Dai, S. Phonon Polaritons and Hyperbolic Response in van der Waals Materials. *Adv. Opt. Mater.* **8**, 1901393 (2019).
182. Álvarez-Pérez, G. *et al.* Infrared permittivity of the biaxial van der waals semiconductor α-MoO3 from near-and far-field correlative studies. *Adv. Mater.* **32**, 1908176 (2020).
183. Álvarez-Pérez, G. *et al.* Infrared Permittivity of the Biaxial van der Waals Semiconductor α-MoO3 from Near- and Far-Field Correlative Studies. *Adv. Mater.* **32**, (2020).
184. Chen, M. *et al.* Configurable phonon polaritons in twisted α-MoO3. *Nat. Mater. 2020 1912* **19**, 1307–1311 (2020).
185. Hu, G. *et al.* Topological polaritons and photonic magic angles in twisted α-MoO3 bilayers. *Nat. 2020 5827811* **582**, 209–213 (2020).
186. Zheng, Z. *et al.* A mid-infrared biaxial hyperbolic van der Waals crystal. *Sci. Adv.* **5**, eaav8690 (2019).
187. Taboada-Gutiérrez, J. *et al.* Broad spectral tuning of ultra-low-loss polaritons in a van der Waals crystal by intercalation. *Nat. Mater.* **19**, 964–968 (2020).
188. Schubert, M. *et al.* Anisotropy, phonon modes, and free charge carrier parameters in

monoclinic β-gallium oxide single crystals. *Phys. Rev. B* **93**, 125209 (2016).

189. Claus, R. Polariton Dispersion and Crystal Optics in Monoclinic Materials. *Phys. status solidi* **88**, 683–688 (1978).
190. Armbruster, T. *et al.* Recommended nomenclature of epidote-group minerals. *Eur. J. Mineral.* **18**, (2006).
191. Liu, M. *et al.* Symmetry breaking and geometric confinement in VO2: Results from a three-dimensional infrared nano-imaging. *Appl. Phys. Lett.* **104**, 121905 (2014).
192. PHILLIPPI, C. M. & MAZDIYASNI, K. S. Infrared and Raman Spectra of Zirconia Polymorphs. *J. Am. Ceram. Soc.* **54**, (1971).
193. Koch, E. E., Otto, A. & Kliewwer, K. L. Reflection spectroscopy on monoclinic crystals. *Chem. Phys.* **3**, 362–369 (1974).
194. Basov, D. N., Averitt, R. D. & Hsieh, D. Towards properties on demand in quantum materials. *Nat. Mater.* **16**, 1077–1088 (2017).
195. Chen, C. W., Choe, J. & Morosan, E. Charge density waves in strongly correlated electron systems. *Reports Prog. Phys.* **79**, 084505 (2016).
196. Shiozaki, K. & Sato, M. Topology of crystalline insulators and superconductors. *Phys. Rev. B* **90**, 165114 (2014).
197. Ma, W. *et al.* In-plane anisotropic and ultra-low-loss polaritons in a natural van der Waals crystal. *Nature* **562**, 557–562 (2018).
198. Duan, J. *et al.* Twisted Nano-Optics: Manipulating Light at the Nanoscale with Twisted Phonon Polaritonic Slabs. *Nano Lett.* **20**, 5323–5329 (2020).
199. Peck, D. & Ostrander, A. Crystallography: The Monoclinic System. (2020).
200. Jellison, G. E. *et al.* Spectroscopic dielectric tensor of monoclinic crystals: CdWO4. *Phys. Rev. B* **84**, 195439 (2011).
201. Sturm, C. *et al.* Dipole analysis of the dielectric function of color dispersive materials: Application to monoclinic Ga2O3. *Phys. Rev. B* **94**, 035148 (2016).
202. Mock, A. *et al.* Band-to-band transitions, selection rules, effective mass, and excitonic contributions in monoclinic β−Ga2O3. *Phys. Rev. B* **96**, 245205 (2017).
203. Wu, Y., Zhang, W., Wang, Y., Zou, Z. & Chen, J. Energy dissipation analysis based on velocity gradient tensor decomposition. *Phys. Fluids* **32**, 035114 (2020).
204. Higashiwaki, M. & Jessen, G. H. Guest Editorial: The dawn of gallium oxide

microelectronics. *Appl. Phys. Lett.* **112**, 60401 (2018).

205. Tadjer, M. J. Cheap Ultra-Wide Bandgap Power Electronics? Gallium Oxide May Hold the Answer. *Electrochem. Soc. Interface* **27**, 49–52 (2018).
206. Granqvist, C. G. *Handbook of Inorganic Electrochromic Materials*. (Elsevier, 1995).
207. Miyata, T., Nakatani, T. & Minami, T. Gallium oxide as host material for multicolor emitting phosphors. *J. Lumin.* **87**–**89**, 1183–1185 (2000).
208. Réti, F., Fleischer, M., Meixner, H. & Giber, J. Effect of coadsorption of reducing gases on the conductivity of β-Ga2O3 thin films in the presence of O2. *Sensors Actuators B Chem.* **19**, 573–577 (1994).
209. Winta, C. J., Wolf, M. & Paarmann, A. Low-temperature infrared dielectric function of hyperbolic α-quartz. *Phys. Rev. B* **99**, 144308 (2019).
210. Li, P. *et al.* Optical Nanoimaging of Hyperbolic Surface Polaritons at the Edges of van der Waals Materials. *Nano Lett.* **17**, 228–235 (2017).
211. Álvarez-Pérez, G., Voronin, K. V., Volkov, V. S., Alonso-González, P. & Nikitin, A. Y. Analytical approximations for the dispersion of electromagnetic modes in slabs of biaxial crystals. *Phys. Rev. B* **100**, 1–11 (2019).
212. Jacob, Z. & Narimanov, E. E. Optical hyperspace for plasmons: Dyakonov states in metamaterials. *Appl. Phys. Lett.* **93**, (2008).
213. Zapata-Rodríguez, C. J., Miret, J. J., Vuković, S. & Belić, M. R. Engineered surface waves in hyperbolic metamaterials. *Opt. Express* **21**, 19113 (2013).
214. Sorni, J. A., Naserpour, M., Zapata-Rodríguez, C. J. & Miret, J. J. Dyakonov surface waves in lossy metamaterials. *Opt. Commun.* **355**, 251–255 (2015).
215. Passler, N. C. *et al.* Second-Harmonic Generation from Critically Coupled Surface Phonon Polaritons. *ACS Photonics* **4**, 1048–1053 (2017).
216. Schubert, M. *et al.* Longitudinal phonon plasmon mode coupling in β-Ga2O3. *Appl. Phys. Lett.* **114**, 102102 (2019).
217. Antoniou, P., Suchanek, F., Varner, J. F. & Foley, J. J. Role of Cavity Losses on Nonadiabatic Couplings and Dynamics in Polaritonic Chemistry. *J. Phys. Chem. Lett.* (2020) doi:10.1021/acs.jpclett.0c02406.
218. Gao, W. *et al.* Experimental observation of photonic nodal line degeneracies in metacrystals. *Nat. Commun.* **9**, (2018).

219. Tielrooij, K.-J. *et al.* Out-of-plane heat transfer in van der Waals stacks through electron–hyperbolic phonon coupling. *Nat. Nanotechnol.* **13**, 41–46 (2018).
220. Salihoglu, H. *et al.* Energy Transport by Radiation in Hyperbolic Material Comparable to Conduction. *Adv. Funct. Mater.* **30**, 1905830 (2020).
221. Maia, F. C. B. *et al.* Anisotropic Flow Control and Gate Modulation of Hybrid Phonon-Polaritons. *Nano Lett.* **19**, 708–715 (2019).
222. Bensmann, S. *et al.* Near-field imaging and spectroscopy of locally strained GaN using an IR broadband laser. *Opt. Express* **22**, 22369 (2014).
223. Gigler, A. M. *et al.* Nanoscale residual stress-field mapping around nanoindents in SiC by IR s-SNOM and confocal Raman microscopy. *Opt. Express* **17**, 22351 (2009).
224. Huber, A., Ocelic, N., Taubner, T. & Hillenbrand, R. Nanoscale Resolved Infrared Probing of Crystal Structure and of Plasmon−Phonon Coupling. *Nano Lett.* **6**, 774–778 (2006).
225. Ocelic, N., Huber, A. & Hillenbrand, R. Pseudoheterodyne detection for background-free near-field spectroscopy. *Appl. Phys. Lett.* **89**, 101124 (2006).
226. Arora, A. *et al.* Highly Anisotropic in-Plane Excitons in Atomically Thin and Bulklike 1T′-ReSe2. *Nano Lett.* **17**, (2017).
227. Hwang, W. S. *et al.* High-voltage field effect transistors with wide-bandgap β -Ga 2O3 nanomembranes. *Appl. Phys. Lett.* **104**, (2014).
228. Adachi, S. The Reststrahlen Region. *Opt. Prop. Cryst. Amorph. Semicond.* 33–62 (1999) doi:10.1007/978-1-4615-5241-3_2.
229. Rodrigues Da Silva, R. *et al.* Using phonon resonances as a route to all-angle negative refraction in the far-infrared region: The case of crystal quartz. *Phys. Rev. Lett.* **105**, 163903 (2010).
230. He, M. *et al.* Guided Mid-IR and Near-IR Light within a Hybrid Hyperbolic-Material/Silicon Waveguide Heterostructure. *Adv. Mater.* **33**, 2004305 (2021).
231. Huang, W. *et al.* Van der Waals Phonon Polariton Microstructures: Van der Waals Phonon Polariton Microstructures for Configurable Infrared Electromagnetic Field Localizations (Adv. Sci. 13/2021). *Adv. Sci.* **8**, 2170076 (2021).
232. Dai, Z. *et al.* Edge-oriented and steerable hyperbolic polaritons in anisotropic van der Waals nanocavities. *Nat. Commun. 2020 111* **11**, 1–8 (2020).

233. Kehr, S. C., Döring, J., Gensch, M., Helm, M. & Eng, L. M. FEL-Based Near-Field Infrared to THz Nanoscopy. *http://dx.doi.org/10.1080/08940886.2017.1338421* **30**, 31–35 (2017).
234. Pavlidis, G. *et al.* Experimental confirmation of long hyperbolic polariton lifetimes in monoisotopic (10B) hexagonal boron nitride at room temperature. *APL Mater.* **9**, 91109 (2021).
235. Lalanne, P. & Lemercier-lalanne, D. On the effective medium theory of subwavelength periodic structures. *https://doi.org/10.1080/09500349608232871* **43**, 2063–2085 (2009).
236. Podolskiy, V. A. & Narimanov, E. E. Strongly anisotropic waveguide as a nonmagnetic left-handed system. *Phys. Rev. B* **71**, (2005).
237. Shalaev, V. M. *et al.* Negative index of refraction in optical metamaterials. *Opt. Lett.* **30**, 3356 (2005).
238. Shalaev, V. M. Optical negative-index metamaterials. *Nat. Photonics* **1**, 41–48 (2007).
239. Kim, M., So, S., Yao, K., Liu, Y. & Rho, J. Deep sub-wavelength nanofocusing of UV-visible light by hyperbolic metamaterials. *Sci. Rep.* **6**, 38645 (2016).
240. Thongrattanasiri, S. & Podolskiy, V. A. Hypergratings: nanophotonics in planar anisotropic metamaterials. *Opt. Lett.* **34**, 890 (2009).
241. Lu, D. & Liu, Z. Hyperlenses and metalenses for far-field super-resolution imaging. *Nat. Commun.* **3**, (2012).
242. Sun, J., Shalaev, M. I. & Litchinitser, N. M. Experimental demonstration of a non-resonant hyperlens in the visible spectral range. *Nat. Commun.* **6**, 7201 (2015).
243. Noginov, M. A. *et al.* Controlling spontaneous emission with metamaterials. *Opt. Lett.* **35**, 1863 (2010).
244. Iorsh, I., Poddubny, A., Orlov, A., Belov, P. & Kivshar, Y. S. Spontaneous emission enhancement in metal–dielectric metamaterials. *Phys. Lett. A* **376**, 185–187 (2012).
245. Jacob, Z. *et al.* Engineering photonic density of states using metamaterials. *Appl. Phys. B* **100**, 215–218 (2010).
246. Kidwai, O., Zhukovsky, S. V & Sipe, J. E. Dipole radiation near hyperbolic metamaterials: applicability of effective-medium approximation. *Opt. Lett.* **36**, 2530 (2011).
247. Lu, D., Kan, J. J., Fullerton, E. E. & Liu, Z. Enhancing spontaneous emission rates of

molecules using nanopatterned multilayer hyperbolic metamaterials. *Nat. Nanotechnol.* **9**, 48–53 (2014).

248. Sreekanth, K. V., Krishna, K. H., De Luca, A. & Strangi, G. Large spontaneous emission rate enhancement in grating coupled hyperbolic metamaterials. *Sci. Rep.* **4**, 6340 (2014).
249. Sohr, P., Wei, D., Tomasulo, S., Yakes, M. K. & Law, S. Simultaneous Large Mode Index and High Quality Factor in Infrared Hyperbolic Metamaterials. **33**, 33 (2018).
250. Sohr, P., Wei, D., Wang, Z. & Law, S. Strong Coupling in Semiconductor Hyperbolic Metamaterials. *Nano Lett.* **21**, 9951–9957 (2021).
251. Cleri, A. J. *et al.* Tunable, Homoepitaxial Hyperbolic Metamaterials Enabled by High Mobility CdO. *Adv. Opt. Mater.* 2202137 (2022) doi:10.1002/ADOM.202202137.
252. Da Silva, S. W. *et al.* Optical phonon spectra of GaSb/AlSb superlattices: Influence of strain and interface roughnesses. *J. Appl. Phys.* **80**, 597–599 (1996).
253. Sood, A. K., Menéndez, J., Cardona, M. & Ploog, K. Resonance Raman scattering by confined LO and TO phonons in GaAs-AlAs superlattices. *Phys. Rev. Lett.* **54**, 2111–2114 (1985).
254. Ratchford, D. C. *et al.* Controlling the Infrared Dielectric Function through Atomic-Scale Heterostructures. *ACS Nano* **13**, (2019).
255. Herres, N. *et al.* Effect of interfacial bonding on the structural and vibrational properties of InAs/GaSb superlattices. *Phys. Rev. B - Condens. Matter Mater. Phys.* **53**, 15688–15705 (1996).
256. Waterman, J. R. *et al.* The effect of interface bond type on the structural and optical properties of GaSb/InAs superlattices. *Semicond. Sci. Technol.* **8**, (1993).
257. A. Fasolino, E. Molinari, J. C. M. Calculated superlattice and interface phonons of InAs/Gash superlattices. **33**, 8889–8891 (1986).
258. Folland, T. G. & Caldwell, J. D. Chapter 12 Semiconductor Nanophotonics Using Surface Polaritons. *NATO Science for Peace and Security Series B: Physics and Biophysics* 235–254 (2018) doi:10.1007/978-94-024-1544-5_12.
259. Yu, P. Y. & Cardona, M. Fundamentals of Semiconductors. *Graduate Texts in Physics* (2010) doi:10.1007/978-3-642-00710-1.
260. Paudel, T. R. & Lambrecht, W. R. L. Computational study of phonon modes in short-period AlN/GaN superlattices. *Phys. Rev. B* **80**, (2009).

261. Enderlein, R., Suisky, D. & Röseler, J. Optical Phonons in Superlattices. *Phys. status solidi* **165**, 9–66 (1991).
262. Caldwell, J. D. & Novoselov, K. S. Mid-infrared nanophotonics. *Nat. Mater.* **14**, 364–366 (2015).
263. Azuhata, T., Sota, T., Suzuki, K. & Nakamura, S. Polarized Raman spectra in GaN. *J. Phys. Condens. Matter* **7**, L129–L133 (1995).
264. McNeil, L. E., Grimsditch, M. & French, R. H. Vibrational Spectroscopy of Aluminum Nitride. *J. Am. Ceram. Soc.* **76**, 1132–1136 (1993).
265. Jusserand, B. & Cardona, M. Raman spectroscopy of vibrations in superlattices. *Topics in Applied Physics* 49–152 doi:10.1007/bfb0051988.
266. Gleize, J. *et al.* Phonons in a strained hexagonal GaN–AlN superlattice. *Appl. Phys. Lett.* **74**, 703–705 (1999).
267. Gleize, J., Renucci, M. A., Frandon, J. & Demangeot, F. Anisotropy effects on polar optical phonons in wurtzite GaN/AlN superlattices. *Phys. Rev. B* **60**, 15985–15992 (1999).
268. MacMillan, M. F., Devaty, R. P., Choyke, W. J., Khan, M. A. & Kuznia, J. Infrared reflectance of AlN–GaN short period superlattice films. *J. Appl. Phys.* **80**, 2372–2377 (1996).
269. Smirnov, M. B. Vibrational Spectra of AlN⁄GaN Superlattices: Theory and Experiment. *Phys. Solid State* **47**, 742 (2005).
270. Schubert, M., Hofmann, T. & Šik, J. Long-wavelength interface modes in semiconductor layer structures. *Phys. Rev. B* **71**, (2005).
271. Passler, N. C. & Paarmann, A. Generalized 4 × 4 matrix formalism for light propagation in anisotropic stratified media: study of surface phonon polaritons in polar dielectric heterostructures. *J. Opt. Soc. Am. B* **34**, 2128 (2017).
272. Kirk, C. T. Quantitative analysis of the effect of disorder-induced mode coupling on infrared absorption in silica. *Phys. Rev. B* **38**, 1255–1273 (1988).
273. Darakchieva, V. *et al.* Phonon mode behavior in strained wurtzite AlN/GaN superlattices. *Phys. Rev. B - Condens. Matter Mater. Phys.* **71**, 115329 (2005).
274. Harima, H., Nakashima, S. & Uemura, T. Raman scattering from anisotropic LO-phonon–plasmon–coupled mode in*n*-type 4H– and 6H–SiC. *J. Appl. Phys.* **78**, 1996–2005 (1995).
275. Caldwell, J. D. *et al.* Low-loss, infrared and terahertz nanophotonics using surface phonon

polaritons. *Nanophotonics* **4**, 44–68 (2015).

276. Niu, S. *et al.* Giant optical anisotropy in a quasi-one-dimensional crystal. *Nat. Photonics* **12**, 392–396 (2018).
277. Falge, H. J. & Otto, A. Dispersion of Phonon-Like Surface Polaritons on α-Quartz Observed by Attenuated Total Reflection. *Phys. status solidi* **56**, 523–534 (1973).
278. Neuner III, B. *et al.* Critically coupled surface phonon-polariton excitation in silicon carbide. *Opt. Lett.* **34**, 2667 (2009).
279. Taubner, T., Korobkin, D., Urzhumov, Y., Shvets, G. & Hillenbrand, R. Near-Field Microscopy Through a SiC Superlens. *Science (80-.).* **313**, 1595 (2006).
280. Beechem, T. E. *et al.* Tunable Infrared Devices via Ferroelectric Domain Reconfiguration. *Adv. Opt. Mater.* **6**, 1800862 (2018).
281. He, M. *et al.* Phonon engineering of boron nitride via isotopic enrichment. *J. Mater. Res.* **36**, 4394–4403 (2021).
282. Spann, B. T. *et al.* Photoinduced tunability of the reststrahlen band in 4H-SiC. *Phys. Rev. B* **93**, 085205 (2016).
283. Adam D. Dunkelberger, Chase T. Ellis, Daniel C. Ratchford, Alexander J. Giles, Mijin Kim, Chul Soo Kim, Bryan T. Spann, Igor Vurgaftman, Joseph G. Tischler, James P. Long, Orest J. Glembocki, J. C. O. & J. D. C. Active tuning of surface phonon polariton resonances via carrier photoinjection. *Nat. Photonics* **12**, 50–56 (2018).
284. Korlacki, R. *et al.* Strain and stress relationships for optical phonon modes in monoclinic crystals with +¦-Ga2 O3 as an example. *Phys. Rev. B* **102**, (2020).
285. Tekippe, V. J., Ramdas, A. K. & Rodriguez, S. Piezospectroscopic Study of the Raman Spectrum of <math xmlns="http://www.w3.org/1998/Math/MathML" display="inline"><mi>α</mi></math>-Quartz. *Phys. Rev. B* **8**, 706 (1973).
286. Briggs, R. J. & Ramdas, A. K. Piezospectroscopic study of the raman spectrum of cadmium sulfide. *Phys. Rev. B* **13**, 5518–5529 (1976).
287. Bir, G. L. & Pikus, G. E. *Symmetry and strain-induced effects in semiconductors*. *Materials Research* (John Wiley & Sons, 1974).
288. Zheng, Z. *et al.* Phonon Polaritons in Twisted Double-Layers of Hyperbolic van der Waals Crystals. *Nano Lett.* **20**, 5301–5308 (2020).

289. Álvarez-Pérez, G. *et al.* Active Tuning of Highly Anisotropic Phonon Polaritons in Van der Waals Crystal Slabs by Gated Graphene. *ACS Photonics* **9**, 383–390 (2022).
290. Nakayama, M. *et al.* Zone-folding effects on phonons in gaas-alas superlattices. *Jpn. J. Appl. Phys.* **24**, 1331–1334 (1985).
291. Barker, A. S., Merz, J. L. & Gossard, A. C. Study of zone-folding effects on phonons in alternating monolayers of GaAs-AlAs. *Phys. Rev. B* **17**, 3181–3196 (1978).
292. Dechaumphai, E. & Chen, R. Thermal transport in phononic crystals: The role of zone folding effect. *J. Appl. Phys.* **111**, 073508 (2012).
293. Hopkins, P. E. *et al.* Reduction in the thermal conductivity of single crystalline silicon by phononic crystal patterning. *Nano Lett.* **11**, 107–112 (2011).
294. Nakashima, S. & Harima, H. Raman Investigation of SiC Polytypes. *Phys. status solidi* **162**, 39–64 (1997).
295. Gubbin, C. R. *et al.* Hybrid longitudinal-transverse phonon polaritons. *Nat. Commun. 2019 101* **10**, 1–6 (2019).
296. Molinari, E., Fasolino, A. & Kunc, K. Confined longitudinal and transverse phonons in GaAs/AlAs superlattices. *Superlattices Microstruct.* **2**, 397–400 (1986).
297. Molinari, E., Fasolino, A. & Kunc, K. Superlattice effects on confined phonons. *Phys. Rev. Lett.* **56**, 1751 (1986).
298. Jusserand, B. & Paquet, D. Comment on 'resonance raman scattering by confined LO and to phonons in gaAs-alAs superlattices'. *Phys. Rev. Lett.* **56**, 1752 (1986).
299. Sood, A. K., Menéndez, J., Cardona, M. & Ploog, K. Sood et al. respond. *Phys. Rev. Lett.* **56**, 1753 (1986).
300. Hoglund, E. R. *et al.* Emergent interface vibrational structure of oxide superlattices. *Nat. 2022 6017894* **601**, 556–561 (2022).
301. Armelles, G., Recio, M., Ruiz, A. & Briones, F. Confined optical phonons in GaAs/GaP strained layer superlattices. *Solid State Commun.* **71**, 431–434 (1989).
302. D. Berdekas, G. K. Phonon confinement in InAs/GaSb superlattices. **43**, 9976–9979 (1991).
303. Katayama, S. I. & Fukasawa, R. Raman Spectra of Confined LO Phonons in Single Heterostructure. *J. Phys. Soc. Japan* **56**, 3726–3733 (1987).
304. Kroemer, H. The 6.1Å family (InAs, GaSb, AlSb) and its heterostructures: a selective

review. *Phys. E Low-dimensional Syst. Nanostructures* **20**, 196–203 (2004).

305. Dutta, P. S., Bhat, H. L. & Kumar, V. The physics and technology of gallium antimonide: An emerging optoelectronic material. *J. Appl. Phys.* **81**, 5821–5870 (1997).
306. Bennett, B. R., Magno, R., Boos, J. B., Kruppa, W. & Ancona, M. G. Antimonide-based compound semiconductors for electronic devices: A review. *Solid. State. Electron.* **49**, 1875–1895 (2005).
307. Alam, M. N., Matson, J. R., Sohr, P., Caldwell, J. D. & Law, S. Interface quality in GaSb/AlSb short period superlattices. (2021) doi:10.1116/6.0001290.
308. Schwartz, G. P., Gualtieri, G. J., Sunder, W. A. & Farrow, L. A. Light scattering from quantum confined and interface optical vibrational modes in strained-layer GaSb/AlSb superlattices. *Phys. Rev. B* **36**, 4868–4877 (1987).
309. Said, A. H. *et al.* High-energy-resolution inelastic X-ray scattering spectrometer at beamline 30-ID of the Advanced Photon Source. *J. Synchrotron Radiat.* **27**, 827–835 (2020).
310. Chaudhary, K. *et al.* Polariton nanophotonics using phase-change materials. *Nat. Commun.* **10**, 4487 (2019).
311. Hu, H. *et al.* Doping-driven topological polaritons in graphene/α-MoO3 heterostructures. *Nat. Nanotechnol. 2022 179* **17**, 940–946 (2022).
312. Pearton, S. J. *et al.* A review of Ga2O3 materials, processing, and devices. *Appl. Phys. Rev.* **5**, (2018).
313. Gubbin, C. R., De Liberato, S. & Folland, T. G. Surface phonon polaritons for infrared optoelectronics. *J. Appl. Phys.* **131**, 030901 (2022).
314. Comsol. COMSOL Multiphysics. *accessed: July 27, 2020*.
315. Schubert, M. *et al.* Phonon Properties. in *Gallium Oxide: Materials Properties, Crystal Growth, and Devices* (eds. Higashiwaki, M. & Fujita, S.) 501–534 (Springer International Publishing, 2020). doi:10.1007/978-3-030-37153-1_28.